

Collective radiative effects in nanofiber-coupled atomic ensembles

From timed Dicke states to full inversion

DISSERTATION

Zur Erlangung des akademischen Grades
doctor rerum naturalium
(Dr. rer. nat.)
im Fach Physik

eingereicht an der
Mathematisch-Naturwissenschaftlichen Fakultät
der Humboldt-Universität zu Berlin

von

M.Sc.-Phys. Christian Liedl

Präsidentin der Humboldt-Universität zu Berlin:
Prof. Dr. Julia von Blumenthal

Dekanin der Mathematisch-Naturwissenschaftlichen Fakultät:
Prof. Dr. Caren Tischendorf

Gutachter:
Prof. Dr. Arno Rauschenbeutel
Prof. Dr. Oliver Benson
Prof. Dr. Antoine Browaeys

Tag der mündlichen Prüfung:
24. März 2023

Acknowledgements

First of all, I would like to thank Arno Rauschenbeutel for giving me the opportunity to pursue a Ph.D. in his group. I am very thankful for his support and that he encouraged and allowed me to investigate what triggered my interest. I learned a lot from his intuitive and curiosity-driven approach to physics, and I really appreciate the many discussions with him that have often led to crucial insights. I am also very grateful to Philipp Schneeweiss for the excellent supervision and for teaching me everything from tedious and technical intricacies to fundamental physics. At the same time, he always kept an eye on the bigger picture, and his advice often steered my project into the right direction.

I would like to thank Stanimir Kondov for transmitting great fascination for science and for encouraging me to start a Ph.D. I also want to thank Sofia Pazzagli for motivating and inspiring me to continue my Ph.D. after a somewhat solitary start as the only group member in Berlin and for being a great person in general.

I thank Fedoua Rothländer for her outstanding support and for always fighting in our favor in an administrative uphill battle. I am also very grateful to Thomas Hoinkes and Dagmar Fahnauer for their help with all technical problems in our lab.

One of the things I enjoyed most about my Ph.D. was working with my colleagues from the old atoms team. I would like to thank Yijian Meng for introducing me to our experiment and for passing old atom-specific experimental wisdom. Sebastian Pucher and I moved the experiment from Vienna to Berlin, and we spent endless time re-building, re-calibrating, and re-inventing the lab. I thank him for his hard work, great experimental wit, and for teaching me how to correctly pronounce the word “Kaffeeeee”. I am very grateful to Felix Tebbenjohanns for his quick understanding, technical knowledge, and theoretical deep dives, which have been crucial for my project. Moreover, I thank him for sparking new curiosity and joy in physics at a point at which I was worried and bogged down with the need to produce results. Only recently, Constanze Bach has joined our group. She has learned to control the setup and contributed new ideas and understanding to our projects at record speed. I really enjoyed working with her and I am very happy that I can pass the experiment to such capable hands. Furthermore, I am very grateful to our nanofiber, which has outlived yet another Ph.D. student with great perseverance.

I am also very thankful for the many discussions with group members that were not directly involved in our projects. Especially, I would like to thank Jürgen Volz for his numerous contributions to my project, for taking the time to teach me about physics, and for being a great bullshit detector. I also thank Riccardo Pennetta, Max Schemmer, Martin Cordier, and Martin Blaha for sharing their knowledge with me and for many fruitful discussions. I would like to thank Leonid Yatsenko for helping us understand our results

on oscillatory Raman gain. I would also like to thank all other group members, many of whom have become great friends, for creating an encouraging and familial environment, which I will miss very much.

I was lucky to be part of the Berlin School of Optical Sciences and Quantum Technologies, which allowed me to connect with Ph.D. students from other research groups in Berlin. I would especially like to thank Luisa Esguerra Rodríguez, Daniel Lechner, Gabriela Luna Amador, Pia Fürtjes, and Julian Bopp for being able to share the frustrations and worries during my Ph.D. and for being great friends. I thank the nanofiber running team for the collectively enhanced motivation and for many out-of-breath discussions about physics and life. I also want to thank the Friday Light Talks team for allowing me to contribute to an open, inspiring, and collaborative environment at the physics institute. I really enjoyed organizing each event.

I would like to thank my non-physics friends for taking my mind off physics and keeping me sane over the last few years. A very special thank you goes to my parents and my brother for their unconditional support and understanding throughout my whole life. Most importantly, I would like to thank Mariel García Huiman for being the sun and making sure “que acabe alive”.

Abstract

Dicke superradiance is a hallmark effect in quantum optics and describes the collectively enhanced decay of an ensemble of atoms. There, a fully excited ensemble emits light in the form of a short, so-called superradiant burst due to the build-up of a collective dipole moment during the decay. In order to observe this effect, the atoms typically have to be placed in close vicinity to each other. While weakly excited ensembles do not show such burst dynamics, their decay can still be collectively accelerated, even for a large separation between the atoms.

In this thesis, we study collective radiative effects in nanofiber-coupled atomic ensembles that extend over thousands of optical wavelengths. We optically couple up to 1000 atoms to the guided modes of an optical nanofiber, which mediates long-range dipole-dipole interactions between the atoms. We engineer the coupling to be unidirectional, realizing a cascaded quantum system in which the dynamics of each atom is solely determined by the dynamics of upstream atoms.

We coherently excite the atoms using nanofiber-guided optical pulses, allowing us to explore the entire parameter regime from weak excitation to full inversion. We find that coherent forward scattering, which is responsible for superradiance in the weak excitation regime, plays an important role for the dynamics even close to full inversion. We observe superradiant burst dynamics, which occurs in our system despite the macroscopic separation between the atoms and an asymmetric coupling. We find that the peak-emitted power scales even faster with the number of atoms than in the case of ideal Dicke superradiance due to a collectively enhanced channeling efficiency into the nanofiber-guided mode. By analyzing the coherence properties of the superradiant burst, we directly identify two regimes of burst dynamics: in the first, an initial atomic coherence is induced by the excitation laser, leading to a subsequent build-up of the total atomic dipole moment. In the second regime, there is no initial coherence, and the superradiant burst is seeded by vacuum fluctuations. We introduce a cascaded interaction model and find that it accurately describes the collective dynamics of our system over the entire parameter regime explored in this thesis.

Finally, we study the driven dynamics of a nanofiber-coupled ensemble of three-level atoms. We drive two-photon Rabi oscillations between the two ground states of a Λ system and observe the associated oscillatory Raman gain and absorption, which can be understood as a coherent photon exchange between the two drive fields.

Our results shed light on the collective radiation of waveguide-coupled ensembles of quantum emitters and could, e.g., be useful for the generation of multiphoton Fock states, which are a valuable resource for quantum technologies.

Zusammenfassung

Dicke Superradianz ist ein fundamentaler Effekt in der Quantenoptik und beschreibt den kollektiv beschleunigten Zerfall eines Ensembles von Atomen. Dabei kann ein vollständig angeregtes Ensemble durch die Ausbildung eines kollektiven Dipolmoments während des Zerfalls Licht in Form eines kurzen, so genannten superradianten Pulses emittieren. Um diesen Effekt zu beobachten, müssen sich die Atome in der Regel in unmittelbarer Nähe zueinander befinden. Schwach angeregte Ensembles zeigen zwar keine solche Puls-Dynamik, aber ihr Zerfall kann dennoch kollektiv beschleunigt sein, selbst bei einem großen Abstand zwischen den Atomen.

In dieser Arbeit untersuchen wir kollektive Strahlungseffekte in Nanofaser-gekoppelten atomaren Ensembles, die sich über Tausende von optischen Wellenlängen erstrecken. Wir koppeln bis zu 1000 Atome optisch an die geführten Moden einer optischen Nanofaser, die langreichweitige Dipol-Dipol Wechselwirkungen zwischen den Atomen vermittelt. Wir realisieren eine unidirektionale Kopplung und damit ein kaskadiertes Quantensystem, in dem die Dynamik jedes Atoms ausschließlich durch die Dynamik der vorgelagerten Atome bestimmt wird.

Wir regen die Atome mit nanofasergeführten optischen Pulsen kohärent an, was uns ermöglicht, den gesamten Parameterbereich von schwacher Anregung bis hin zur vollständigen Inversion zu erforschen. Wir stellen fest, dass die kohärente Vorwärtsstreuung, die für die Superradianz im Regime der schwachen Anregung verantwortlich ist, auch nahe voller Inversion eine wichtige Rolle für die Dynamik spielt. Wir beobachten superradiante Puls-Dynamik, die in unserem System trotz des makroskopischen Abstands zwischen den Atomen und einer asymmetrischen Kopplung auftritt. Wir stellen fest, dass die emittierte Spitzenleistung noch schneller mit der Anzahl der Atome skaliert als im Fall der idealen Dicke Superradianz, was auf eine kollektiv erhöhte Sammeleffizienz der nanofasergeführten Mode zurückzuführen ist. Die Analyse der Kohärenz-Eigenschaften des superradianten Pulses erlaubt es uns, zwei Regime der Puls-Dynamik zu identifizieren: Im ersten Regime induziert der Anregungslaser eine initiale atomare Kohärenz, die anschließend zu einem Aufbau des totalen atomaren Dipolmoments führt. Im zweiten Regime besteht zunächst keine Kohärenz, und der superradiante Puls wird durch Vakuumfluktuationen ausgelöst. Wir entwickeln ein kaskadiertes Wechselwirkungsmodell und zeigen, dass es die kollektive Dynamik unseres Systems über den gesamten in dieser Arbeit untersuchten Parameterbereich akkurat beschreibt.

Schließlich untersuchen wir die getriebene Dynamik eines Nanofaser-gekoppelten Ensembles von Drei-Niveau-Atomen. Wir treiben Zwei-Photonen-Rabi-Oszillationen zwischen den beiden Grundzuständen eines Λ -Systems und beobachten die damit verbundene os-

zillatorische Raman-Verstärkung und -Absorption, die als kohärenter Photonentransfer zwischen den beiden treibenden Feldern verstanden werden kann.

Unsere Erkenntnisse geben Aufschluss über die kollektive Strahlung von wellenleitergekoppelten Ensembles von Quantenemittern und könnten z.B. hilfreich für die Erzeugung von Multiphotonen-Fock-Zuständen sein, welche eine wertvolle Ressource für Quantentechnologien darstellen.

List of publications

In the process of working on this thesis, the following articles have been published or are currently under review in peer-reviewed journals:

- S.S. Kondov, C.-H. Lee, K. H. Leung, C. Liedl, I. Majewska, R. Moszynski, and T. Zelevinsky. [Molecular lattice clock with long vibrational coherence](#). *Nat. Phys.*, 15(11):1118, 2019.
- Y. Meng, C. Liedl, S. Pucher, A. Rauschenbeutel, and P. Schneeweiss. [Imaging and localizing individual atoms interfaced with a nanophotonic waveguide](#). *Phys. Rev. Lett.*, 125(5):053603, 2020.
- B. Olmos, C. Liedl, I. Lesanovsky, and P. Schneeweiss. [Bragg condition for scattering into a guided optical mode](#). *Phys. Rev. A*, 104(4):043517, 2021.
- S. Pucher*, C. Liedl*, S. Jin, A. Rauschenbeutel, and P. Schneeweiss. [Atomic spin-controlled non-reciprocal Raman amplification of fibre-guided light](#). *Nat. Phot.*, 16(5):380, 2022.
- C. Liedl, S. Pucher, P. Schneeweiss, L. P. Yatsenko, and A. Rauschenbeutel. [Observation of oscillatory Raman gain associated with two-photon Rabi oscillations of nanofiber-coupled atoms](#). *J. Phys. B: At. Mol. Opt. Phys.*, 55(23):234005, 2022.
- C. Liedl, S. Pucher, F. Tebbenjohanns, P. Schneeweiss, and A. Rauschenbeutel. [Collective Radiation of a Cascaded Quantum System: From Timed Dicke States to Inverted Ensembles](#). *Phys. Rev. Lett.*, 130(16):163602, 2023.
- C. Liedl, F. Tebbenjohanns, C. Bach, S. Pucher, A. Rauschenbeutel, and P. Schneeweiss. [Observation of superradiant bursts in waveguide QED](#). *arXiv:2211.08940*, 2022.

*These authors contributed equally: S. Pucher and C. Liedl.

Contents

1	Introduction	1
1.1	Collective light-matter interaction	1
1.2	Waveguide quantum electrodynamics	3
1.3	Outline of the thesis	4
2	Optical nanofiber-based interface	7
2.1	Tapered optical fiber	7
2.2	Nanofiber-based two-color optical dipole trap	9
2.3	Experimental sequence	10
2.4	Detection setup	11
2.5	Measurement of the optical depth	13
2.6	Trapping lifetime	14
2.7	Measurement of the number of atoms	15
2.8	Atom-light coupling strength	15
2.9	Generation of nanosecond-long optical pulses	18
3	Theoretical modeling	21
3.1	Linear response theory	21
3.2	Many-body master equation	22
3.2.1	Dicke superradiant bursts	25
3.2.2	Asymmetric atom-waveguide coupling strength	25
3.2.3	Imperfect atom-waveguide coupling strength	27
3.2.4	Spatial disorder	28
3.3	Coherent state approximation	30
3.4	Mixed coherent state approximation	31
3.5	Comparison of the different approaches	34
3.5.1	Benchmarking using the many-body master equation	34
3.5.2	Benchmarking using the mixed coherent state approximation	36
3.6	Emission into the backward direction	38
3.7	Fluctuations of the coupling strength	40

4	Coherent excitation and coherent forward scattering	43
4.1	Coherent excitation	43
4.1.1	Choice of the pulse duration	45
4.1.2	Absorption of the excitation pulse	46
4.1.3	Dynamics of the transmitted excitation pulses	48
4.1.4	Measurement of the excited state probability	50
4.2	Coherent forward scattering	51
4.2.1	Scaling with the excitation power	51
4.2.2	Scaling with the number of atoms	55
4.3	Intermediate summary and conclusion	56
5	Superradiant bursts	59
5.1	Observation of superradiant burst dynamics	60
5.2	Scaling with the number of atoms	61
5.3	Scaling in the large-N limit	64
5.4	Superradiant burst dynamics for a finite initial dipole moment	66
5.5	Coherence properties of the superradiant burst	68
5.5.1	Two-time correlation functions	68
5.5.2	Heterodyne measurement of the superradiant burst	70
5.5.3	Identification of two regimes of burst dynamics	73
5.6	Subradiant dynamics following a superradiant burst	75
5.6.1	Phase pattern of the subradiant states	77
5.6.2	Subradiant states for full inversion	79
5.7	Intermediate summary and conclusion	80
6	Observation of oscillatory Raman gain associated with two-photon Rabi oscillations	83
6.1	Theoretical modeling	84
6.1.1	Three-level system	84
6.1.2	Adiabatic elimination	86
6.1.3	Analytical solution and probe transmission	87
6.2	Experimental setting	88
6.3	Autler-Townes splitting	90
6.4	Observation of oscillatory Raman gain	91
6.4.1	Scaling with probe power and detuning	94
6.5	Intermediate summary and conclusion	95
7	Conclusion and perspectives	97

Bibliography	99
A Appendix	113
A.1 Transmission coefficient on resonance	113
A.2 Rabi frequency of a nanofiber-guided light field	114
A.3 Optical Bloch equations for a two-level atom	115
A.3.1 Transmission coefficient for arbitrary detuning	116
A.3.2 Analytical solution	116
A.4 Ideal Dicke superradiance in wQED	117
A.5 Extracting the first-order correlation function from the heterodyne signal	118
A.6 First-order correlation function of independent and inverted two-level atoms	121
A.7 Alternative excitation scheme	123
A.8 Optical Bloch equations for a three-level atom	124
A.8.1 Adiabatic elimination	125
A.8.2 Simplified effective two-level system	127

1 Introduction

1.1 Collective light-matter interaction

Understanding the interaction between light and matter is crucial for almost any research field in the natural sciences. Matter absorbs, reflects, transmits, and emits light, allowing us to perceive much of the world through our eyes, cameras, spectrometers, and photodetectors. This enables us to observe physical, biological and chemical processes in nature. The study of light-matter interaction on the level of single atoms and single photons has been a driving force for the research field of quantum optics. In the past sixty years, technological advances such as the development of lasers have facilitated an ever-increasing control of individual atoms [1, 2], enabling quantum technological applications in computation [3, 4], communication [5, 6], sensing [7], and simulation [8].

Once one has understood how a single atom radiates light, one could assume that an ensemble of N atoms radiates in the same way, but simply N times as much as a single atom. However, it was already pointed out in 1954 by Dicke that this is not the case [9]. He theoretically predicted that the spontaneous emission of an ensemble of atoms is collectively altered when the atoms are confined to a volume that is small compared to the optical wavelength cubed. In this thesis, we will call this regime of tight confinement the Dicke regime. Depending on the quantum state of the atomic ensemble, the emission can be either collectively enhanced (superradiant) or inhibited (subradiant). In particular, Dicke predicted that a fully inverted ensemble would emit a short, intense burst of light. This so-called superradiant burst dynamics is strikingly different from the exponential decay dynamics of independently emitting atoms, for which the peak intensity scales linearly with N . Superradiant burst dynamics can be understood as a build-up of atomic coherence due to a collective decay of the atomic ensemble [10, 11]. This results in constructive interference of the fields emitted by the atomic dipoles, which is why the peak-emitted power scales quadratically with the number of atoms. Superradiant burst dynamics was first observed in 1973 [12] in an optically pumped warm vapor, and a lot of experimental and theoretical effort in the following decade went into understanding different aspects of superradiance [10, 11].

Since then, the experimental control of atomic ensembles has improved tremendously. In

particular, laser cooling and trapping of neutral atoms enable the precise preparation of both the motional and electronic atomic state [13]. Dicke superradiance has been observed in a variety of different atomic systems, from warm vapors [12] to Rydberg atoms [14, 15], Bose Einstein condensates [16, 17], atoms in high-finesse cavities [18–20], ion traps [21], and tightly confined dipole traps [22, 23]. In addition, Dicke superradiance has been observed in systems consisting of artificial atoms, such as color centers in diamond [24], superconducting qubits [25], quantum dots, molecular aggregates, and crystals [26, 27]. At the same time, subradiance in the Dicke regime has proven to be experimentally elusive due to the suppressed coupling to light and has only been observed in a few experiments [21, 23, 28–31].

While most of the research on collective radiative effects in the 20th century has focused on super- and subradiance in the Dicke regime, the collective radiation of dilute atomic ensembles has recently gained renewed interest. In 2006, Scully et al. proposed that the absorption of a single photon can prepare an atomic ensemble in a so-called timed Dicke state, in which the arrival time of the photon is imprinted as a relative phase factor onto each atom [32]. The subsequent decay of the atomic ensemble then features so-called single-photon superradiance [33, 34], i.e., strongly enhanced emission into the forward direction due to constructive interference of the atomic dipoles. Following the initial superradiant decay, single-photon subradiance can also occur at later times [35]. In the last five years, such dynamics has been observed in dilute clouds of cold atoms [36–39], Rydberg super atoms [40], and waveguide-coupled ensembles [41–47]. Weakly excited atoms can be described as classical dipole emitters with a linear response [48, 49]. Therefore, single-photon superradiance is also referred to as superradiance in the linear optics, or linear response regime [50].

The phenomena of single-photon superradiance and Dicke superradiance of a fully excited ensemble seem quite different at first sight, and, with very few exceptions [23, 51], most experimental and theoretical works have studied either one or the other. However, both phenomena are intimately connected. Their underlying mechanism is the interference of the fields emitted by the atomic dipoles during their decay, which leads to an enhanced or inhibited collective decay rate of the ensemble.

With the advent of quantum technologies in the last few decades, new applications based on the collective radiation of atomic ensembles have been proposed. For example, superradiant lasers can be used as an active optical clock, promising record stabilities [52–54]. Moreover, the advances in controlling neutral atoms and, more recently, molecules in optical lattices [8] and tweezer arrays [55] have sparked new ideas for applications of collective light-matter interaction. Superradiant emission can be used as a resource for the generation of complex quantum states of light [56–58], which may prove useful for

metrology [59, 60]. In particular, ordered atomic arrays with subwavelength spacing hold great potential for applications. Subradiant states of such atomic arrays lend themselves to efficient quantum storage of light due to their reduced decay rates [61, 62]. It was recently demonstrated that a small interatomic spacing leads to strong reflectivity of a two-dimensional array of atoms, which features subradiant states [63]. Moreover, the reflectivity can be coherently controlled using a single ancilla qubit [64], constituting a first step towards constructing quantum coherent metasurfaces [65].

Experiments with laser-cooled atoms or molecules usually rely on macroscopic free-space setups. While this approach allows for unprecedented experimental control, a lot of experimental effort in the last decade has been geared towards integrating laser-cooled atoms with nanophotonic structures, such as nanophotonic resonators and waveguides [66]. Initially, a major motivation for this research was improving on free-space setups in terms of the atomic coupling strength to a single optical mode, as well as the miniaturization of the experimental setups [67, 68]. However, it soon became clear that nanophotonics allows one to realize completely new paradigms of light-matter interaction [66, 69]. In particular, the ability to couple quantum emitters to waveguides has led to the emerging field of waveguide quantum electrodynamics (wQED), which we will review in the following section. Specifically, we will focus on its potential to study and realize novel effects in collective light-matter interaction.

1.2 Waveguide quantum electrodynamics

The field of wQED describes the interaction between quantum emitters and photons that propagate in a waveguide [41]. As quantum emitters, most prominently quantum dots, superconducting qubits, quantum solid-state defects, and neutral atoms have been used to implement wQED [41, 70–73]. For the waveguide, one can, e.g., use optical nanofibers, hollow-core fibers, superconducting transmission lines, and photonic crystal waveguides [41]. Instead of reviewing all aspects and promises of wQED, we will highlight three main differences compared to free-space setups, which make wQED an intriguing platform for studying collective light-matter interaction.

First, one can scale the number of emitters without compromising the atom-light coupling strength. Using a free-space Gaussian laser beam, one has to decrease the beam waist to increase the atom-light coupling strength. This decreases the Rayleigh length of the beam, leading to an inhomogeneous broadening of the coupling strengths for extended ensembles consisting of many atoms. In contrast, waveguided light fields do not diverge, and one can thus achieve large atom-light coupling, even for samples extending over macroscopic distances.

Second, it has been shown that the strong confinement of light in the transverse direction in a nanophotonic waveguide leads to longitudinal polarization components of the evanescent field. This effect, in combination with atomic polarization selection rules, can be used to engineer propagation direction-dependent atom-light coupling. This so-called chiral light-matter interaction is inherent to many wQED platforms and represents a new degree of freedom for the control of quantum optics systems [69]. In particular, in this thesis, we will use the chiral coupling in our experimental system to study the collective radiative dynamics of a cascaded quantum system [74, 75].

Third, coupling many atoms to a shared optical mode gives rise to dipole-dipole interactions between the atoms, mediated by the optical mode. For free-space optical modes, the corresponding interaction strength decays with the distance between the atoms. However, if the atoms share a common waveguide mode, the interaction becomes, in principle, infinite-ranged.

Specifically, we experiment with nanofiber-coupled ensembles of neutral atoms in this thesis. While, there, the coupling strength is relatively low compared to other wQED systems, the advantage is that thousands of practically indistinguishable atoms can be coupled to the nanofiber mode. These features make wQED with neutral atoms an intriguing platform to shed light on the fundamental mechanisms of super- and subradiance and study new forms of collective light-matter interaction.

1.3 Outline of the thesis

In this thesis, we study collective radiative effects of nanofiber-coupled atomic ensembles. In particular, we explore how the radiative dynamics changes from weak excitation to full inversion, for which superradiant burst dynamics occurs. The thesis is organized as follows.

In chapter 2, we describe the experimental apparatus and the experimental techniques necessary to create an optical nanofiber-based interface for neutral cesium atoms. We describe and characterize the optically trapped ensemble of atoms in terms of its optical depth, the single-atom coupling strength to the guided modes, and the trapping lifetime. We also describe the optical detection setup and the generation of nanosecond-long optical pulses with a large extinction ratio.

In chapter 3, we discuss the theoretical modeling of our experiment. We discuss the role of chiral atom-waveguide coupling and experimental imperfections in the superradiant emission of a nanofiber-coupled atomic ensemble. We present two new models which assume unidirectional atom-waveguide coupling and analyze the parameter space in which the different models are applicable.

In chapter 4, we describe the coherent excitation of an ensemble of nanofiber-coupled atoms by short, resonant Rabi pulses. We discuss different effects that limit the fidelity of the state preparation and infer the achieved excited state probability by measuring the number of photons that the atoms absorb from the excitation pulse. Then, we turn to the collective decay dynamics following the excitation pulse. We find that coherent forward scattering strongly influences the dynamics even beyond the linear response regime.

In chapter 5, we report on the observation of superradiant burst dynamics in a wQED system. We analyze the scaling of the peak emitted power with the number of atoms and explore superradiant burst dynamics for a non-zero initial atomic dipole. We measure the coherence properties of the emitted light and identify two distinct regimes of burst dynamics. Finally, we briefly discuss first insights into the occurrence of subradiant states beyond the regime of linear response.

In chapter 6, we drive the atomic ensemble with two laser fields in a Λ configuration, realizing a three-level system. We observe Autler-Townes splitting in the transmission spectrum of a nanofiber-guided probe laser field. We then drive the atomic ensemble on a far-off-resonant two-photon resonance. We observe and analyze an oscillatory Raman gain of the probe field, which is due to two-photon Rabi oscillations between the two ground states of the Λ system.

Finally, in chapter 7, we conclude and discuss perspectives for future research.

2 Optical nanofiber-based interface

The lab book entry of our experiment from November 20/21, 2008, is shown in Fig. 2.1 and represents a major milestone in our field: the first optical trapping and interfacing of neutral atoms close to a nanofiber [76]. Since then, the experiment has survived a move from Mainz to Vienna, and in 2019, we moved it from Vienna to Berlin. Importantly, the nanofiber has never been exchanged in the last 14 years, which showcases its robustness. It has been the subject of six dissertations and numerous publications, which have each deepened the understanding and control of our experimental system. Since much of the experimental apparatus and standard experimental techniques are described in the dissertations of previous students [77–82], we will only briefly explain the aspects and techniques that are most relevant to this thesis.

We describe the properties of the evanescent field of the nanofiber-guided mode, which is used as an optical interface for the atoms. We explain the optical trapping and the experimental preparation sequence. We then present the optical detection setup and characterize the ensemble of nanofiber-trapped atoms by measuring the number of atoms and their coupling strength, as well as their trapping lifetimes. Finally, we describe the generation of ns-long optical pulses with a large extinction ratio

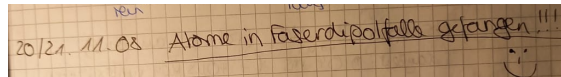


Figure 2.1: Lab book entry from November, 2008: “Trapped atoms in fiber dipole trap!!! :-)”. Credits: Dr. Eugen Vetsch.

2.1 Tapered optical fiber

The nanofiber is implemented as the waist of a tapered optical fiber (TOF), with a nominal length of 5 mm and a nominal diameter of $2r_{\text{fiber}}=500$ nm, see Fig. 2.2(a). It was produced in a heat-and-pull process, with a 4 cm-long taper section [76, 83, 84]. Along this taper, the mode of the standard single-mode fiber is adiabatically transformed into the fundamental nanofiber-guided HE_{11} mode. The adiabatic tapering ensures high transmission through the entire TOF and was measured to be about 97 % [76]. The intensity distribution of the

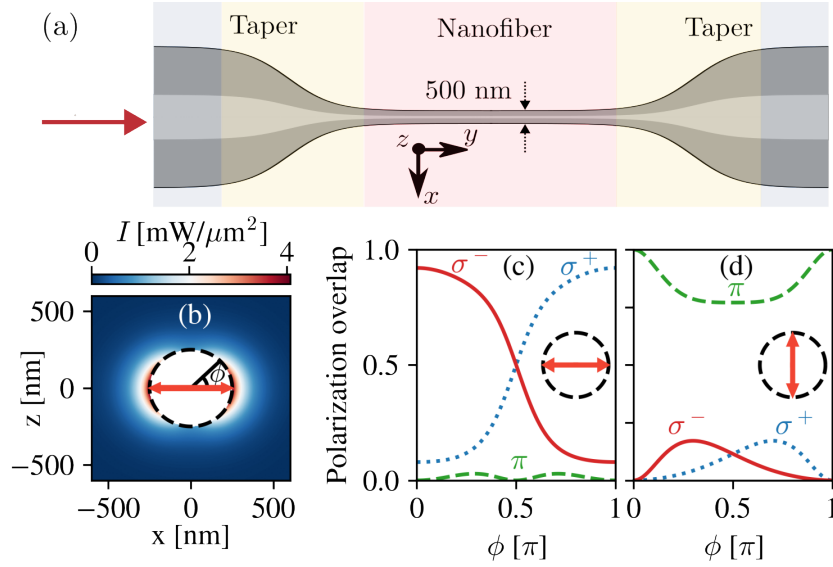


Figure 2.2: (a) Sketch of the tapered optical fiber (not to scale). (b) Intensity of the nanofiber-guided mode in the x - z plane. The light field is quasilinearly polarization along x , indicated by the red arrow, and propagates in the $+y$ -direction. The fiber surface is shown as the black dashed line. The intensity of the evanescent field decays in the radial direction and is larger along the polarization axis. (c) and (d) Polarization overlaps as a function of the azimuthal angle, ϕ , at a radial distance of 230 nm for two different quasilinear polarizations, indicated by the red arrows. The quantization axis is chosen along z .

nanofiber-guided mode in the x - z plane is shown in Fig. 2.2(b) for a light field propagating in the $+y$ -direction, i.e., into the plane [77]. The light field with a power of 1 nW is quasilinearly polarized along the x -axis, which breaks the azimuthal symmetry such that the intensity is stronger along the polarization axis. The intensity decays approximately exponentially in the radial direction, with a decay constant that is proportional to the wavevector of the light field. Figures 2.2(c) and (d) illustrate how the polarization of the evanescent field changes azimuthally at a fixed radial distance of 230 nm from the nanofiber surface. We plot the overlap with σ^{+-} , σ^{-} , and π -polarization as the red solid, blue dotted, and green dashed line, respectively. Note that the quantization axis is chosen along z . In (c), the laser field is quasilinearly polarized along x [85]. Notably, the light is almost perfectly σ^{-} -polarized for $\phi = 0$ and σ^{+} -polarized for $\phi = \pi$ (92 % overlap, respectively). Due to symmetry reasons, these local polarizations have to flip when the light field propagates in the other direction. The local polarization thus depends on the propagation direction of the light field. This effect is also referred to as spin-momentum locking [69]. In (d), the laser field is quasilinearly polarized along z , and the light is

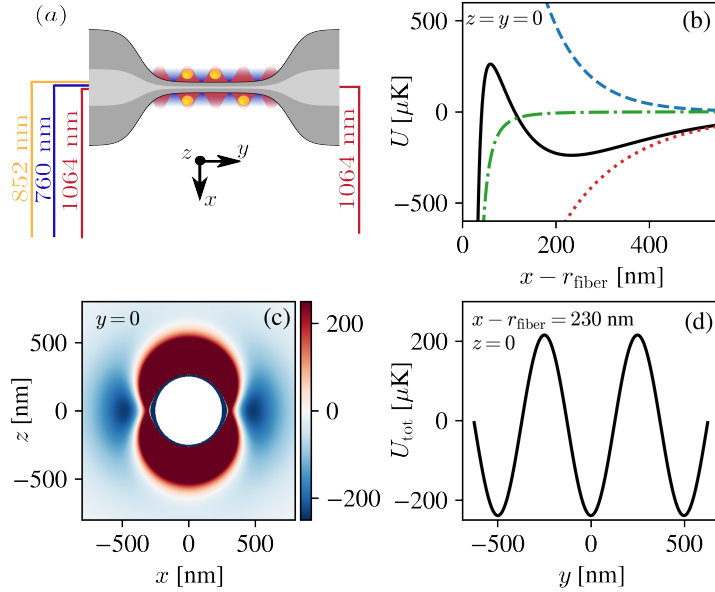


Figure 2.3: (a) Schematic of the nanofiber-based trapping setup. The blue-detuned running wave (760 nm) and red-detuned standing wave (1064 nm) fields create a dipole trap for the cesium atoms (yellow spheres). We use a resonant, guided laser field (852 nm) to perform degenerate Raman cooling and measure the optical depth via transmission spectroscopy. (b) Radial scalar trapping potential as a function of the distance from the nanofiber surface. The solid black line depicts the total trapping potential, calculated by summing up the blue trapping potential (blue dashed line), the red trapping potential (red dotted line), and the Caisimir-Polder potential (green dash-dotted line). (c) Total trapping potential in the x - z plane. The cross-section of the nanofiber with a diameter of $2r_{\text{fiber}}=500$ nm is indicated as a white circle. (d) Axial cut through the total trapping potential.

perfectly π -polarized for $\phi = 0, \pi$. In this case, the local polarization is independent of the propagation direction.

2.2 Nanofiber-based two-color optical dipole trap

In the experiment, we want to optically interface cesium atoms using the evanescent field of the nanofiber. In order to achieve substantial and uniform atom-light coupling, we trap the atoms in the close vicinity of the nanofiber surface using a two-color optical dipole trap, see Fig 2.3(a) [76]. The blue detuned, running wave field has a wavelength of 760 nm and a power of 20.5 mW. The red-detuned, standing wave trapping field has a wavelength of 1064 nm and a total power of 2.4 mW. When calculating the trapping

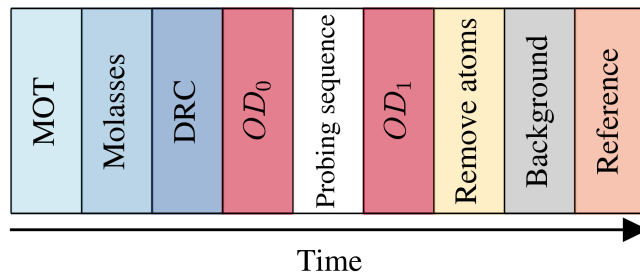


Figure 2.4: Schematic of the basic experimental sequence. Apart from the probing sequence and the reference, the sequence is the same for all experiments presented in this thesis.

potential, we take into account the scalar potentials induced by the two trapping fields as well as the attractive Casimir-Polder force [86, 87]. In Fig. 2.3(b), we plot these three components and the total trapping potential as a function of the radial distance from the fiber surface for an antinode of the red standing wave and $z = 0$. Since the decay constants for the two trapping light fields are different, the total potential features a minimum at a radial distance of about 230 nm from the nanofiber surface, with a potential depth of about 240 μK . Both trapping light fields are quasilinearly polarized. However, the blue trapping field is polarized orthogonally to the red trapping field, which strengthens the confinement in the azimuthal direction. As can be seen in Fig. 2.3(c), two potential minima are created on opposing sides of the fiber. Finally, the standing wave configuration of the red-detuned trapping laser field facilitates axial confinement. It creates a periodic modulation of the trapping potential in the axial direction, with a periodicity of about 500 nm, see Fig. 2.3(d). To summarize, the resulting trapping potential consists of two diametral arrays of trapping sites.

2.3 Experimental sequence

The basic structure of the experimental sequence used for all experiments presented in this thesis is schematically depicted in Fig. 2.4. We first trap and cool atoms using a magneto-optical trap (MOT), which is spatially overlapped with the nanofiber. The atoms are then further cooled using an optical molasses and probabilistically loaded into the two-color dipole trap [76]. Since our trap loading operates in the collisional blockade regime, at most one atom can be loaded into each potential minimum, which limits the average filling factor to $1/2$ [88]. After the loading, the atoms are trapped in two diametric arrays of trapping sites with random filling. We then apply a magnetic offset field of

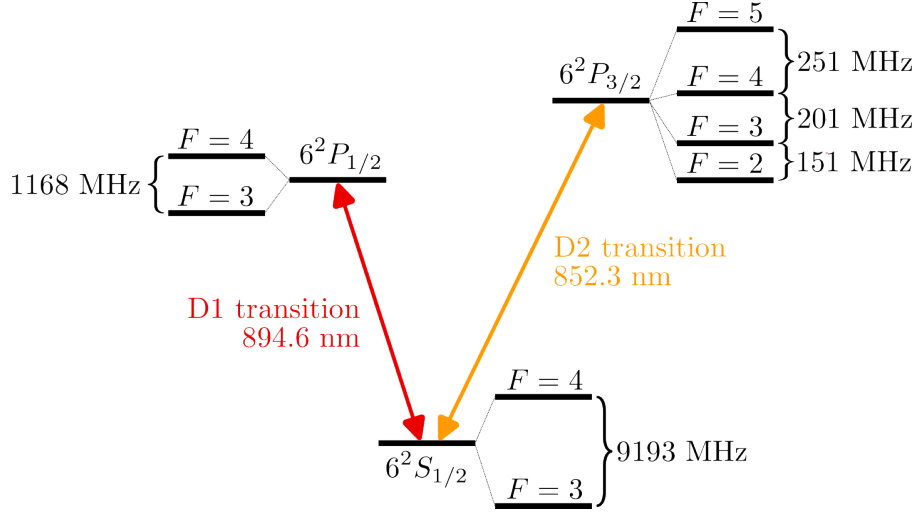


Figure 2.5: Relevant cesium energy levels. The two main transitions are denoted as D1 ($6^2S_{1/2} \rightarrow 6^2P_{1/2}$) and D2 ($6^2S_{1/2} \rightarrow 6^2P_{3/2}$). The values are taken from [89].

about 0.5 G in the $+z$ -direction and perform degenerate Raman cooling (DRC) with a fiber-guided laser field that is near-resonant with the $|6S_{1/2}, F=4\rangle \rightarrow |6P_{3/2}, F'=5\rangle$ D2 line transition, see Fig. 2.5 [90]. It is quasilinearly polarized along x . In this configuration, only σ^- -polarized light cools the atoms, while σ^+ -polarized light leads to degenerate Raman heating, where we have chosen the quantization axis along z . The atoms on one side of the fiber are thus expelled from their traps in about 20 ms, and we are left with a one-dimensional array of atoms, which are cooled close to their motional ground state [90]. In addition, DRC optically pumps the atoms to their outermost Zeeman sublevel, $|6S_{1/2}, F=4, m_F=-4\rangle$. This marks the end of our loading and preparation sequence. In order to infer the number of trapped atoms, we measure the optical depth of the nanofiber-trapped ensemble, OD_0 , in each sequence, see section 2.5. We then proceed with our probing sequence, which varies depending on the experiment, as detailed in chapters 4, 5, and 6. After the probing, we again measure the optical depth, OD_1 , in order to infer how many atoms were lost during the probing. Finally, we eject the atom from the trap by switching off the red trapping laser field for 6 ms, measure the detector background, and repeat the probing sequence without atoms for reference.

2.4 Detection setup

In our experiments, we are interested in both the light transmitted through the fiber (forward direction) and the backward scattered light. Therefore, we send the probe laser

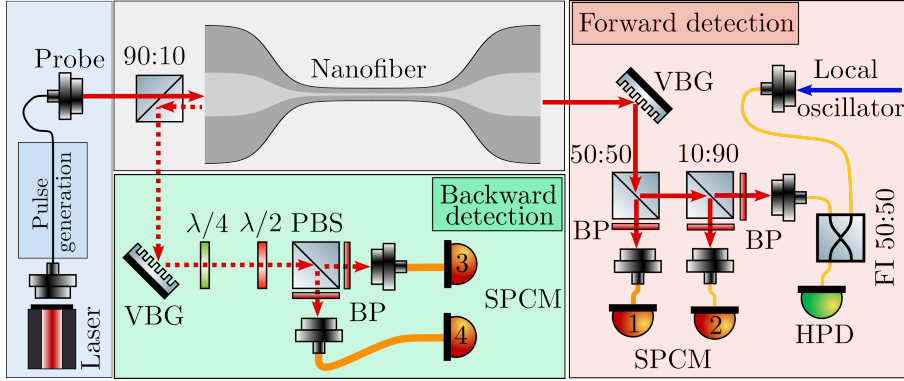


Figure 2.6: Schematic of the core elements of the detection setup in both forward and backward direction. Multi-mode and single-mode fibers are depicted as thick orange and thin yellow lines, respectively. The light is first spectrally band-pass-filtered around 852 nm using volume Bragg gratings (VBG) and band-pass filters (BP). Finally, the light is detected using single-photon counting modules (SPCM) and a hybrid photodetector (HPD). A local oscillator can be overlapped with the signal using a fiber-integrated 50:50 beamsplitter (FI).

field through a 10 : 90 beamsplitter before launching it into the nanofiber. This allows us to collect 90% of the backward-scattered photons. The detection setups in forward and backward directions are schematically depicted in Fig. 2.6. We typically excite and probe the atoms with fiber-guided laser pulses that are near-resonant to the D2 transition at a wavelength of 852 nm. In order to separate the signal from the trapping light fields and suppress other unwanted background light, the light is first spectrally band-pass-filtered around 852 nm using a volume Bragg grating in both forward and backward direction¹. An additional band-pass filter at 852 nm in front of each detector increases the spectral filtering even further². The background is then dominated by Raman scattering of the blue trapping laser field with the fiber material. This process also creates photons at 852 nm, which can therefore not be spectrally filtered [91]. The optical power of this background is about 0.5 pW. In the forward direction, the signal is split up and detected by two single-photon counting modules³ (SPCM) and one hybrid photodetector⁴ (HPD) in counting mode. SPCM 1 is used to measure the transmission spectrum, from which we infer the optical depth before and after each probing sequence. In principle, all detectors can be used to measure the transmitted power during the probing sequence. Depending on the experimental requirements, it is advantageous to use either the SPCMs,

¹OptiGrate, RBG-852-94

²Semrock, LL01-852-12.5

³Excelitas Technologies, SPCM-AQRH-14-FC

⁴Hamamatsu, HPD: R10467U-50, amplifier: C5594-22

the HPD, or both. The relevant specifications of the two detector types are summarized in Tab. 2.1. While the SPCMs feature a much larger quantum efficiency, the HPD has two key advantages. First, the dead time is about 15 times smaller than for the SPCMs, such that much higher count rates can be detected. Second, the HPD features negligible afterpulsing probability. This is particularly important in pulsed experiments, where the power of the atomic fluorescence can be much smaller than the excitation power, such that afterpulsing can be the limiting factor for the signal-to-noise ratio. Both the dark counts and the timing jitter of the two detectors are on the same order of magnitude and do not pose any significant limitation for our experiments.

Parameter	SPCM	HPD
Quantum efficiency [%]	50	12
Dark counts [Hz]	1000	2000
Timing jitter [ps]	350	130
Dead time [ns]	22	1.5
Afterpulsing probability [%]	0.5	negligible

Table 2.1: Comparison between the two detector types for key specifications.

For the heterodyne measurements in chapter 5, the signal field incident on the HPD is overlapped with a detuned local oscillator field using a fiber-integrated 90:10 beam splitter. In the backward direction, the signal is split up using a polarizing beam splitter (PBS), which can be used to select a particular polarization or in order to balance the detector counts. The signals at the two output ports of the PBS are then detected with SPCM 3 and 4.

2.5 Measurement of the optical depth

The optical depth of a medium, OD , is defined via the resonant power transmission coefficient of a weak probe field, $T = \exp(-OD)$. However, for large OD , the on-resonance transmission is very small and thus hard to measure. Instead, we infer the OD from transmission spectroscopy [76]. We sweep the frequency of a fiber-guided laser field over the $|6S_{1/2}, F = 4\rangle \rightarrow |6P_{3/2}, F' = 5\rangle$ D2 line transition and measure the transmitted power with an SPCM. The laser field is quasilinearly polarized along x , such that it is almost perfectly σ^- -polarized at the position of the atoms. It thus predominantly drives the cycling transition, $|6S_{1/2}, F = 4, m_F = -4\rangle \rightarrow |6P_{3/2}, F' = 5, m'_F = -5\rangle$. We also record a reference measurement without atoms and a background measurement, in which the laser is shut off, Fig. 2.7(a). This allows us to convert the photon counts to a transmission coefficient. We fit the resulting transmission spectrum to a saturated

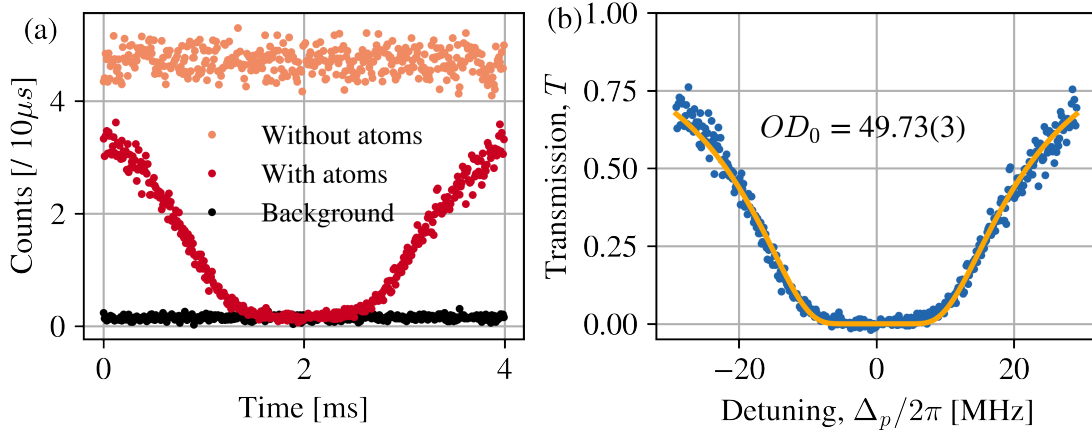


Figure 2.7: Measurement of the transmission spectrum in order to infer the OD . (a) Histogram of the detector counts as the frequency of a probe laser is scanned across resonance with atoms (red dots) and without atoms (light-red dots). The detector background is shown as black dots. (b) Using the data in (a), we compute a transmission spectrum. We fit a saturated Lorentzian profile and extract the OD , see orange solid line.

Lorentzian profile and extract the optical depth from the fit, see Figure 2.7(b).

2.6 Trapping lifetime

Without any cooling, the lifetime of the atoms in their trap is about 60 ms, see green dots in Fig. 2.8. By continuously cooling the atoms with a fiber-guided laser on the D2 line, as explained above, we can prolong the lifetime to about 1.3 s, see red squares in Fig. 2.8 [90]. However, since we are often interested in the light that the atoms scatter into the nanofiber-guided mode on the D2 transition, the cooling light constitutes an unwanted background. To mitigate this background, we can alternatively cool the atoms using a σ^- -polarized, free-space laser field that propagates in the $+z$ -direction. To further reduce signal pollution, we use a laser that is near-resonant with the $|6S_{1/2}, F = 4\rangle \rightarrow |6P_{1/2}, F' = 4\rangle$ D1-line transition. This light can then be easily separated from the D2-line signal by a spectral filter. DRC with the D1 laser is slightly less effective, and we find a lifetime of about 850 ms, see Fig. 2.8.

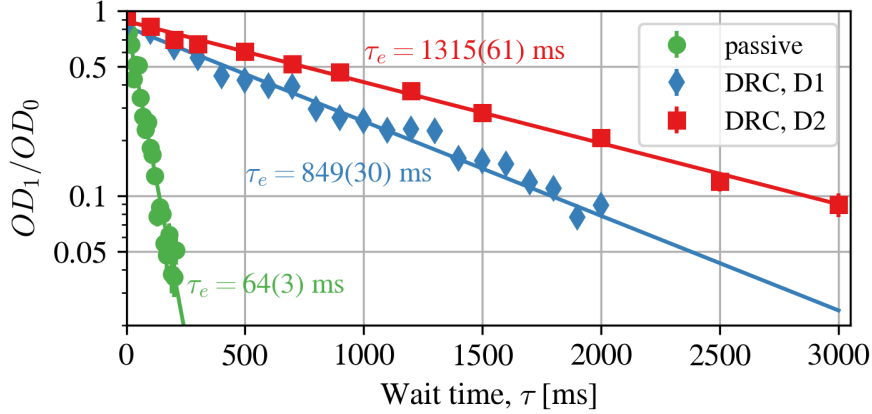


Figure 2.8: Lifetime of the trapped atoms without cooling, see green dots, and for two different realizations of DRC, see blue diamonds and red squares.

2.7 Measurement of the number of atoms

In order to measure the number of trapped atoms, we tune a fiber-guided laser field on resonance with the cycling transition and measure the power absorbed by the atoms as a function of the input power, see Fig. 2.9 [76]. By fitting to a saturation model⁵, we find that the fully saturated ensemble absorbs a power of $P_{\text{abs}}^{\text{max}} = 72(2)$ pW. We compare this to the power radiated by a single, fully saturated atom,

$$P_{\text{sat}} = \frac{\Gamma}{2} \hbar \omega \approx 3.8 \text{ pW}. \quad (2.1)$$

and infer the number of trapped atoms in this measurement, $N = P_{\text{abs}}^{\text{max}}/P_{\text{sat}} = 19.1(5)$. Together with the measured optical depth of $OD = 0.68(2)$, we infer an optical depth per atom of $OD_{\text{single atom}} = 0.036(3)$. This is in agreement with a direct measurement of the optical depth of a single atom, $0.039(1)$, which we carried out with a very similar trapping configuration [91].

2.8 Atom-light coupling strength

The atom-light coupling strength in a waveguide system is commonly quantified by the factors β_f and β_b , which denote the coupling strengths to the forward- and backward-

⁵Fitting function: $P_{\text{abs}}(P_{\text{in}}) = P_{\text{abs}}^{\text{max}} [1 + \exp(-bP_{\text{in}})]$

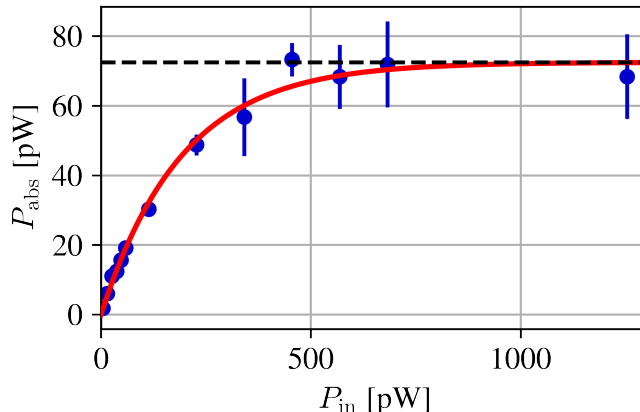


Figure 2.9: Measurement of the absorbed power, P_{abs} as a function of input power, P_{in} . We fit the data with a saturation model (red line) and use the power absorbed by a fully saturated ensemble to infer the number of trapped atoms, see black dashed line.

propagating modes, respectively [69],

$$\beta_f = \Gamma_f/\Gamma, \tag{2.2}$$

$$\beta_b = \Gamma_b/\Gamma. \tag{2.3}$$

Here, Γ_f and Γ_b denote the single-atom decay rates into the forward- and backward-propagating guided modes, respectively, and Γ the total decay rate. We define the forward direction as the $+z$ -direction, see Fig. 2.3(a), i.e., the direction in which we measure the optical depth. For $\beta_f \ll 1$, the optical depth of an ensemble of N atoms is given by $4\beta_f N$ [69], see Appendix A.1. Using the measurement of the number of atoms shown in Fig. 2.9, we infer $\beta_f = 0.009(1)$.

Theoretically, β_f and β_b are calculated as overlap integrals of the atomic radiation mode and the guided modes. This overlap integral depends on both the radial and azimuthal position of the atoms. In Fig. 2.10(a), we show the total coupling strength to the forward-propagating mode, β_f , as a function of the radial distance from the nanofiber surface, for $y = z = 0$ nm on a semi-log scale. We assume that the atom is initially prepared in $|6P_{3/2}, F = 5, m_F = -5\rangle$, such that the atomic fluorescence is perfectly σ^- -polarized. The evanescent field decays exponentially with a decay constant of about $k_f = \pi/\lambda_f$, where $\lambda_f \approx 745$ nm is the wavelength of the atomic transition in the nanofiber-guided mode. Therefore, also the coupling strength decreases exponentially.

The dashed black line indicates the position of the trapping minima, which occur at a radial distance of about 230 nm from the nanofiber surface. There, we expect a coupling

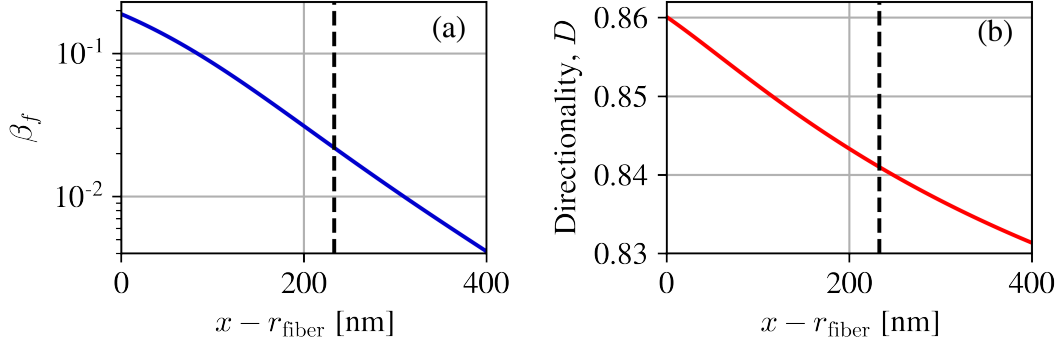


Figure 2.10: Calculated atom-waveguide coupling strength as a function of the distance from the nanofiber surface for $y = z = 0$ nm. We assume a σ^- -polarized atomic emission. (a) Coupling strength to the forward-propagating mode, β_f . (b) Directionality of the atom-waveguide coupling, D . The black dashed lines indicate the position of the trapping minima.

strength of about $\beta_f = 0.021$, which is more than twice as large as the measured value of 0.009(1). As described in Ref. [82], the mean distance from the nanofiber surface and the spread of the corresponding probability distribution increase with the atomic temperature since our trapping potential is not harmonic. Consequently, the mean coupling strength $\bar{\beta}$ decreases as the temperature increases. At the same time, the ratio between the standard deviation, σ_{β_f} , and the mean, $\bar{\beta}$, increases. However, most of the experiments described in this thesis are not carried out in thermal equilibrium, and it is challenging to measure or simulate the actual distribution of β_f values during the probing sequence. Therefore, we will not attempt to numerically model the thermal distribution of β_f -values, but rather fit it to our experimental observations, see section 3.7.

Since the local polarization of the nanofiber-guide mode depends on the propagation direction, the coupling strengths $\beta_{f,b}$ can be asymmetric too. To quantify this asymmetry, we introduce the directionality, D ,

$$D = \frac{\beta_f - \beta_b}{\beta_f + \beta_b}. \quad (2.4)$$

where, $D \in [-1, 1]$. Note that $D = 0$ corresponds to symmetric coupling, and $D = \pm 1$ means that the atoms exclusively couple to the forward- or backward propagating mode, respectively. In Fig. 2.10(b), we plot the directionality, D , as a function of the distance from the nanofiber surface for σ^- -polarized atomic fluorescence. The directionality varies only slightly with the distance to the nanofiber surface. At the position of the trapping minima, $D \approx 0.84$. This means that β_f is about 12 times larger than β_b , which was also

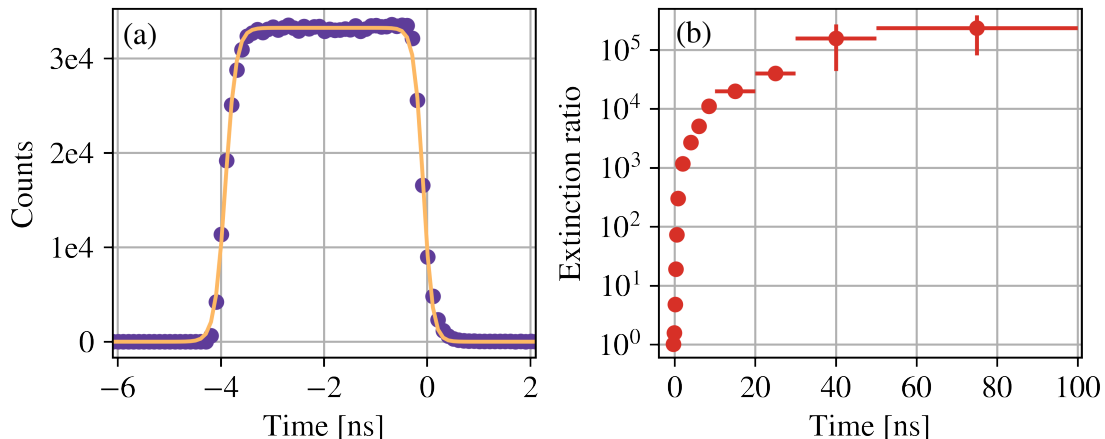


Figure 2.11: Optical pulse, derived from two cascaded Mach-Zehnder switches. (a) A fit (orange line) of the measured histogram of detector counts (purple dots) reveals a rise- and fall time of 454(3) ps and 394(3) ps, respectively. (b) Extinction ratio as a function of time after the switch-off. The horizontal error bars correspond to the widths of the time bins.

verified experimentally using our experimental setup [92]. This so-called chiral coupling enabled, e.g., the realization of optical non-reciprocal devices that are controlled by the atomic spin [69, 93]. We note that the directionality switches sign when the atoms emit σ^+ -polarized light. For π -polarized emission, the coupling is symmetric, i.e., $D = 0$.

2.9 Generation of nanosecond-long optical pulses

In section 4.1, we coherently excite the atoms with optical pulses that are much shorter than the 30.5 ns-lifetime of the $6P_{3/2}$ state [89]. These optical pulses are cut out from a continuous wave laser field using two fiber-integrated, commercial Mach-Zehnder interferometers (MZI) in series⁶. Both of these devices feature two electrical inputs, which can be used to tune the relative phase between the two interferometer arms. One input has a bandwidth on the order of about 1 kHz, while the second one features a much faster bandwidth on the order of 10 GHz. We apply a bias voltage to the slow input to set the MZIs to minimal transmission. We calibrate the bias voltages of both MZIs in every experimental sequence during the MOT loading phase in order to compensate for drifts. We use the slow input to scan the phase while monitoring the interferometer transmission with a photodiode. We then fit the resulting sinusoidal curve and set both interferometers to minimal transmission. In order to create an optical pulse, we then send an electrical

⁶Jenoptik, AM830, and AM830b

pulse into the fast input of the MZIs, with an amplitude that corresponds to a π phase shift. The electrical pulses are generated by an arbitrary waveform generator⁷. As a result, the MZIs switch to maximal transmission for the duration of the electrical pulse, and an optical pulse is created. In Fig. 2.11(a), we show a 4 ns-long optical pulse that was recorded with the HPD. By fitting both the first and second half of the pulse to a sigmoid function⁸, we extract a 10-90 rise- and fall time of 454(3) ps and 394(3) ps, respectively. We note that these times are upper bounds since the bandwidth of the oscilloscope and the timing jitter of the hybrid detector are on the same order of magnitude as the rise- and fall time, such that we are not sure if this measurement is limited by the optical pulse or by our detection. In (b), we show the measured extinction ratio as a function of time after switching off the pulse. The extinction ratio rises quickly and surpasses 10^3 after about 1.5 ns. After about 8 ns, the extinction ratio is larger than 10^4 , and for even larger times, we measure a maximum value of $2.5(1.5) \times 10^5$.

⁷Active Technologies, Arb Rider AWG-5062

⁸Fitting function: $S(t) = A / (1 + e^{\pm k(t-t_0)})$ for falling and rising edge, respectively. The 10-90 rise (and fall) times are given by $\tau = 2 \ln(9)/k$

3 Theoretical modeling

Before discussing our experimental results in chapters 4 and 5, we first introduce several theoretical models that will allow us to understand and interpret our measurements. We are interested in the dynamics of an ensemble of two-level atoms that interact via the shared nanofiber modes but can also independently decay into free space. In particular, we will focus on the cases relevant to our experimental implementation: we describe the optical excitation of the ensemble using nanofiber-guided optical pulses. Moreover, we will analyze the role of directional atom-waveguide coupling, as described in section 2.8. This chapter is organized as follows. First, we review linear response theory and an approach based on a many-body master equation. These two models are extensively described in the literature and serve as a reference for two new models: we describe two cascaded interaction models that allow us to approximately describe the dynamics even for large ensembles of atoms. Finally, we analyze the parameter regimes in which the different models are applicable.

3.1 Linear response theory

If the power of the excitation pulse is chosen to be so small that the probability to find each atom in the excited state, p_{exc} , practically vanishes, then the atoms behave like classical Lorentz oscillators. In this regime of linear optics, the field transmission spectrum for an ensemble of N atoms is given by the following expression, see Appendix A.3.1 for a derivation:

$$t_N(\Delta) = \left(1 - \frac{\beta_f \Gamma}{\Gamma/2 + i\Delta}\right)^N, \quad (3.1)$$

where Δ denotes the detuning from resonance and Γ the atomic population decay rate. For a given input field, $E_{\text{in}}(t)$, the time dynamics of the field transmitted through the ensemble, $E_f(t)$, can then be calculated using the following relation [46],

$$E_f(t) = \mathcal{F}^{-1}[\mathcal{F}[E_{\text{in}}(t)] \cdot t_N(\Delta)], \quad (3.2)$$

where \mathcal{F} and \mathcal{F}^{-1} denote the Fourier transform and its inverse, respectively. There is a wealth of collective radiative effects that occur in the weak excitation regime, many of which

have been experimentally observed [33, 36–40, 63, 94, 95]. In particular, superradiance (subradiance) has been observed in ensembles of waveguide-coupled atoms, evidenced by a collectively enhanced (inhibited) decay [42–47]. However, linear response theory only describes a narrow range of the entire Hilbert space. In this work, we are interested in the collective radiation of atoms beyond the linear regime, i.e., where the excited state probability is not negligible anymore.

3.2 Many-body master equation

A more general solution to this problem that goes beyond linear response theory has been treated many times in literature. Usually, the electromagnetic field is traced out within the Born-Markov approximation, which leads to a many-body master equation for the atomic density matrix, $\hat{\rho}$ [41, 96, 97],

$$\dot{\hat{\rho}} = -\frac{i}{\hbar} [\hat{\mathcal{H}}, \hat{\rho}] + \mathcal{L}[\hat{\rho}]. \quad (3.3)$$

Here, $\hat{\mathcal{H}}$ is an effective Hamiltonian, and \mathcal{L} describes dissipation. Within the rotating wave approximation and in a frame rotating at the laser frequency, they read

$$\hat{\mathcal{H}} = \hbar\Delta \sum_{i=1}^N \hat{\sigma}_i^\dagger \hat{\sigma}_i + \sum_{i=1}^N \hbar\Omega_i (\hat{\sigma}_i^\dagger + \hat{\sigma}_i) + \sum_{i,j=1}^N \hbar J_{ij} \hat{\sigma}_i^\dagger \hat{\sigma}_j \quad (3.4)$$

$$\mathcal{L}[\hat{\rho}] = \sum_{i,j=1}^N \frac{\Gamma_{ij}}{2} \left(2\hat{\sigma}_i \hat{\rho} \hat{\sigma}_j^\dagger - \hat{\rho} \hat{\sigma}_j^\dagger \hat{\sigma}_i - \hat{\sigma}_j^\dagger \hat{\sigma}_i \hat{\rho} \right), \quad (3.5)$$

where $\hat{\sigma}_i = |g\rangle_i \langle e|_i$ denotes the atomic lowering operator of the i th atom, with ground and excited state, $|g\rangle_i$ and $|e\rangle_i$, respectively. The first and second terms in the effective Hamiltonian describe the free evolution of the atoms and the optical drive, respectively. The driving strength is quantified by a complex-valued Rabi frequency, Ω_i , and the laser detuning from resonance is denoted Δ . The third term describes the coherent interaction between different atomic spins, with an amplitude J_{ij} . This term represents a flip-flop interaction, where one atom emits a photon into the guided mode, which is then reabsorbed by another atom. This process is equivalent to a dipole-dipole interaction, which is mediated by the guided mode. The dissipative terms, $\mathcal{L}[\hat{\rho}]$, describe the incoherent atomic decay rates, Γ_{ij} , which are modified due to the shared radiation mode. In general, J_{ij} and Γ_{ij} are proportional to the real and imaginary parts of the Green's function of the system, respectively. Since the average interatomic distance in our experiment is larger

than half the free-space wavelength of the radiation, we neglect any interatomic coupling via free space [98], and J_{ij} and Γ_{ij} take a particularly simple form [99],

$$J_{ij} = -\frac{i}{2} \left[\beta_f \Gamma e^{ik_f(z_i - z_j)} - \beta_b \Gamma e^{-ik_f(z_i - z_j)} \right] \text{sign}(i - j), \quad (3.6)$$

$$\Gamma_{ij} = \beta_f \Gamma e^{-ik_f(z_i - z_j)} + \beta_b \Gamma e^{+ik_f(z_i - z_j)} + \delta_{ij} \Gamma_0, \quad (3.7)$$

where Γ_0 denotes the decay rate into free space, such that the total decay rate is given by the sum $\Gamma = \Gamma_0 + \beta_f \Gamma + \beta_b \Gamma$. Importantly, since the interaction is mediated by a guided mode, the interaction strength does not decay with the interatomic distance, i.e., the dipole-dipole interaction is effectively “infinite-ranged” [43]. However, we note that the interaction strength eventually does decay, e.g., due to losses in the fiber and retardation effects. Both of these effects are negligible on the scale of a few mm, over which we trap our atoms. Once we have solved equation (3.3) for the atomic density matrix, $\hat{\rho}(t)$, we can calculate the field and power exiting the nanofiber in the forward (backward) direction, respectively,

$$E_f = E_{\text{in}} - i\sqrt{\beta_f \Gamma} \sum_{i=1}^N e^{-ik_f z_i} \langle \sigma_i \rangle, \quad (3.8)$$

$$P_f = P_{\text{in}} + \beta_f \Gamma \sum_{i,j=1}^N e^{ik_f(z_i - z_j)} \langle \hat{\sigma}_i^\dagger \hat{\sigma}_j \rangle - i\sqrt{\beta_f \Gamma P_{\text{in}}} \sum_{i=1}^N \left(e^{-ik_f z_i} \langle \hat{\sigma}_i \rangle - c.c. \right), \quad (3.9)$$

$$E_b = -i\sqrt{\beta_b \Gamma} \sum_{i=1}^N e^{ik_f z_i} \langle \sigma_i \rangle, \quad (3.10)$$

$$P_b = \beta_b \Gamma \sum_{i,j=1}^N e^{-ik_f(z_i - z_j)} \langle \hat{\sigma}_i^\dagger \hat{\sigma}_j \rangle. \quad (3.11)$$

Here, P_{in} denotes the input power of the fiber-guided, forward-propagating driving field and E_{in} the corresponding electric field, which we assume to be real-valued. Note that we have chosen the unit of the power to be photons per second. The unit of the electric field is chosen such that $P_{\text{in}} = |E_{\text{in}}|^2$. The second term in Eq. (3.9) describes light that is emitted spontaneously by the atoms, while the third term represents the coherently scattered light. Since the density matrix $\hat{\rho}$ has 2^{2N} entries, the computational complexity of solving Eq. (3.3) is exponential in the number of atoms. Therefore, we can only simulate the dynamics of about ten atoms using a standard desktop computer. However, in our experiment, we trap up to 1000 atoms, such that solving the many-body master equation is generally impossible, even for the most advanced supercomputers.

We note that the system is exactly solvable when the atoms feature particle exchange

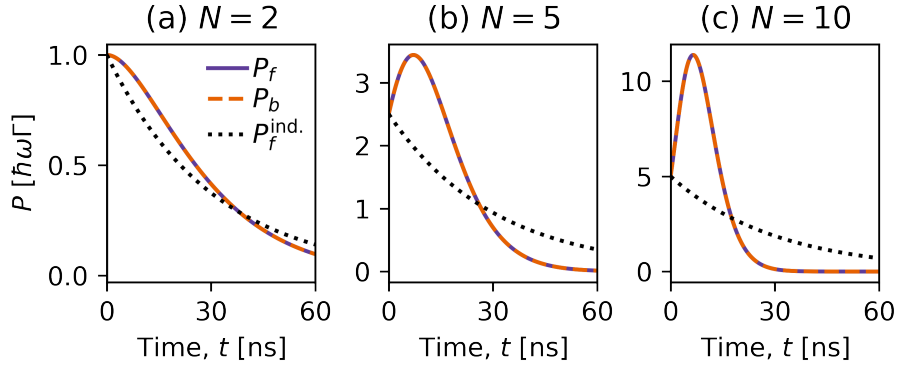


Figure 3.1: Ideal Dicke superradiance. Power emitted into the waveguide modes, P_f and P_b , simulated by solving the many-body master equation for $N = 2, 5$, and 10 initially inverted atoms in (a), (b), and (c), respectively. We assume $\beta_f = \beta_b = 0.5$ and the Bragg configuration. For this setting, the many body master equation is equivalent to that of ideal Dicke superradiance. The case of N independently emitting atoms is shown as a black dotted line for reference.

symmetry since the dynamics is then restricted to the completely symmetric, so-called Dicke states [9]. Particle-exchange symmetry can be realized by placing the atoms in a volume that is much smaller than the wavelength of the radiation or by placing the atoms in a high-finesse cavity [10]. In waveguide QED, particle exchange symmetry can be achieved for unity symmetric coupling, i.e., $\beta_f = \beta_b = 0.5$. In addition, an interatomic spacing of $n\lambda_f/2$ is required, where n is a natural number, and λ_f is the transition wavelength inside the nanofiber. In the following, we will call this the Bragg configuration. When these two requirements are met, the amplitudes J_{ij} vanish and the master equation, Eq. (3.3), is identical to the master equation of ideal Dicke superradiance, see Appendix A.4 and Ref. [99]. In particular, when all atoms are initially prepared in the excited state, $|e\rangle$, ideal Dicke superradiance predicts the emission of short, intense bursts of light [9, 10], which stems from a spontaneous synchronization of the atomic dipoles during their decay. However, our experimental platform neither features unity atom-waveguide coupling nor an atomic spacing commensurate with $\lambda_f/2$. Thus, our system does not feature particle-exchange symmetry. In the following three subsections, we will first show the dynamics of the power emitted into the waveguide for the ideal Dicke case and analyze the effect of directional atom-waveguide coupling. Then we will discuss the role of non-unity atom-waveguide coupling. Finally, we will analyze the effect of spatial disorder along the axial direction.

3.2.1 Dicke superradiant bursts

In Fig. 3.1, we show the power that an initially fully inverted ensemble emits into the waveguide modes for $N = 2, 5$, and 10 atoms in (a), (b), and (c), respectively. As a reference, we show the dynamics of the power for N independently emitting atoms, i.e., an exponential decay with the rate Γ , as a black dotted line. Here, we choose $\beta_f = \beta_b = 0.5$, and atomic positions $z_k = n\lambda_f/2$, where n denotes the n th atom. This setting realizes the ideal Dicke case. Since the system is symmetric with respect to the forward- and backward-propagating modes, the dynamics of P_f and P_b are exactly the same, see solid purple and dashed orange lines, respectively.

For two inverted atoms, see panel (a), we already observe non-exponential decay dynamics. As we increase the atom number further, we observe that the emitted powers first increase, reach peak values of P_f^{\max} and P_b^{\max} , and then decrease. This behavior is the characteristic feature of superradiant burst dynamics, which can be understood as a spontaneous synchronization of the atomic dipoles during their decay. Once they have synchronized, each atom adds constructively to the macroscopic dipole moment of the ensemble. Since the emitted power is proportional to the square of the dipole moment, the peak-emitted power increases quadratically with the number of atoms, N [9, 10].

3.2.2 Asymmetric atom-waveguide coupling strength

As described in section 2.8, the atom-waveguide coupling strength in our experiment can be asymmetric, i.e., $\beta_f \neq \beta_b$. In order to quantify this asymmetry, we introduced the directionality, D ,

$$D = \frac{\beta_f - \beta_b}{\beta_f + \beta_b}. \quad (3.12)$$

In particular, when driving the atoms on the $|6S_{1/2}, F = 4, m_F = -4\rangle \rightarrow |6P_{3/2}, F = 5, m_F = -5\rangle$ cycling transition, the emitted light is σ^- -polarized. In our experiment, the coupling strength to the forward-propagating mode is then about 12 times larger than the coupling strength to the backward-propagating mode, i.e., $D = 0.84$, see section 2.8.

In order to illustrate the effect of directional atom-waveguide coupling, we solve the many-body master equation for 10 initially inverted atoms for different directionalities, D , while keeping the total coupling strength constant, $\beta_f + \beta_b = 1$. As before, we assume that the atoms are arranged in the Bragg configuration. We plot the resulting dynamics of the forward-emitted power, P_f , in Fig. 3.2(a). Note that we divide the power, P_f , by β_f to better compare the different configurations. While the peak-emitted power is largest in the case of symmetric coupling, i.e., $D = 0$, we initially observe very similar burst

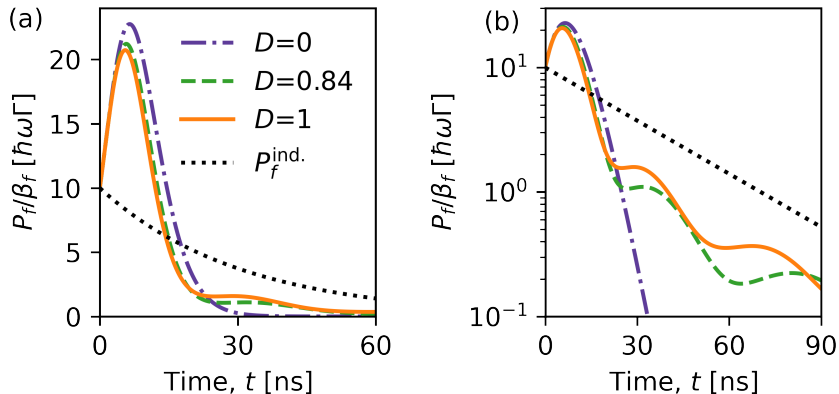


Figure 3.2: (a) Effect of the directionality of atom-waveguide coupling, D , on the emission dynamics. We solve the many-body master equation for 10 atoms that are fully inverted at time $t = 0$ ns. We assume that the atoms are arranged in the Bragg configuration. We fix the total coupling strength to $\beta_f + \beta_b = 1$ and show the predictions for the power emitted into the forward direction, P_f , for different directionalities, D . Note that we divide the power P_f by the respective coupling strength to the forward-propagating mode, β_f . Panel (b) shows the same data as (a) on a semi-log scale to highlight the dynamics at large t .

dynamics for all directionalities.

However, for times larger than about 20 ns, the dynamics in the case of directional coupling is qualitatively very different from the ideal Dicke case. To highlight these differences, we plot the data shown in panel (a) on a semi-log scale in panel (b). For symmetric coupling ($D = 0$), the power converges to an exponential decay after some time. The corresponding decay constant is given by $N\Gamma$, which is the decay constant expected for the symmetric Dicke state in the single-excitation manifold [33]. The decay at longer times is thus much faster than that of independently emitting atoms (see dotted black line). In contrast, for directional coupling ($D > 0$), we observe non-exponential decay dynamics. In particular, we observe several minima of the power, P_f , which indicate that the ensemble populates subradiant states, i.e., decay is momentarily inhibited.

While it is an intriguing research direction to study the origin of this effect, we will only shortly revisit the subradiant dynamics in section 5.6. Instead, the main focus of this thesis will lie on the early superradiant dynamics. Importantly, the dynamics for the maximally achievable directionality in our experiment, $D = 0.84$, is almost the same as the dynamics for unidirectional coupling, $D = 1$. This will motivate our assumption of unidirectional coupling later on, see sections 3.3 and 3.4.

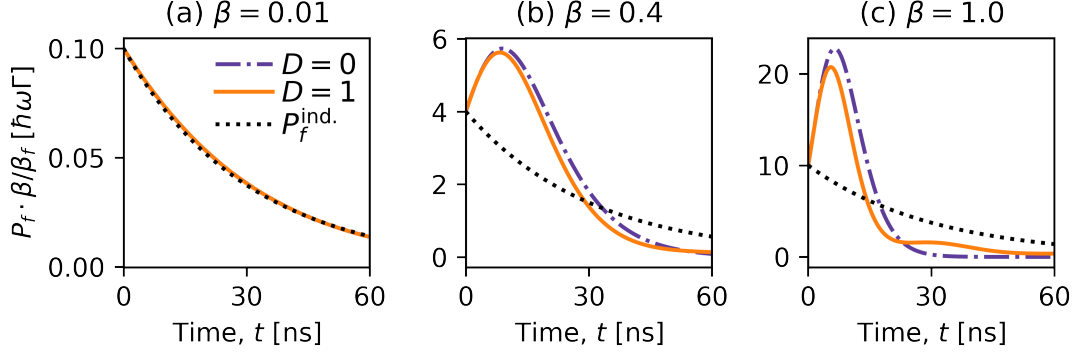


Figure 3.3: Influence of imperfect atom-waveguide coupling on the superradiant burst dynamics. We show the powers, P_f , that an ensemble of $N = 10$ initially inverted atoms emit into the nanofiber-guided modes for three different atom-waveguide coupling strengths, $\beta = \beta_f + \beta_b$. We again assume the Bragg configuration and show the predictions for both symmetric ($D = 0$) and unidirectional $D = 1$ coupling. Superradiant burst dynamics disappears as β decreases, independently of the directionality. Note that P_f is rescaled by the factor β/β_f .

3.2.3 Imperfect atom-waveguide coupling strength

In our experiment, the atom-waveguide coupling strength is far from unity, $\beta = \beta_f + \beta_b \approx 0.01$, meaning that a single atom emits about 1 % of its light into the nanofiber-guided modes, while 99 % of the light is emitted into independent free-space modes, see section 2.8.

In Figs. 3.3, we plot the dynamics of the forward-emitted power, P_f , for $N = 10$ initially inverted atoms for different β . We plot the dynamics for both symmetric $D = 0$ and unidirectional ($D = 1$) coupling, see dash-dotted purple and solid orange lines, respectively. As before, we assume the Bragg configuration. Note that we scale P_f by the factor β/β_f . In other words, we multiply P_f for symmetric coupling by two to better compare the dynamics with the case of unidirectional coupling.

For $\beta = 0.4$ in panel (b), we observe that the superradiant burst is slightly less pronounced compared to the case of unity coupling in (c). As we decrease β to the value expected in our experiment, $\beta = 0.01$ in (a), the dynamics almost coincides with that of an ensemble of independently decaying atoms, see dotted black line. This suggests that the superradiant burst dynamics is inhibited by the decay into free space, independent of the directionality. This can be understood as a consequence of competition between decay into the guided modes and the independent decay into free-space modes. Superradiant burst dynamics for a fully inverted ensemble occurs because the initial vacuum fluctuation that triggers

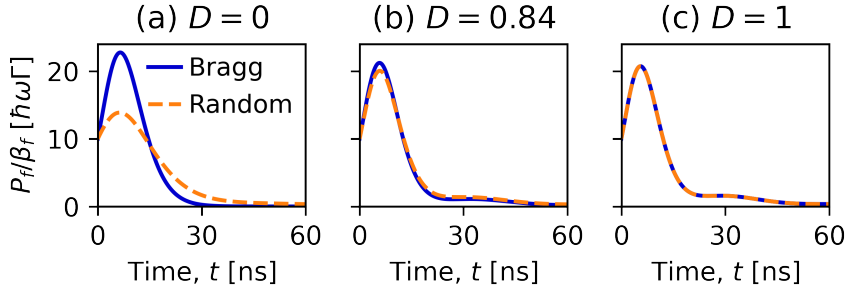


Figure 3.4: Effect of spatial disorder on the emission dynamics for different directionalities, D . We simulate the dynamics of P_f/β for 10 initially fully inverted atoms and $\beta = 1$. We show the dynamics for the Bragg configuration and random atomic positions as the blue solid and dashed orange lines, respectively. Notably, the dynamics is unaffected by the spatial disorder for unidirectional coupling, see panel (c).

the emission process is amplified as the atoms decay [10]. This leads to a build-up of coherence, i.e., the atomic dipoles synchronize their phases. Any decay into the free space modes dephases the atomic dipoles, such that the superradiant burst dynamics is quenched.

Importantly, superradiant dynamics can always be recovered by increasing the atom number. An analytic expression for the minimal atom number at which burst dynamics occurs has recently been derived for fully inverted, waveguide-coupled ensembles [99]. For the Bragg configuration, one obtains

$$N_{\text{Bragg}} = 1 + \frac{1}{\beta}. \quad (3.13)$$

For the Bragg configuration, this threshold is thus independent of the directionality. Intuitively, one can understand the expression in Eq. (3.13) as the number of atoms for which, initially, the atomic ensemble emits at a rate into the waveguide that exceeds the independent decay rate of a single atom, $\beta\Gamma N > \Gamma$. However, while nanofiber-based optical lattices with Bragg spacing have been experimentally realized [100, 101], they are challenging to implement. In the following, we will analyze the dynamics in the presence of spatial disorder in the axial direction.

3.2.4 Spatial disorder

In our experiment, we probabilistically load an optical lattice with a maximal filling fraction of 0.5, see section 2.3. Since our lattice spacing, $d \approx 500$ nm, is incommensurate

with the in-fiber resonant optical wavelength, $\lambda_f = 745$ nm, we can assume that the spacing is effectively random. Indeed, one can show that the phases of $e^{ik_f z_n}$ are homogeneously sampled, where z_n denotes the z -position of the n th atom [81, 91]. Therefore, we model the spatial disorder along the axial direction in our experiment by averaging the simulation results over 10 randomly chosen configurations of atomic positions, z_i . In Figs. 3.4, we plot the dynamics of the forward-emitted power, P_f , divided by β , for 10 initially inverted atoms for both the Bragg configuration and random atomic positions. In panel (a), we choose symmetric coupling, $D = 0$, and observe that the superradiant burst for random atomic positions is less pronounced than for the Bragg configuration. For random spacing, coherence can either be built up with respect to the forward- or backward-propagating mode, meaning that the atomic dipoles feature phases that are given by the corresponding propagation phases. The latter are $e^{ik_f z_i}$ and $e^{-ik_f z_i}$ for the forward and backward-propagating modes, respectively, and are generally not the same. Therefore, decay into the backward-propagating mode dephases the coherence that is built up with respect to the forward-propagating mode and vice versa. This leads to quenching of the superradiant burst.

In panel (c), we show the same simulation for unidirectional coupling, i.e., $D = 0$. There, the dynamics is completely independent of the axial atomic positions since there is no dephasing due to decay into the backward-propagating mode. We thus conclude that spatial disorder does not affect superradiant burst dynamics for unidirectional coupling. In panel (b), we choose the directionality expected in our experiment, $D = 0.84$. While we observe a slight quenching of the superradiant burst for random atomic positions, the effect is much less than for symmetric coupling, see (a).

One can also find an analytical expression for the threshold beyond which superradiant bursts occur for random atomic positions [99],

$$N_{\text{Random}}(D) = \frac{\beta(\beta + 1)}{\beta_f^2 + \beta_b^2} = \frac{2(\beta + 1)}{\beta(1 + D^2)}, \quad (3.14)$$

$$N_{\text{Random}}(D = 1) = 1 + \frac{1}{\beta} = N_{\text{Bragg}}, \quad (3.15)$$

$$N_{\text{Random}}(D = 0) = 2 \left(1 + \frac{1}{\beta} \right) = 2N_{\text{Bragg}}. \quad (3.16)$$

In contrast to the case of Bragg spacing, the threshold for random atomic positions does depend on the directionality of the atom-waveguide coupling strength, D . In particular, the threshold for unidirectional coupling is the same as for the Bragg configuration. For symmetric coupling, the threshold is exactly twice as large. For random atomic positions, one can thus reduce the threshold atom number by up to a factor of two by engineering an

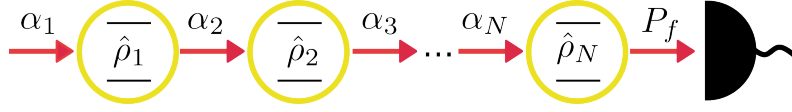


Figure 3.5: Schematic representation of the cascaded interaction model. Each atom, with index k , is driven by a light field with amplitude α_k , which only depends on the dynamics of upstream atoms. Each atom is described by a single-atom density operator, $\hat{\rho}_k$. Finally, we compute the output power P_f .

asymmetric atom-waveguide coupling. For $\beta = 0.01$ and symmetric coupling, we obtain, $N_{\text{Random}}(D = 0) = 202$ and $N_{\text{Bragg}(D=1)} = 101$. For the directionality in our experiment, the expected threshold is $N_{\text{Random}}(D = 0.84) = 118$.

In order to reach the regime of superradiant burst dynamics, we thus still have to invert hundreds of atoms for a unidirectional coupling strength of $\beta_f = 0.01$. Solving the full master equation for such large ensembles is prohibitive, see section 3.2.

3.3 Coherent state approximation

In the following two sections, we will describe two new models to describe the collective radiative dynamics of ensembles of two-level atoms that are unidirectionally coupled to a waveguided mode. We will use the asymmetry of the atom-light coupling strength and describe the light field classically to simplify our calculations and greatly reduce the computational complexity of our modeling. Since we can prepare the atoms in a state in which their coupling to the forward propagating mode is about 12 times larger than the coupling to the backward-propagating mode [92], we assume unidirectional coupling in the following, i.e., $\beta_b = 0$. The system then constitutes a cascaded quantum system, in which the dynamics of each atom is only determined by the dynamics of upstream atoms [74, 75]. Such a cascaded interaction is schematically depicted in Fig. 3.5. Each atom, with index k , is described by a single-atom density matrix, $\hat{\rho}_k$, and is exposed to a light field α_k . Our first task is to simulate the atomic response of the first atom to the input field, α_1 . Then, we compute the light field after the first atom, α_2 , which then drives the second atom, and so on. This way, we can propagate the light field through the ensemble to finally compute the output power, P_f , which we measure in our experiment.

As a first approximation, we assume that each atom is solely driven by the coherent part of the light field scattered by the previous atom, with amplitude α_k^c . In the following, we will call this approach ‘‘coherent state approximation’’ (CSA). Note that, for resonant excitation, we can choose $\alpha_k^c \in \mathbb{R} \forall k$ without loss of generality. For the first atom, the time-dependent driving field is given the excitation laser, $\alpha_1 = \sqrt{P_1}$. For all other

atoms, we determine the field α_{k+1}^c , and the corresponding power, P_{k+1} , via the following input-output equations [102]:

$$\alpha_{k+1}^c = \alpha_k^c - i\sqrt{\beta_f\Gamma}\hat{\rho}_k^{eg}, \quad (3.17)$$

$$P_{k+1} = P_k + \beta_f\Gamma\hat{\rho}_k^{ee} + 2\sqrt{\beta_f\Gamma}\text{Im}(\alpha_k^*\hat{\rho}_k^{eg}) \quad (3.18)$$

$$= |\alpha_{k+1}^c|^2 + \beta_f\Gamma\left(\hat{\rho}_k^{ee} - |\hat{\rho}_k^{eg}|^2\right), \quad (3.19)$$

where $\text{Im}(\dots)$ denotes the imaginary part and $*$ denotes complex conjugation. In order to solve these input-output equations, we have to know the dynamics of the density matrix of atom k . Therefore, we solve the single-atom Lindblad master equation for each atom k [103, 104]

$$\dot{\hat{\rho}}_k = -\frac{i}{\hbar}\left[\hat{\mathcal{H}}_k, \hat{\rho}_k\right] + \mathcal{L}[\hat{\rho}_k]. \quad (3.20)$$

Here, $\hat{\mathcal{H}}_k$ is a semi-classical Hamiltonian assuming that the k th atom is resonantly driven by a time-dependent coherent light field with Rabi frequency $\Omega_k = \sqrt{4\beta_f\Gamma}\alpha_k$, and \mathcal{L} is the Lindblad superoperator describing spontaneous emission with decay rate Γ ,

$$\hat{\mathcal{H}}_k = \frac{\hbar\Omega_k}{2}\left(\hat{\sigma}_k^\dagger + \hat{\sigma}_k\right), \quad (3.21)$$

$$\mathcal{L}[\hat{\rho}_k] = \Gamma\left[\hat{\sigma}_k\hat{\rho}_k\hat{\sigma}_k^\dagger - \frac{1}{2}\left(\hat{\sigma}_k^\dagger\hat{\sigma}_k\hat{\rho}_k + \hat{\rho}_k\hat{\sigma}_k^\dagger\hat{\sigma}_k\right)\right]. \quad (3.22)$$

In chapter 4, we will see that, surprisingly, the CSA describes the dynamics of the power of the light exiting the nanofiber, P_f , over a relatively wide range of parameters in our experiment. Importantly, however, the assumption of a coherent drive is not justified for an ensemble close to full inversion. Indeed, from Eq. (3.19), it is clear that $P_{k+1} \neq |\alpha_{k+1}^c|^2$, i.e., that the field is not in a coherent state. Then, the atoms are also driven by the incoherent light that other atoms emit into the nanofiber mode, which is not captured by the CSA. In particular, in the singular case of a perfectly inverted ensemble, the CSA prediction coincides with the prediction for independently emitting atoms, i.e., an exponential decay.

3.4 Mixed coherent state approximation

In this section, we present a modification of the CSA that allows us to phenomenologically model how the atoms are driven by the incoherent part of the light. In the CSA, we restrict the field to the rotating frame of the excitation laser field, i.e., $\alpha_k^c \in \mathbb{R} \forall k$. This means that the atoms are only driven by light fields that are either in phase or π out of phase

with the excitation laser field. However, spontaneously emitted photons do not feature any fixed phase relationship to the excitation laser field. To emulate this incoherent light, we describe the light field impinging on the k th atom as a mixture of coherent states with amplitude $\alpha_k^c + e^{i\phi}\alpha_k^{\text{inc}}$, and homogeneously sample the phase ϕ over $[0, 2\pi)$. The density matrix of this mixture of coherent states is then given by

$$\rho_{\text{MCS}} = \frac{1}{2\pi} \int_0^{2\pi} d\phi |\alpha_k^c + e^{i\phi}\alpha_k^{\text{inc}}\rangle \langle \alpha_k^c + e^{i\phi}\alpha_k^{\text{inc}}|, \quad (3.23)$$

where $|\alpha\rangle$ represents a coherent state with a time-dependent amplitude of $\alpha \in \mathbb{C}$. In the following, we will call this approach ‘‘mixed coherent state approximation’’ (MCSA). Importantly, the newly introduced, incoherent amplitude, α_k^{inc} , is chosen such that the total power is given by eq. (3.19),

$$\alpha_k^{\text{inc}} = \sqrt{P_k - |\alpha_k^c|^2}. \quad (3.24)$$

We can visualize the mixed coherent state by plotting, e.g., its Husimi Q representation, which is defined as [104]

$$Q(\alpha) = \frac{1}{\pi} \langle \alpha | \rho_{\text{MCSA}} | \alpha \rangle. \quad (3.25)$$

It represents a quasiprobability distribution in phase space and can, e.g., be used to graphically illustrate the properties of a light field. While it is normalized, $\int Q(\alpha) d\alpha = 1$, and non-negative, it is not a proper probability distribution since the coherent states $\{|\alpha\rangle\}$ are not orthogonal. In Fig. 3.6, we plot the Q function for three example mixed coherent states. In (a), the incoherent amplitude is zero, such that the mixed coherent state is equivalent to a pure coherent state with a real-valued amplitude. In (c), the coherent amplitude is zero, such that the Husimi Q representation becomes symmetric with respect to the origin. This means that there is no preferred phase, as expected for a fully incoherent light field. In (b), we show a mixed coherent state with equal coherent and incoherent amplitudes. There, the center of the circle (i.e., the expectation value of the field) is given by the coherent amplitude, α^c , while the radius of the circle is determined by the incoherent amplitude, α^{inc} . We can compute the expectation value for the field and power when the light field is in the mixed coherent state:

$$\alpha_{\text{MCS}} = \frac{1}{2\pi} \int_0^{2\pi} d\phi (\alpha^c + e^{i\phi}\alpha^{\text{inc}}) = \alpha^c, \quad (3.26)$$

$$P_{\text{MCS}} = \frac{1}{2\pi} \int_0^{2\pi} d\phi |\alpha^c + e^{i\phi}\alpha^{\text{inc}}|^2 = |\alpha^c|^2 + |\alpha^{\text{inc}}|^2. \quad (3.27)$$

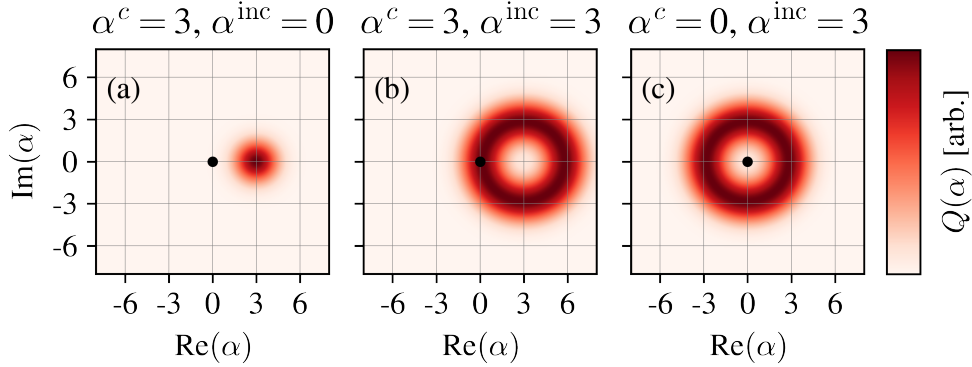


Figure 3.6: Husimi Q representation of mixed coherent states with different coherent and incoherent amplitudes. $\text{Re}(\dots)$ and $\text{Im}(\dots)$ denote the real and imaginary parts, respectively.

Note that, while each pure state in the mixture is coherent, the mixed coherent state loses an important property of a coherent state, i.e., $P_{\text{MCS}} \neq |\alpha_{\text{MCS}}|^2$.

As in the CSA, we can now solve the single-atom Lindblad master equation and the input-output equation, this time with a drive field in the mixed coherent state. Specifically, this means that we solve the master equation for the k th atom by assuming a coherent drive field with an amplitude $\alpha_k = \alpha_k^c + e^{i\phi} \alpha_k^{\text{inc}}$. We thus obtain solutions for the atomic density matrix, $\rho_k^\phi(t)$, for each phase ϕ . Similarly, by applying the input-output formalism in Eqs. (3.17)-(3.19), we find ϕ -dependent output fields and powers, α_{k+1}^ϕ and P_{k+1}^ϕ . Finally, we compute the expectation values for the field and power by tracing over the phase ϕ ,

$$P_{k+1} = \frac{1}{2\pi} \int_0^{2\pi} d\phi P_{k+1}^\phi \quad (3.28)$$

$$\alpha_{k+1} = \frac{1}{2\pi} \int_0^{2\pi} d\phi \alpha_{k+1}^\phi. \quad (3.29)$$

We note that, numerically, the integral over ϕ is approximated as a sum over a certain number of ϕ -values. Intuitively, one could suspect that the sampling has to be finer for a larger incoherent amplitude, α^{inc} , since the radius of the circle in the Husimi Q representation is proportional to α^{inc} . However, we numerically found that the simulation results converge for about 4 ϕ -values, even for large ensembles with up to 10^4 atoms. For all MCSA simulations presented in this thesis, we sample over 20 ϕ -values.

3.5 Comparison of the different approaches

3.5.1 Benchmarking using the many-body master equation

On a standard desktop computer, the many-body master equation can only be solved for about 10 atoms in a reasonable amount of time. We compare the different models by simulating time traces of the power that an ensemble of $N = 10$ atoms emits into the forward propagating mode. In order to observe dynamics with collective features for only 10 atoms, we increase the coupling strength to $\beta_f = 0.4$. Again, we neglect the coupling to the backward-propagating mode, i.e., we assume that $\beta_b = 0$. Moreover, we neglect the excitation dynamics and start our simulations with all atoms in state $|\psi_0\rangle$,

$$|\psi_0\rangle = \cos\left(\frac{A}{2}\right)|g\rangle - i\sin\left(\frac{A}{2}\right)|e\rangle. \quad (3.30)$$

Since linear response theory is only applicable for an incident excitation pulse, we don't include it in our comparison in this section. Here, A denotes the pulse area for excitation pulses much shorter than the excited state lifetime. Note that we have chosen the rotating frame of a nanofiber-guided excitation laser field. This means that, in the lab frame, each atom is excited with a phase $\exp(ik_f z_n)$, where k_f denotes the wave vector of the nanofiber-guided mode and the z_n the axial atomic position. We chose this particular subclass of states because we will use fiber-guided excitation pulses to prepare the ensemble in the desired states later on, which will imprint exactly this phase pattern onto the atomic ensemble. In Fig. 3.7, we show the time traces simulated by solving the many-body master equation (ME) as solid red lines. The outcomes of adopting the coherent state approximation and the mixed coherent state approximation are shown as orange dashed and blue dotted lines, respectively. As a reference, we also show the dynamics of an ensemble of independent atoms as a solid black line.

In Fig. 3.7(a)-(d), we choose pulse areas of $A = \{0.1\pi, 0.5\pi, 0.8\pi, \pi\}$, respectively. In (a), the pulse area of $A = 0.1\pi$ corresponds to an excited state probability of only $\sin^2(0.1\pi/2) \approx 0.02$ and all three models predict the same dynamics for the power, P_f . Notably, the decay dynamics is quite different from the case of independent emission. In particular, the decay constant is collectively enhanced, i.e., superradiant. For $A = 0.5\pi$ in (b), each atom is prepared in an equal superposition of ground and excited state, and, again, all three models predict almost the same dynamics. We now start to see a deviation from an exponential decay. In (c), we increase the excited state probability from 0.5 to 0.9 and start to observe differences in the model predictions. The CSA prediction deviates substantially already for short times and does not fully capture the initial increase in power predicted by the ME and MCSA approach. In (d), we plot the case of full inversion,

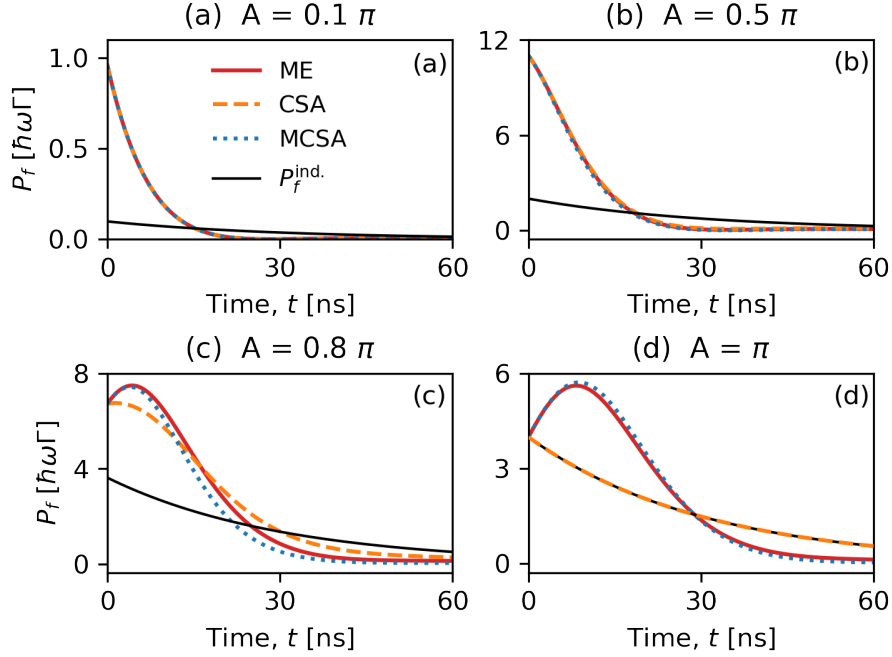


Figure 3.7: Simulated power emitted into the forward direction by $N = 10$ chirally coupled atoms with $\beta_f = 0.4$ for different theoretical models and different initial states, $|\psi_0\rangle$. ME: Solution of the many-body master equation. CSA: Simulation assuming the coherent state approximation. MCSA: Simulation assuming the mixed coherent state approximation. The pulse areas are $A = \{0.1\pi, 0.5\pi, 0.8\pi, \pi\}$ in (a)-(d), respectively. The exponentially decaying power for an ensemble of independently emitting atoms is shown as solid black lines for reference.

i.e., $A = \pi$. As expected, the CSA approach now completely fails and its prediction coincides with the dynamics of an ensemble of independently emitting atoms (see solid black line). However, the MCSA model prediction is still in close agreement with the ME solution. In particular, the superradiant burst dynamics, i.e., an initial increase of the emitted power, is well captured. We numerically checked that the threshold atom number predicted by the MCSA is exactly the same as the analytical expression in Eq. (3.15).

For later times, t , the dynamics predicted by the MCSA deviates much more from the many-body master equations. In Fig. 3.8, we plot the MCSA and ME prediction for P_f for 10 initially inverted ($A = \pi$) atoms, with a unidirectional coupling of $\beta_f = 0.4$. Note that this is the same setting as in Fig. 3.7(d). Here, we plot the dynamics on a semi-log scale to highlight that the differences between MCSA and ME grow with time. For $t > 30$ ns, the ME predicts that the decay rate of P_f oscillates between values that are slightly faster and slower than Γ , indicating that the ensemble evolves through several subradiant states. This dynamics is not captured by the MCSA prediction, which converges to an

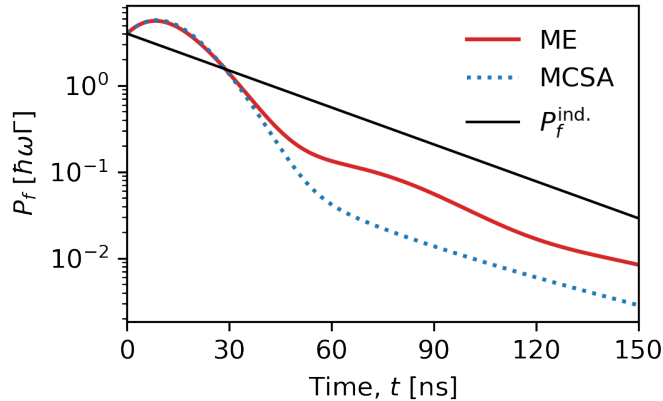


Figure 3.8: Decay dynamics of P_f for 10 initially inverted atoms and a unidirectional coupling of $\beta_f = 0.4$. Note the semi-log scale. We show the ME and MCSA predictions as solid red and blue dotted lines, respectively. As a reference, we also plot P_f for an independently emitting ensemble as a solid black line.

exponential decay for large t . In order to improve on the predictions for later times, one could simulate the system using the so-called cumulant expansion [105, 106]. This approach is based on neglecting atom-atom correlations beyond a certain order m , such that the computational complexity of the calculations is reduced from exponential to N^m . For atomic arrays in free space, it was recently shown that the predictions by a cumulant expansion to third order closely match the ME predictions for 10 atoms, even for later times [107]. However, simulating the dynamics of ensembles consisting of thousands of atoms is still very challenging for a computational complexity that scales as N^3 . Since we are mainly interested in the early superradiant dynamics and the MCSA model's computational complexity scales only linearly with N , we will not further discuss the cumulant expansion in this thesis.

3.5.2 Benchmarking using the mixed coherent state approximation

While we are not able to benchmark our approximative models against the ME for larger atom numbers, the close match between MCSA and ME for 10 atoms motivates the following analysis, in which we compare all other models to the MCSA. We now choose a coupling strength that is realistic for our experiment, $\beta_f = 0.01$, and compute the predicted output power, P_f , for the different models explained above. We now also simulate the pulsed excitation with a pulse width of $T_{\text{pulse}} = 4$ ns and perform a 2D-scan of the pulse area, A , and the number of atoms, N . In order to quantify how close the different model

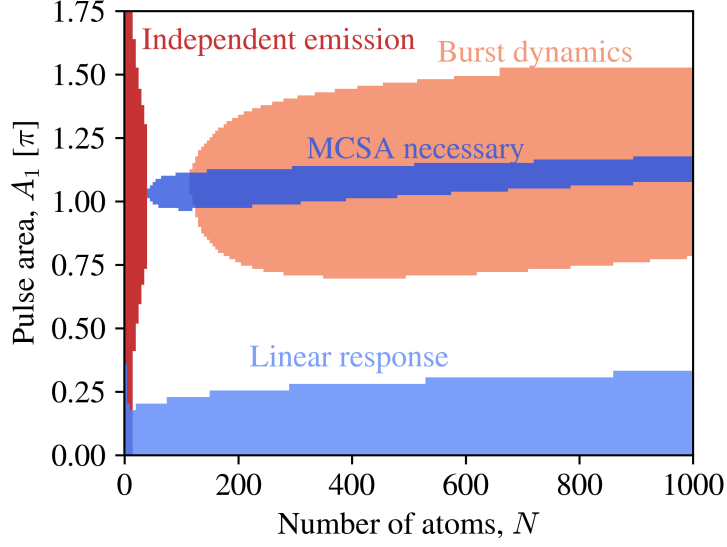


Figure 3.9: Different regimes of collective dynamics. Here, we assume a 4 ns-long, nanofiber-guided excitation pulse, $\beta_f = 0.01$, and $\beta_b = 0$. We compare the predictions of the different theoretical models for the power emitted into the forward direction to the MCSA prediction.

predictions are to the MCSA prediction, we introduce the relative deviation $\delta(A)$:

$$\delta(A) = \frac{\int_0^\infty dt |P_f^A(t) - P_f^{\text{MCSA}}(t)|}{\int_0^\infty dt P_f^{\text{MCSA}}(t)}. \quad (3.31)$$

Here, $P_f^A(t)$ denotes the prediction for $P_f(t)$ using model A. We then define four different regimes, which we plot as colored areas in Fig. 3.9. They are defined as follows:

- Independent emission (dark red): $\delta(\text{Independent emission}) < 0.1$,
- Linear response (light blue): $\delta(\text{Linear response}) < 0.1$,
- Burst dynamics (light red): The MCSA prediction for the peak power emitted into the forward direction occurs at a time $t > 0$ ns. ,
- MCSA necessary (dark blue): $\delta(\text{CSA}) > 0.1$,
- White regions: $\delta(\text{CSA}) < 0.1$, but $\delta(\text{Linear response}) > 0.1$ and $\delta(\text{Independent emission}) > 0.1$, and no burst dynamics occurs.

The probability that a scattered photon is reabsorbed by another atom is small in an optically thin medium. Then, the interatomic interaction can practically be neglected, and

the decay into the waveguide is that of independently emitting atoms. Indeed, independent emission correctly describes the dynamics of ensembles comprising less than about 40 atoms, which corresponds to an optical depth of about 1.6, see Figure 3.9. On the other hand, linear response theory correctly describes the dynamics of even larger ensembles with up to 1000 atoms, as long as the pulse area is smaller than about 0.25π , which corresponds to an excited state probability of about 0.15. The breakdown of linear response theory for larger pulse areas is expected since one assumes a negligible excited state probability in linear response theory.

Only for almost fully inverted ensembles ($A_1 \approx \pi$), MCSA and CSA differ by more than 10%. Notably, this regime (labeled “MCSA necessary” in Fig. 3.9) occurs over a quite narrow range of pulse areas, A_1 , which gets even narrower for a larger number of atoms. However, burst dynamics occurs over a much wider range of pulse areas. This means that even the CSA correctly predicts burst dynamics, albeit for ensembles that are not fully inverted. The difference between these two regimes will be further analyzed in section 5.5, where we present an experiment that allows us to directly identify the regimes of superradiant burst dynamics and the underlying physical mechanisms. The characteristic threshold atom number beyond which the superradiant burst appears is predicted to be 114 atoms for our parameters, see Fig. 3.9. Finally, there is a small parameter space, in which MCSA is necessary, but no burst dynamics occurs. This can be understood from the fact that the CSA predicts independent emission for fully inverted ensembles, regardless of the number of atoms. Therefore, as soon as the atoms do not emit independently, CSA breaks down for pulse areas of about π , despite the fact that the number of atoms is still below the characteristic threshold for the superradiant burst. We note that, while we assumed a perfectly homogeneous coupling strength in the above analysis, the coupling strengths feature some inhomogeneous broadening in the actual experiment. This shifts the threshold for the superradiance burst to larger atom numbers and narrows the regime, in which MCSA and CSA differ even more.

3.6 Emission into the backward direction

Although we assume unidirectional atom-waveguide coupling in the CSA and MCSA model, in the actual experiment, the coupling to the backward-propagating mode, β_b , is not zero. However, we excite the atoms via the forward-propagating mode, and the collective dynamics is dominated by forward-propagating photons. We can thus assume that any phase pattern that forms along the atomic ensemble is determined by the propagation phase of the forward-propagating mode. Since the spacing between the atoms is incommensurate with the in-fiber transition wavelength, and the optical lattice in our

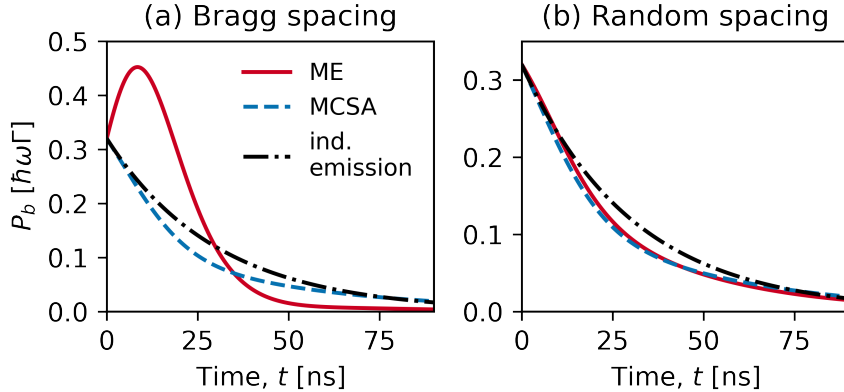


Figure 3.10: Dynamics of the power emitted into the backward-propagating mode, P_b . We again assume unidirectional coupling with $\beta_f = 0.4$. We simulate the dynamics of 10 initially fully inverted atoms for different settings. (a) The atoms are spaced by half the in-fiber wavelength, λ_f . (b) The atoms are randomly spaced. For random spacing, incoherent summation of the populations is sufficient to model P_b . We assume an atom-waveguide coupling strength of $\beta = \beta_f + \beta_b = 0.4$. We assume a directional coupling as in our experiment, i.e., $D = 0.84$. We compare the ME prediction with the MCSA prediction, see solid red and blue dashed lines, respectively. As a reference, we show the case of independently emitting atoms as a black dashed line.

experiment is randomly filled, we can treat the emission into the backward direction as if it was incoherent. Therefore, we calculate the power emitted into the backward direction, P_b , by incoherently summing up the time-dependent emission rates of the individual atoms:

$$P_b = \beta_b \Gamma \sum_{i=1}^N \rho_i^{ee} \quad (3.32)$$

To test the validity of this assumption, we again solve the many-body master equation for 10 atoms. This time, we set the ratio between forward and backward coupling to $\beta_f/\beta_b \approx 12$, as in the experiment. The total atom-waveguide coupling, is chosen as in Fig. 3.7, i.e., $\beta = \beta_f + \beta_b = 0.4$. In Fig. 3.10, we show the calculation of P_b using the ME (solid red line), as well as the incoherent sum of the atomic populations predicted by the MCSA, i.e., Eq. (3.32) (dashed blue line). In (a), we assume the Bragg configuration. In (b), we average over 20 randomly chosen configurations of atomic positions to simulate the probabilistic loading of trapping sites in our experiment. While there is a difference between the exact calculation of P_b and incoherent summation for an ensemble in Bragg configuration, the two results almost coincide for the irregular spacing that occurs in our

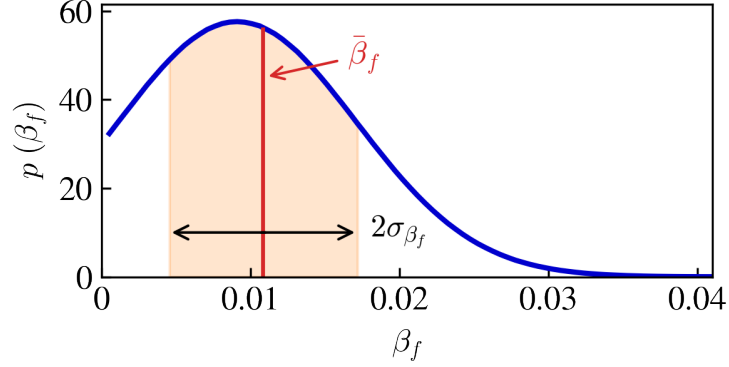


Figure 3.11: Approximative probability distribution for the coupling strength, β_f . We assume a Gaussian distribution that is truncated at $\beta_f = 0$ and $\beta_f = 1$. The mean and standard deviation of the truncated Gaussian are indicated by the red vertical line and the black double arrow, respectively.

experiment. This comparison justifies our approximative calculation of P_b . Note that while the dynamics in the backward direction does not feature a superradiant burst for random spacing, it still differs from independent emission, see black dash-dotted line for reference.

3.7 Fluctuations of the coupling strength

As discussed in section 2.8, the coupling strength of the atoms to the nanofiber-guided mode depends on their radial distances from the fiber surface as well as their azimuthal positions. Due to the thermal motion of the atoms in their trapping potential, the coupling strengths fluctuate. In order to model this effect, we assume a probability distribution of β_f values, $p(\beta_f)$. In the CSA and MCSA models, we then draw a random β_f from $p(\beta_f)$ for each atom and propagate the field through the ensemble, as described in section 3.3 and 3.4. We assume that the coupling strength for each atom stays constant during a single excitation- and emission process. This is justified due to the large difference between the timescales of the decay dynamics (about 30 ns) and the motional period of the atoms in their trapping potential (about 10 μ s). We draw 100 such random β_f -configurations from $p(\beta_f)$, and average the resulting time traces of P_f , ρ_{eg}^k , and ρ_{ee}^k for each atom, k .

Most of the experiments described in this thesis are not carried out in thermal equilibrium, and it is challenging to measure or simulate the actual distribution of β_f values during the probing sequence. Instead, we model temperature-induced fluctuations of the coupling strength by approximating the probability distribution of β_f values as a Gaussian see

Fig. 3.11. Since $\beta_f \in [0, 1]$, we truncate the Gaussian distribution both at $\beta_f = 0$ and $\beta_f = 1$ to avoid unphysical values of the coupling strength. We then use the mean of the distribution, $\bar{\beta}_f$, and the standard deviation, σ_{β_f} , as fit parameters to match our theoretical predictions to the experimental data. For the data shown in chapter 4, we find the best agreement of model and data for a mean and standard deviation of the truncated distribution of $\bar{\beta}_f = 0.0108$ and $\sigma_{\beta_f} = 0.0065$, respectively. For the data shown in chapter 5, we find the best fit for slightly different parameters, i.e., $\bar{\beta}_f = 0.0112$ and $\sigma_{\beta_f} = 0.0065$. Notably, these two parameters are the only free parameters in the theoretical modeling of the data presented in chapters 4 and 5.

4 Coherent excitation and coherent forward scattering

This chapter is based on Ref. [108]:

C. Liedl, S. Pucher, F. Tebbenjohanns, P. Schneeweiss, and A. Rauschenbeutel. [Collective Radiation of a Cascaded Quantum System: From Timed Dicke States to Inverted Ensembles](#). *Phys. Rev. Lett.*, 130(16):163602, 2023.

In this thesis, we are interested in the collective radiative dynamics of an ensemble of nanofiber-coupled atoms. In particular, we want to explore how the dynamics changes as a function of the initial excitation of the ensemble, from the weak excitation regime to full inversion. In this chapter, we first describe and analyze the coherent excitation of an atomic ensemble using fiber-guided laser pulses that are much shorter than the excited state lifetime. Then, we explore the decay dynamics of the power emitted into the nanofiber-guided modes following the excitation pulse. In particular, we will focus on the role of coherent forward scattering.

4.1 Coherent excitation

Ideally, we would like to be able to coherently excite each atom close to the state $|\psi_0\rangle$, see Eq. (3.30), which features an induced dipole moment, d_0 , and an excited state probability, p_{exc} ,

$$|\psi_0\rangle = \cos\left(\frac{A}{2}\right) |g\rangle - i \sin\left(\frac{A}{2}\right) |e\rangle, \quad (4.1)$$

$$d_0 = \langle\psi_0|(\hat{\sigma} + \hat{\sigma}^\dagger)|\psi_0\rangle = -2i \sin\left(\frac{A}{2}\right) \cos\left(\frac{A}{2}\right), \quad (4.2)$$

$$p_{\text{exc}} = \langle\psi_0|\hat{\sigma}^\dagger\hat{\sigma}|\psi_0\rangle = \sin^2\left(\frac{A}{2}\right). \quad (4.3)$$

Here, we have expressed d_0 in units of the transition dipole matrix element. Note that d_0 is purely imaginary only for resonant excitation. We plot both the imaginary part of d_0 and p_{exc} as a function of the pulse area, A , in Fig. 4.1, see blue dashed and red solid lines,

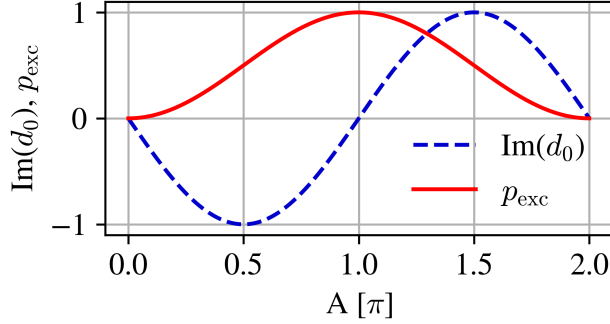


Figure 4.1: Dependence of the imaginary part of the induced dipole moment, d_0 , and the excited state probability, p_{exc} , on the pulse area, A . We assume coherent, resonant excitation with an idealized Rabi pulse, which prepares the atoms in state $|\psi_0\rangle$, see Eq. (4.1).

respectively. The excited state probability reaches a maximum of $p_{\text{exc}} = 1$ for a pulse area of π , i.e., the atom is fully inverted. For $A \in (0, \pi)$, d_0 is negative and imaginary, i.e., the induced dipole moment features a 90° -phase lag with respect to the excitation laser, as for a classical Lorentz oscillator [109]. Importantly, $\text{Im}(d_0)$ vanishes for maximal p_{exc} . As A is further increased, $\text{Im}(d_0)$ increases again, albeit with the opposite sign.

The most straightforward way to prepare the atoms in state $|\psi_0\rangle$ is to expose them to a short laser pulse that drives coherent Rabi oscillations, where the frequency is given by the Rabi frequency, Ω . According to the area theorem, the corresponding pulse area is then given by $A = \int dt \Omega(t)$ [110]. Since we use rectangular pulses, A is the product between Ω and the pulse duration, T_{pulse} . The Rabi frequency is typically calculated as the scalar product of the atomic transition dipole moment, \vec{d} , and the electric field of the optical drive, \vec{E} ,

$$\Omega = \frac{\vec{d} \cdot \vec{E}}{\hbar} \quad (4.4)$$

However, we excite the atoms using a nanofiber-guided laser field. Since the evanescent field varies substantially over the trapping volume, the temperature of the atoms in their trap, and thus, their distribution of positions has to be precisely known in order to calculate the Rabi frequency. Instead, we will express the Rabi frequency in terms of the coupling strength, β_f , which can be determined experimentally, see section 2.8.

$$\Omega = \sqrt{\frac{4\beta_f \Gamma P_{\text{in}}}{\hbar \omega}}, \quad (4.5)$$

where P_{in} is the initial power of the excitation laser, see Appendix A.2 for a derivation.

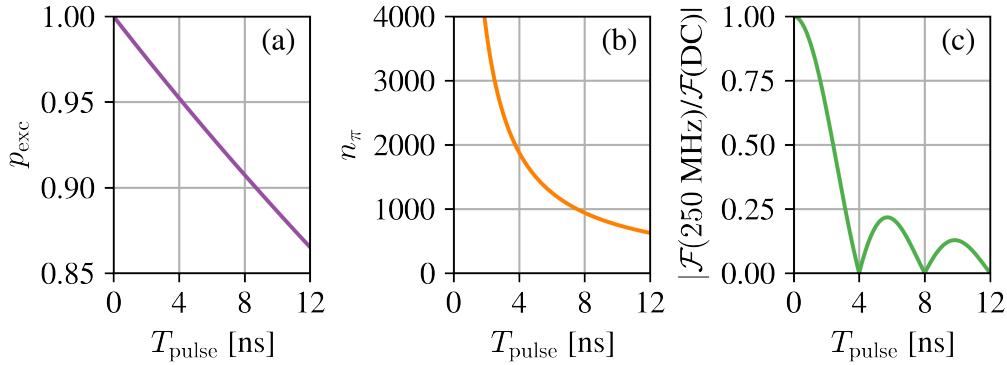


Figure 4.2: Different constraints for the coherent excitation with a π -pulse as a function of the pulse duration, T_{pulse} . (a) Excited state probability after a π -pulse with duration T_{pulse} . (b) Number of photons in the π -pulse. (c) Absolute value of the spectral component at $2\pi \times 250$ MHz, normalized by the DC component.

4.1.1 Choice of the pulse duration

In order to fully invert the ensemble, the pulse area, A , has to equal to π for each atom. In addition, there are other constraints that have to be met. In Fig. 4.2, we show the scaling of the following three constraints with the pulse duration, T_{pulse} :

1. Spontaneous emission: The pulse duration has to be much shorter than the excited state lifetime of about 30.5 ns, since spontaneous emission inevitably leads to decoherence. For a single atom and resonant excitation, one can analytically compute the excited state probability, p_{exc} , after a π -pulse with duration T_{pulse} , which is shown in Fig. 4.2(a). See appendix A.3.2 for a derivation.
2. Number of photons: For an ideal π -pulse, each atom absorbs exactly 1 photon from the laser. Therefore, the Rabi frequency decreases along the ensemble due to absorption of the excitation pulse. In order to invert the entire ensemble, the number of photons in the π -pulse has to be at least larger than the number of atoms. Using Eq. (4.5), one can calculate the number of photons for a given pulse duration, T_{pulse} , and a pulse area, A ,

$$n(A) = \frac{A^2}{4\beta_f \Gamma T_{\text{pulse}}}. \quad (4.6)$$

The number of photons in a $A = \pi$ -pulse as a function of T_{pulse} is shown in Fig. 4.2(b).

3. Excitation of other hyperfine levels: The spectrum of a rectangular pulse centered at $t = 0$ ns is given by its Fourier transform, $\mathcal{F}(\omega) \sim \sin(\omega T_{\text{pulse}}/2)/(2\omega)$. For a short enough pulse, the pulse features a substantial spectral component that is resonant with the other hyperfine levels of the excited state manifold. In Fig. 4.2(c), we

show the magnitude of the spectral component at 250 MHz, which is the detuning of the adjacent hyperfine level, $|6P_{3/2}, F = 4\rangle$, from the target hyperfine level, $|6P_{3/2}, F = 5\rangle$. The excitation of other hyperfine levels can result in quantum beats of the emitted power, which may obscure the observation of the targeted collective dynamics.

While, in order to meet the first two constraints, the pulse duration should be as short as possible, the third constraint is detrimental for very short pulses. For $T_{\text{pulse}} = 4$ ns, the spectral component at 250 MHz is zero and the decay probability is only about 7 %. Moreover, there are about 1900 photons in a π -pulse, which is substantially larger than the at most 1000 trapped atoms in our experiment. A pulse duration of $T_{\text{pulse}} = 4$ ns is, therefore, a natural sweet spot with respect to the three constraints listed above. However, we only understood the third constraint after performing the measurements presented in this section, such that we chose a pulse duration of 5 ns. The pulse duration is then changed to 4 ns for the experiments presented in chapter 5.

4.1.2 Absorption of the excitation pulse

As explained above, the number of photons in a π -pulse should be larger than the number of atoms. In this section, we will analyze this constraint more carefully to understand the role of absorption of the excitation pulse in the coherent excitation of an ensemble of atoms. To quantify this effect, we use a very simple model of pulse absorption. In particular, this model neglects all other decoherence and dephasing effects, such that it will allow us to analyze how the absorption of the probe laser along the ensemble limits the maximally achievable excited state probability.

For an excitation pulse much shorter than the excited state lifetime, the k th atom absorbs, on average, an energy that corresponds to that of $p_{\text{exc}}^k \approx \sin(A_k/2)^2$ photons from the excitation pulse. Therefore, the number of photons in the excitation pulse that impinges on atom $k + 1$ is given by

$$n(A_{k+1}) = n(A_k) - p_{\text{exc}}^k. \quad (4.7)$$

For the first atom, we can directly compute the pulse area, A_1 , and the corresponding number of photons in the excitation pulse, $n(A_1)$, from the input power of the excitation laser field. Then, we calculate the pulse area seen by each atom by iterative use of the following expression,

$$A_{k+1} = \sqrt{A_k^2 - 4\beta_f \Gamma T_{\text{pulse}} p_{\text{exc}}^k}, \quad (4.8)$$

where we have inserted the expression for $n(A)$, i.e., Eq. (4.6), into both sides of Eq. (4.7). Due to absorption of the excitation pulse, the pulse area seen by the atoms thus decreases

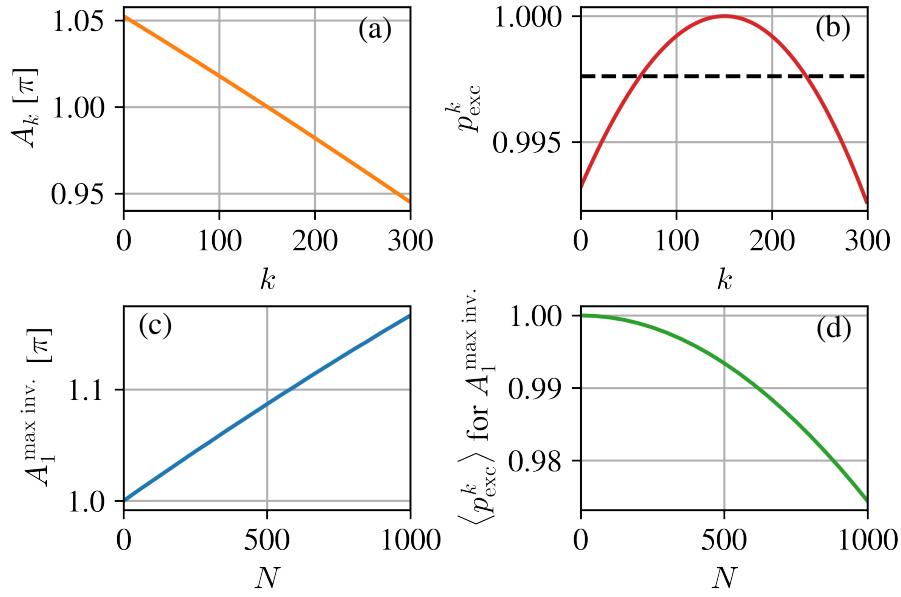


Figure 4.3: Absorption of the excitation pulse, for a pulse duration of $T_{\text{pulse}} = 5$ ns and $\beta_f = 0.0108$. (a) Decrease of the pulse area A_k along the ensemble due to absorption of the excitation pulse. Here, we chose a pulse area of $A_1 = 1.053\pi$, such that the average pulse area for 300 atoms is equal to $\langle A_k \rangle = \pi$. (b) Excited state probability along the ensemble, corresponding to the pulse areas shown in (a). The average excited state probability for the 300 atoms is 0.997, see black dashed line. (c) Pulse area, A_1 , that has to be set for the first atom in order to achieve an average pulse area of $\langle A_k \rangle = \pi$, as a function of the number of atoms in the ensemble, N . (d) Maximally achievable average excited state probability due to absorption of the excitation pulse as a function of N . Note that, in our simple model of pulse absorption, we neglect all decoherence and dephasing mechanisms.

along the atomic ensemble.

In Fig. 4.3(a), we show the decrease of A_k for 300 atoms. Here, we have chosen a pulse area of $A_1 = 1.053\pi$ for the first atom, such that the pulse area averaged over the whole ensemble, $\langle A_k \rangle$, is equal to π . In (b), we plot the excited state probability, p_{exc}^k , for each atom, assuming the pulse areas shown in (a). The black dashed line indicates the average excited state probability, $\langle p_{\text{exc}}^k \rangle = 0.997$, i.e., almost unity. However, the effect of pulse absorption introduces a systematic bias: The first atom will always see a slightly larger pulse area than the last atom. This order has a small but systematic effect on the collective decay dynamics following the excitation pulse, see section 5.4. While, in this section, we have only presented a simplified model of pulse absorption, both the CSA and MCSA models capture the full dynamics during the excitation pulse, such that all

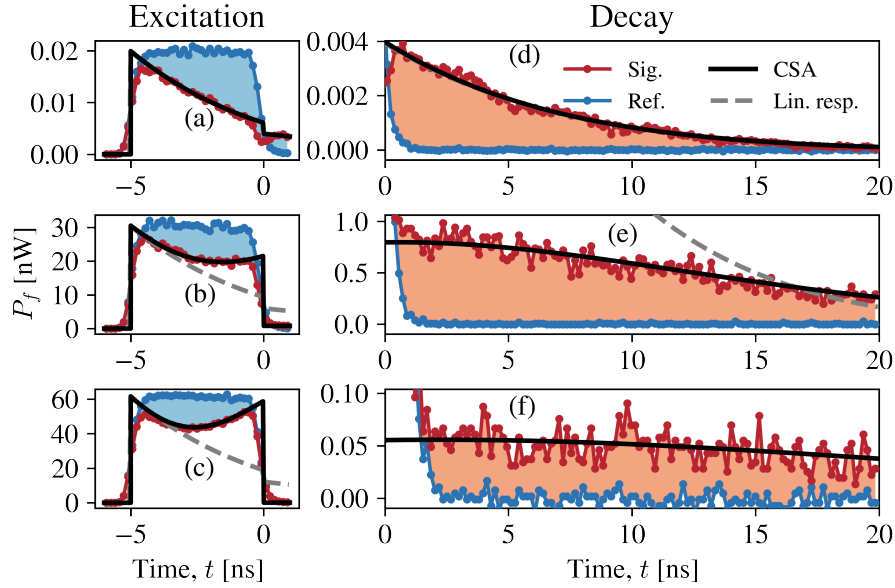


Figure 4.4: Collective excitation and decay of about 300 nanofiber-trapped atoms, for different excitation powers, P_{in} . The excitation dynamics is displayed in (a)-(c), for pulse areas of $A_1 = 0.02\pi, 0.7\pi,$ and π , respectively. The corresponding decay dynamics after switching off the excitation pulse at $t = 0$ ns is shown in (d)-(f). The measured signals are displayed as red dots, while the blue dots show reference measurements without atoms. The corresponding CSA and linear response predictions are shown as black solid and gray dashed lines, respectively.

propagation and absorption effects are taken into account.

Finally, in (c), we plot the pulse area, A_1 , that has to be set for the first atom, such that the pulse area averaged over an ensemble of N atoms is equal to π . In the following, we will denote the pulse area which maximally inverts the ensemble as $A_1^{\text{max inv.}}$. In panel (b), we plot the corresponding maximally achievable excited state probability. In our experiment, we can trap up to about 1000 atoms, such that, for a pulse duration of 5 ns, the absorption of the excitation pulse does not substantially limit the maximally achievable excited state probability. For even larger ensembles, one might have to either reduce the pulse duration or use a different excitation method.

4.1.3 Dynamics of the transmitted excitation pulses

In Fig. 4.4, we show time traces of the power exiting the fiber in the forward direction, P_f , for different excitation powers, P_{in} , and about 300 trapped atoms. Per experimental sequence, we launch 400 optical pulses with a pulse duration of $T_{\text{pulse}} = 5$ ns into the nanofiber-guided mode in order to improve the photon counting statistics. The repetition

rate of the optical pulses is 5 kHz, i.e., the probing sequence takes 80 ms in total. We perform continuous degenerate Raman cooling (DRC) with a free-space laser beam that is near-resonant with the D1 transition, such that, at most, 15 % of the atoms are lost from the trap during the probing sequence. We note that the scattering rate of the DRC laser field of about 10 kHz is three orders of magnitude smaller than the collective decay rate of the atomic ensemble. Therefore, we can assume that DRC does not substantially alter the observed collective dynamics. Each time trace shown in the following is obtained by averaging over the 400 probing pulses in each sequence. Moreover, we average over hundreds of experimental sequences to obtain sufficient counting statistics.

The excitation dynamics is shown in (a)-(c) in red, a reference measurement without atoms is shown in blue. In (d)-(f), we show the corresponding decay dynamics after the pulse is switched off at time $t = 0$ ns. Note that the data for the excitation and decay dynamics are taken from the same time traces and are simply displayed in two separate plots due to the widely different y -scales. The corresponding CSA and linear response predictions are shown as solid black and gray dashed lines, respectively, where we have assumed a truncated Gaussian distribution of coupling strengths, β_f , see section 3.7. In (a), the excitation power is about 20 pW, which corresponds to a pulse area of $A_1 \approx 0.02\pi$, i.e., much smaller than π . Consequently, the excited state probability is negligible, and the atomic response is well described by linear response theory. We observe a steep decrease of the transmitted power as the ensemble absorbs the excitation pulse. Subsequently, the ensemble emits the absorbed energy into the waveguide with a decay constant of 6.1(1) ns, i.e., much faster than the natural lifetime of 30.5 ns, see panel (d). This enhanced emission occurs due to the constructive interference of the atomic dipoles into the forward direction and has been experimentally observed, e.g., in Refs. [45, 46]. In (b) and (c), we increase the excitation power by about three orders of magnitude to 30 nW and 60 nW, respectively. The pulse areas seen by the first atom are 0.7π in (b) and π in (c), such that the non-linear response of the systems becomes apparent, i.e., each two-level atom can absorb at most one photon at a time. In particular, for the π -pulse in (c), the power increases again after an initial decrease and finally reaches the level of the input power at $t = 0$ ns. This indicates that the ensemble is fully saturated and can not absorb any more, as expected for an inverted ensemble. The fluorescent decay dynamics in panels (e) and (f) is non-exponential and deviates strongly from the predictions of linear response theory. Still, the data is in excellent agreement with the CSA predictions. Surprisingly, the maximum power emitted into the forward-propagating mode is about 20 times larger in (e) than in (f), despite the fact that more energy is stored in the ensemble in (f).

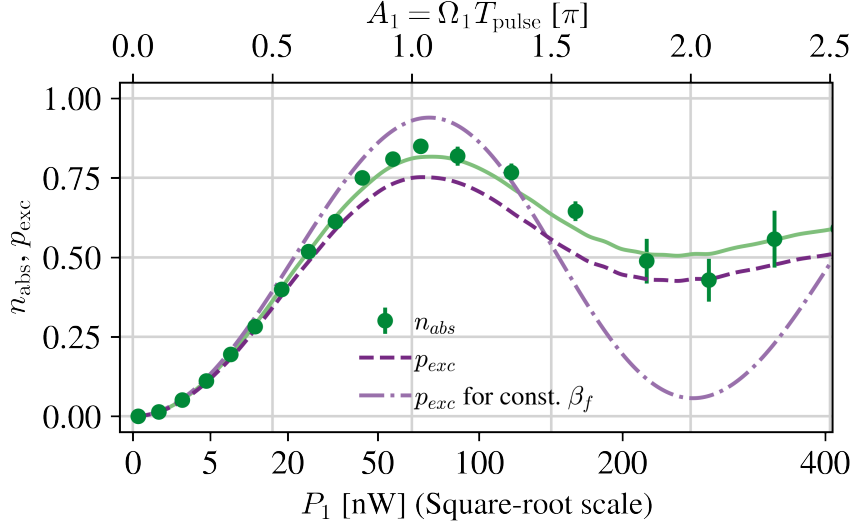


Figure 4.5: Number of photons absorbed per atom as a function of excitation power, P_{in} , and pulse area seen by the first atom, A_1 , (green dots). The corresponding CSA prediction is shown as the green solid line. The CSA predictions for the average excited state probability with and without taking into account fluctuations of β_f are shown as the purple dashed and dash-dotted lines, respectively.

4.1.4 Measurement of the excited state probability

In order to better understand the excitation dynamics, we will now analyze the time traces more quantitatively. The blue-shaded areas in Fig. 4.4(a)–(c) are equal to the energies that the atoms absorb from the excitation pulses. By dividing this energy by the number of atoms, N , and the photon energy, $\hbar\omega$, we can thus extract the number of photons absorbed per atom, n_{abs} .

$$n_{\text{abs}} = \frac{1}{N\hbar\omega} \int_{-T_{\text{pulse}}}^0 dt (P_f^{\text{ref}} - P_f^{\text{sig}}), \quad (4.9)$$

which we plot as green dots in Fig. 4.5 for different excitation powers, P_{in} , and corresponding pulse areas, A_1 . The corresponding CSA model prediction is shown as a green solid line. In addition, we plot the model prediction for the average excited state probability at $t = 0$, p_{exc} , as a purple dashed line. We observe that the ensemble performs damped Rabi oscillations, where n_{abs} and p_{exc} reach maximum values of $0.85(1)$ and $0.76(1)$, respectively. Note that this maximal inversion is reached for a pulse area of $A_1^{\text{max inv.}} = 1.04\pi$ due to absorption of the excitation pulse along the ensemble. This is in reasonable agreement

with our calculation in section 4.1.2, which gave $A_1^{\max \text{ inv.}} = 1.053\pi$. This shows that we are indeed able to coherently and substantially invert the entire ensemble of about 300 trapped atoms in this measurement. For a finite excitation pulse duration, p_{exc} is slightly smaller than n_{abs} since there is a non-zero probability that an excited atom decays spontaneously during the pulse, as discussed in section 4.1.1. For the 5 ns-long pulse used in this experiment, the probability of spontaneous emission during the pulse is about 0.08, which explains the difference between the two quantities $n_{\text{abs}} - p_{\text{exc}} = 0.09(2)$. In the following, we take n_{abs} as an estimate for p_{exc} .

We also show the CSA prediction for a homogeneous coupling strength, $\beta_f = \bar{\beta}_f$, as the purple dash-dotted line. There, p_{exc} reaches a maximum value of about 0.92=1-0.08, i.e., the value that is also expected for a single atom and a pulse duration of 5 ns, see Fig. 4.2(a). This confirms that the absorption of the pulse along the ensemble does not substantially affect the state preparation. Instead, thermal fluctuations of β_f that result in an inhomogeneous spread of Rabi frequencies are the limiting factor for the maximally achievable excited state probability.

While the excitation with resonant Rabi pulses is a conceptually and technically simple way to excite an ensemble of atoms, there are other methods that are more robust against inhomogeneous coupling. In particular, excitation using a composite sequence of picosecond pulses has recently been demonstrated for a few thermal atoms trespassing an optical nanofiber [111–113]. Alternatively, one could employ adiabatic protocols such as rapid adiabatic passage [114] or stark-chirped rapid adiabatic passage [115]. However, all these protocols pose new experimental challenges. Importantly, despite the imperfect state preparation due to the inhomogeneous atom-waveguide coupling strength, the experimentally observed collective dynamics is qualitatively very similar to the predicted dynamics for a constant coupling strength, as we will see in the following.

4.2 Coherent forward scattering

We now turn to the dynamics that occurs once the excitation pulse is switched off. In Figs. 4.4(d)-(f), the atoms emit a fraction of their stored energy into the forward-propagating nanofiber mode, where the magnitude of the fluorescence strongly depends on the power of the excitation pulse.

4.2.1 Scaling with the excitation power

Similar to our analysis in the previous section, we can extract the number of photons that are emitted, per atom, into the forward (backward) propagating guided modes, n_{em}^f

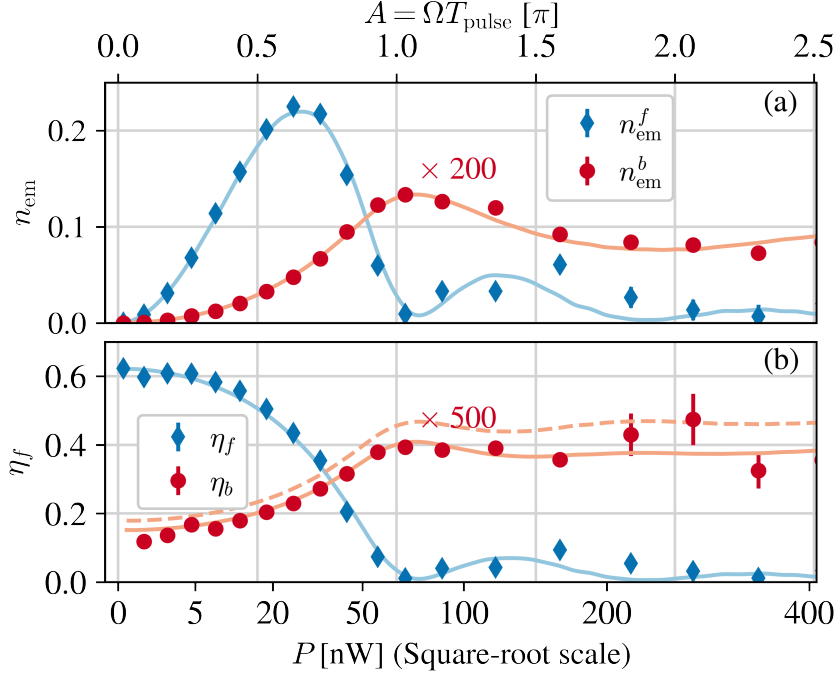


Figure 4.6: Integrated power of the forward-emitted light as a function of excitation power (and pulse area). (a) Number of photons per atom emitted into the forward (backward) propagating mode. (b) Fraction of stored energy emitted into the forward (backward) direction. The data for the forward and backward directions are shown in blue and red, respectively. The corresponding CSA predictions are depicted as solid blue and solid red lines.

(n_{em}^b) from the orange shaded areas in Fig. 4.4(d)-(f).

$$n_{\text{em}}^f = \frac{1}{N\hbar\omega} \int_0^\infty dt (P_f^{\text{sig}} - P_f^{\text{ref}}), \quad (4.10)$$

$$n_{\text{em}}^b = \frac{1}{N\hbar\omega} \int_0^\infty dt (P_b^{\text{sig}} - P_b^{\text{ref}}), \quad (4.11)$$

which we show together with the corresponding CSA prediction in Fig. 4.6(a) in blue and red, respectively. Note that the data for the backward direction is scaled by the factor indicated in red. We first turn to the number of photons per atom emitted into the forward direction, n_{em}^f . We observe a maximal value of 0.225(2), which means that about 70 photons are emitted into the forward-propagating nanofiber mode by only about 300 atoms. This has to be compared to the case of independent emission, where even a perfectly inverted ensemble would only scatter about $\beta_f N \approx 3$ photons into the forward

direction. Notably, the maximal n_{em}^f does not coincide with the maximal excited state probability, which occurs for a pulse area of $A_1^{\text{max inv.}} = 1.04\pi$, see Fig. 4.5.

To understand this behavior, we introduce two new quantities:

$$\eta_f = \frac{n_{\text{em}}^f}{n_{\text{abs}}}, \quad (4.12)$$

$$\eta_b = \frac{n_{\text{em}}^b}{n_{\text{abs}}}, \quad (4.13)$$

i.e., the fraction of stored energy that is emitted into the forward- and backward propagating modes, respectively. The number of photons emitted into the forward (backward) direction is then the product of the number of photons stored in the ensemble, n_{abs} and η_f (η_b), which can therefore be thought of as the collection efficiencies of the nanofiber-guided modes. For independently emitting atoms, we expect $\eta_f = \beta_f$ and $\eta_b = \beta_b$. Importantly, we note that the physical meaning of η_f is not that of a coupling strength. In particular, the optical drive by a fiber-guided light field is still determined by β_f , and not by η_f . The quantity η_f rather quantifies the collective enhancement of the emission into the forward-propagating mode.

We plot the measured values of η_f and η_b together with the CSA prediction in red and blue in Fig. 4.6(b), respectively. The enhancement in the forward direction is largest for vanishing input power and η_f reaches a maximum value of 0.62(1), which corresponds to a 60-fold enhancement of forward scattering compared to independently emitting atoms. In this regime, the data is also in good agreement with linear response theory, which predicts $\eta_f = 0.67$ for our experimental parameters. There, the system behaves like a phased array of classical antennas [116]. During the excitation, the propagation phase of the excitation laser field is imprinted onto the atoms, such that, in the single-excitation manifold, the ensemble is described by a so-called timed-Dicke state [32]:

$$|\text{TD}\rangle = \frac{1}{\sqrt{N}} \sum_{n=0}^N e^{ik_f z_n} |g_1, g_2, \dots, e_n, \dots, g_N\rangle, \quad (4.14)$$

which differs by the single-excitation Dicke state by the phase factor $e^{ik_f z_n}$, i.e., the propagation phase of the laser. This phase factor ensures that the light that is coherently scattered by the atoms interferes constructively into the forward direction, explaining the collectively enhanced collection efficiency, $\eta_f > \beta_f$. As we increase the excitation power, the excited state probability, p_{exc} , and, concomitantly, the probability of incoherent spontaneous emission, increases and eventually dominates the decay dynamics. For a

perfect π -pulse, the atoms are prepared in the fully inverted state

$$|\text{FI}\rangle = |e_1, e_2, \dots, e_N\rangle, \quad (4.15)$$

which features no phase relationship to the excitation laser anymore. As a result, we observe that η_f reaches a minimum value of $0.011(2) \approx \beta_f$ for a pulse area of $A_1^{\text{max inv.}} = 1.04\pi$, i.e., the collection efficiency of the forward-propagating mode is not collectively enhanced. We note that, for the measurements presented in this chapter, the system is prepared below the threshold for the onset of a superradiant burst. There, the light emitted by an ensemble of fully inverted atoms can show substantial coherence that also manifests as a collectively enhanced η_f , as we will see in chapter 5.

The peculiar dependence of n_{em}^f on the pulse area, see Fig. 4.6(a), can now be understood as a result of the complex interplay between coherent forward scattering (quantified by η_f) and the energy stored in the ensemble (quantified by n_{abs}). While the former is maximized for $A_1 \rightarrow 0$, the latter is maximized for $A_1 \rightarrow A_1^{\text{max inv.}} \approx \pi$, such that the best compromise for our parameters is met for $A_1 \approx 0.6\pi$. Notably, the data is in excellent agreement with the CSA predictions, which underlines the fact that the coherent part of the light field dominates the atomic dynamics in the regime studied in this section.

The emission into the backward direction shows a behavior that is very different from the forward direction. The number of photons per atom emitted into the backward direction peaks at a pulse area of about π , in agreement with the CSA predictions. There, the power emitted into the backward direction is assumed to be proportional to the incoherent sum of all atomic populations, see Eq. (3.32), which is why the maximal n_{em}^b coincides with the maximal p_{exc} . Therefore, one would naively assume that the collection efficiency in the backward direction is not collectively modified, and hence, $\eta_b = \beta_b$. However, as can be seen from both the experimental data and the CSA prediction, η_b does depend on A_1 and follows the opposite trend as η_f . Since the fields scattered by the atoms interfere constructively in the forward direction, there has to be destructive interference into the other modes due to energy conservation [117]. If one assumes that the only preferred mode is the forward direction, the fraction of energy emitted into the backward direction should approximately be given by

$$\eta_b = \frac{\beta_b}{1 - \beta_f}(1 - \eta_f), \quad (4.16)$$

which we show as the red dashed line in Fig. 4.6(b). Here, $1 - \eta_f$ is the fraction of energy that is scattered into all directions except the forward-propagating mode. A fraction of $\beta_b/(1 - \beta_f)$ of this energy should then be radiated into the backward direction. Indeed,

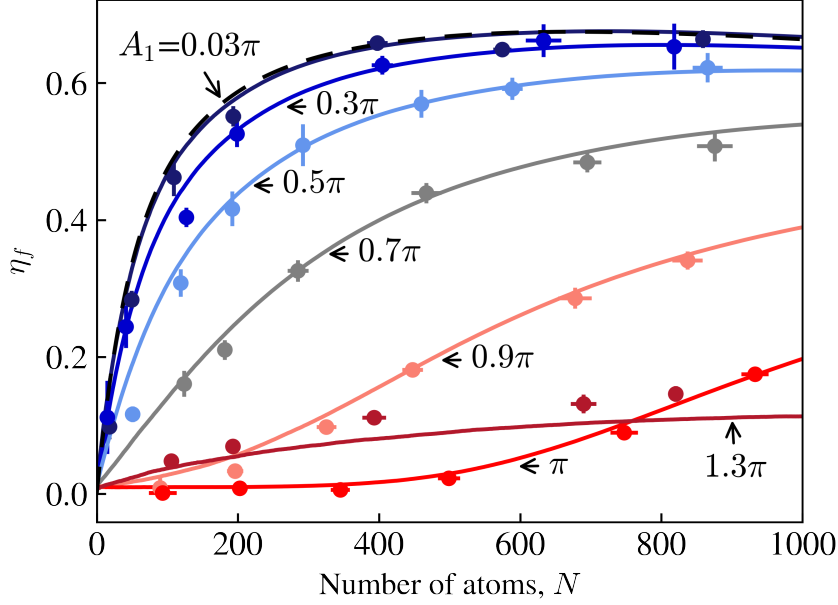


Figure 4.7: Fraction of stored energy emitted into the forward direction, η_f as a function of the number of atoms, N for different pulse areas, A_1 .

the calculation according to Eq. (4.16) qualitatively agrees with the full calculation using the CSA model, which is displayed as the red solid line. This further strengthens our assumption of incoherent backward emission.

4.2.2 Scaling with the number of atoms

To gain further insight into the underlying physics of coherent forward scattering beyond the weak excitation regime, we now investigate the dependence of η_f on the number of atoms, N . In Fig. 4.7, we show the dependence of η_f on N for different pulse areas, A_1 . The corresponding CSA predictions are shown as colored solid lines, and the linear response predictions are displayed as a black dashed line.

For the smallest pulse area, $A_1 = 0.03\pi$, η_f first increases linearly. In this weak excitation regime, the fields emitted by the atoms interfere constructively in the forward direction. Therefore, the power P_f scales quadratically, while the absorbed power only scales linearly. Since η_f is defined as the ratio between forward scattered energy and absorbed energy, the linear scaling that we observe experimentally is expected as long as coherent scattering dominates. As we increase the atom number further, η_f reaches a plateau, where up to 66(2)% of the energy is emitted into the forward direction, in accordance with the predictions of linear response theory. As we increase the pulse area to 0.3π and 0.5π ,

respectively, the initial slope of $\eta_f(N)$ decreases and the plateau value is slightly lower. For a pulse area of 0.9π , we observe a qualitatively different scaling with N . There, the initial increase of η_f is superlinear, which is indicative of a build-up of coherence along the atomic array. For a pulse area of π , η_f stays at a constant value of roughly $0.01 \approx \beta_f$ until N reaches about 400, from when on it increases superlinearly. Finally, for a pulse area of 1.3π , we observe a similar scaling as for the case of $A_1 = 0.7\pi$. This is because the average excited state probability should ideally be the same for pulse areas symmetric around π . We numerically checked that the lower slope and plateau value are primarily due to the larger thermal fluctuations of the absolute pulse area for larger A_1 .

One could interpret the superlinear scaling that we observe for pulse areas close to π as a signature of superradiant burst dynamics, i.e., a phase locking of the atomic dipoles during their decay. However, in this measurement, we chose a fixed excitation power, P_{in} , for each scan of the number of atoms, N . Due to absorption of the excitation pulse, the pulse area decreases with N . Since the induced dipole moment after a Rabi pulse, d_0 , is largest for a pulse area of $\pi/2$, d_0 increases with N for $A_1 \in (0.5\pi, \pi)$, see Fig. 4.1. Thus, it is quite difficult to distinguish whether the superlinear scaling is caused by absorption or by a collective phase locking of the atomic dipoles. Notably, the CSA model fully captures the behavior of η_f over the whole parameter space explored in this measurement, where we have scanned both the excitation power, P_{in} , and the number of atoms, N , over three orders of magnitude. The fact that the CSA is sufficient to explain our data is evidence that we have prepared the ensemble in a regime in which the coherent part of the light fields emitted by the atoms dominates the decay dynamics.

4.3 Intermediate summary and conclusion

We have demonstrated the experimental capability to coherently excite an ensemble of hundreds of nanofiber-trapped atoms using nanofiber-guided optical Rabi pulses. We inferred the excited state probability from the number of photons that the atoms absorb from the excitation pulse and achieved almost full inversion of the atomic ensemble. We explored the subsequent decay of the power emitted into the waveguide from weak excitation to full inversion. Importantly, we found that the fraction of energy scattered into the forward-propagating nanofiber mode can be strongly enhanced. This enhancement is known as coherent forward scattering and is well known in the regime of linear response [50]. Here, we showed that coherent forward scattering heavily influences the collective decay dynamics even close to full inversion. Specifically, the amount of enhanced forward emission can be understood as an interplay between coherent forward scattering and decoherence due to spontaneous emission, which increases with the excited state probability.

Consequently, the maximal waveguide-emitted energy occurs for a pulse area close to $\pi/2$. It has been theoretically shown that the directional photon emission close to a nanofiber leads to a lateral recoil force [118]. Using our method, this recoil force could be collectively enhanced [119]. Moreover, since we realized a cascaded quantum system, the fraction of energy emitted into the forward direction, η_f , is much larger for the last atom than for the first atom since the latter decays independently. Consequently, also the recoil is larger for the last atom than for the first atom, leading to a compression of the atomic ensemble in the absence of axial confinement. Studying these effects may be interesting in the context of optically driven self-organization of atomic ensembles close to a nanophotonic waveguide [120–122].

Moreover, a superradiant phase transition has recently been observed in a driven, pencil-shaped cloud of atoms close to the Dicke regime [123]. It would be an intriguing research direction to study the influence of directional coupling on these effects and explore similar dynamics in a wQED system.

5 Superradiant bursts

This chapter is based on Ref. [124]:

C. Liedl, F. Tebbenjohanns, C. Bach, S. Pucher, A. Rauschenbeutel, and P. Schneeweiss. [Observation of superradiant bursts in waveguide QED](#). *arXiv:2211.08940*, 2022.

The clapping of an audience after an artistic performance often synchronizes, despite the lack of any reference or leader. Still, crowds of thousands of people manage to spontaneously agree on a common rhythm within seconds. Such spontaneous synchronization was already observed by Huygens in the 17th century for mechanically coupled pendulum clocks [125]. More generally, spontaneous synchronization lies at the heart of a variety of natural phenomena, ranging from flocks of birds, to synchronized heart cells and flashing fireflies [126].

We have already learned that an ensemble of initially inverted atoms can emit a superradiant burst of light which is due to a build-up of coherence between the atomic dipoles, i.e., the dipoles synchronize over time. However, the fully inverted state has zero dipole moment and the phases of the individual atomic dipoles are initially not defined. Thus, superradiant bursts of an initially fully inverted ensemble can be regarded as a prime example of spontaneous synchronization in quantum optics.

In section 3.5, we described that our system is expected to exhibit superradiant burst dynamics when prepared close to or at full inversion. While we have already shown the capability to substantially invert the atomic ensemble in the previous chapter, we concluded that we did not reach the regime in which incoherent emission by the atoms dominates the collective decay dynamics, as it is the case for Dicke superradiant bursts of a fully inverted ensemble.

In this chapter, we report on the observation of superradiant burst dynamics for an ensemble of atoms that are unidirectionally coupled to the nanofiber mode. We then analyze the scaling of the peak-emitted power with the number of initially inverted atoms. We explore superradiant burst dynamics over a wide range of initial excitations and measure the coherence properties of the superradiant burst. This allows us to identify two regimes of burst dynamics in which the synchronization of the atomic dipoles is either spontaneous or seeded by the excitation laser. Finally, we briefly explore the subradiant

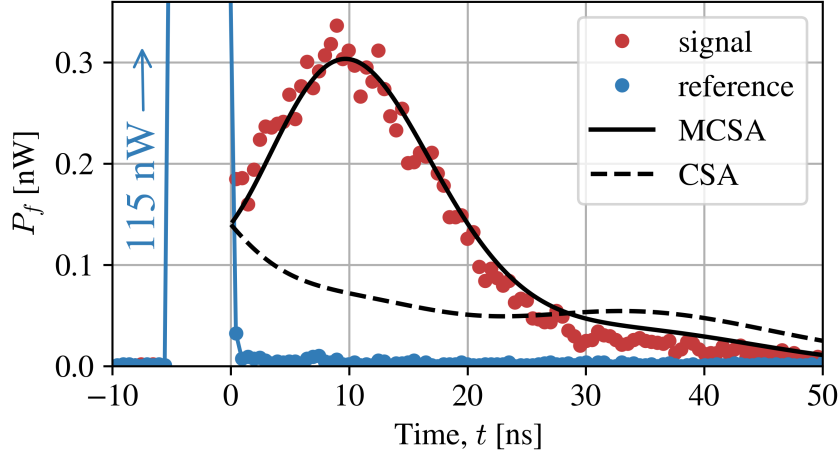


Figure 5.1: Dynamics of the power emitted into the forward-propagating mode, P_f . The signal with and without atoms is shown as red and blue dots, respectively. The ensemble of about 1000 atoms is maximally inverted after the excitation pulse, which switches off at time $t = 0$ ns. The subsequent decay dynamics shows a clear burst, characterized by an initial increase of the emitted power. The MCSA and CSA predictions are shown as a black solid and black dashed line, respectively.

dynamics following the initial superradiant decay.

5.1 Observation of superradiant burst dynamics

In order to reach the regime of superradiant burst dynamics, two technical changes with respect to the measurements in chapter 4 were decisive. First, we changed the pulse duration to 4 ns in order to minimize off-resonant excitation of the neighboring hyperfine levels of the excited state manifold, as explained in section 4.1.1. Second, we used the hybrid photodetector instead of the SPCM to measure the optical power that exits the nanofiber. This greatly reduced afterpulsing, which was detrimental to the observation of burst dynamics in our setting.

In Fig. 5.1, we show a time trace of the power emitted into the forward-propagating mode, P_f , as red dots. A reference measurement without atoms is shown as blue dots. We apply the same probing sequence used in chapter 4, i.e., we expose the atoms to 400 optical pulses per experimental sequence while performing continuous cooling. The time traces are then averaged over hundreds of experimental realizations.

The 4 ns-long excitation pulse with a power of 115 nW corresponds to a pulse area of

$A_1 = A_1^{\max \text{ inv.}} = 1.12 \pi$, such that the ensemble of about 1000 atoms is maximally inverted at time $t = 0$ ns. As the ensemble subsequently decays ($t > 0$ ns), we observe that the power first increases, reaches a maximal value of P_f^{\max} after a delay of $t_D \approx 9$ ns, and then decreases. This is in stark contrast to the exponential decay dynamics of an ensemble of independently emitting atoms, where the power decreases monotonously. The initial increase of the emitted power is the characteristic feature of a superradiant burst. Since the ensemble is not driven for $t > 0$ ns, the energy stored in the ensemble can only decrease. Yet, the power emitted by the ensemble features an initial increase. This observation provides evidence that the atomic dipoles indeed synchronize during their decay and acquire a common phase, which results in constructive interference of the emitted fields, as in the case of standard Dicke superradiance. We also show the model predictions of both the CSA and the MCSA models. We find an excellent agreement with the MCSA prediction, while the CSA model fails to describe our observations. This suggests that we have prepared the ensemble in a regime in which the atomic dynamics is predominantly driven by incoherently emitted light, which is not captured by the CSA. This regime of superradiance is sometimes called superfluorescence [127]. There, the synchronization of the atomic dipoles is not seeded by the excitation laser field but triggered by vacuum fluctuations. In the following sections, we will analyze different aspects of the superradiant burst to gain further insight into the physical mechanisms which govern the observed dynamics.

5.2 Scaling with the number of atoms

In the ideal case of Dicke superradiance, all atoms are located at the exact same position. Therefore, they all emit into a single optical mode. In this case, even two atoms synchronize during their decay and, consequently, a (small) burst occurs. In our case, however, most of the energy stored in the atomic ensemble is emitted into free space, i.e., into independent optical modes. However, only the emission into the forward-propagating mode contributes to the synchronization between the atoms. Therefore, a superradiant burst is only expected to occur above a certain threshold atom number, beyond which the synchronization dominates over the independent decay, as discussed in section 3.2.3.

In Fig. 5.2, we plot the measured time traces of P_f for various numbers of atoms, N , where we have normalized each time trace by its peak value, P_f^{\max} . Importantly, in order to maximally invert the ensemble, one has to slightly change the excitation power for each N . This is because, due to absorption of the excitation pulse, the average pulse area seen by the ensemble is smaller than the pulse area seen by the first atom, see section 4.1.2. To determine the power of the excitation pulse, P_1 , which maximally inverts an ensemble

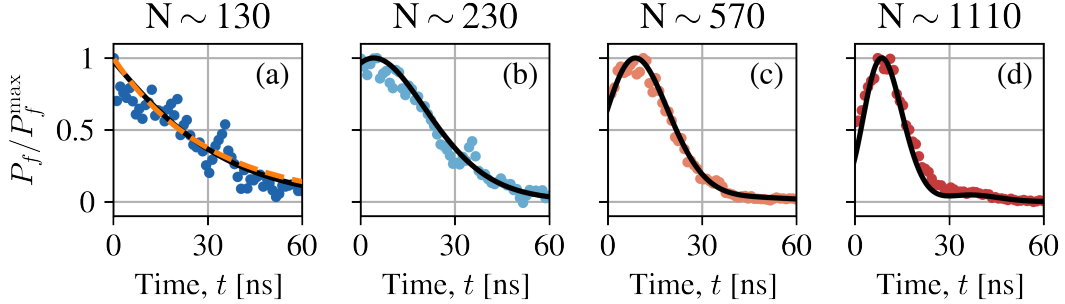


Figure 5.2: Decay dynamics of the power, P_f , for ensembles consisting of a varying number of maximally inverted atoms, N . Superradiant burst dynamics only occurs beyond a certain threshold atom number. The MCSA predictions are shown as black lines. In (a), we also plot the exponential decay that is expected for independently emitting atoms as a dashed orange line.

with a given atom number, N , we scan P_1 before each measurement. We then chose the power at which the maximal number of photons is absorbed from the excitation pulse, see section 4.1.4.

In Fig. 5.2(a), we show the decay dynamics for about 130 maximally inverted atoms. We observe a monotonously decaying power, P_f . The dynamics is well described by the MCSA model (black line), which almost coincides with the exponential decay of an independently emitting ensemble (orange dashed line). As we increase the number of atoms to about 230, see panel (b), we first observe a plateau before the power eventually decreases. This indicates that N is close to the threshold atom number for the onset of superradiant burst dynamics. We note that this threshold is larger than what is expected from the analytical result, $N \approx 100$, see Eq. (3.15). This is due to the inhomogeneous spread of coupling strengths, β_f . Using the MCSA, we extract that the spread of β_f in our experiment increases the threshold atom number to 146. Finally, we observe a clear burst for 570 atoms, which becomes even more pronounced for 1100 atoms. We repeat the measurement shown in Fig. 5.2 for even more different atom numbers and extract the peak power emitted into the waveguide, P_f^{\max} , for each time trace. Figure 5.3(a) shows the scaling of P_f^{\max} with N on a log-log scale. One can clearly observe two different regimes. For small atom numbers, we observe a linear scaling. Fitting a power law to the data for atom numbers smaller than 300 gives an exponent of 1.0(2), see red dashed line¹. In this regime, the peak power occurs directly after the switch-off of the excitation laser, i.e.,

¹Fitting function: $P_f^{\max}(N) = AN^\alpha$

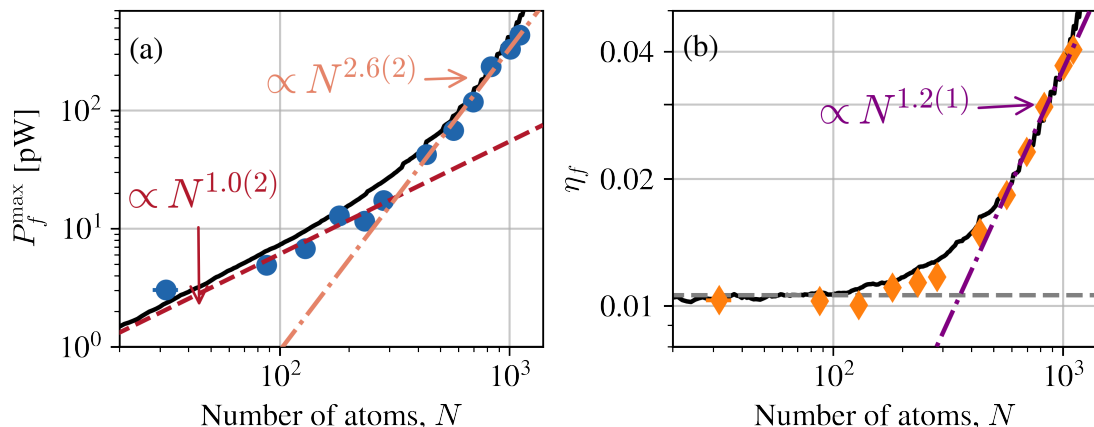


Figure 5.3: Dependence of superradiant burst dynamics on the number of atoms, N . (a) Scaling of the peak power, P_f^{\max} , with N . (b) Scaling of the fraction of stored energy that is emitted into the forward direction, η_f . Note that both panels feature a log-log scale, such that a power-law scaling with exponent α appears as a straight line with slope α .

$t = 0$ ns, see Fig. 5.1. If the atoms emit independently, this peak power is given by

$$P_f^{\max} = P_f(t = 0 \text{ ns}) = \beta_f \Gamma E_{\text{st}}. \quad (5.1)$$

Here, $E_{\text{st}} = p_{\text{exc}} \hbar \omega N$ is the energy stored in an ensemble with average excited state probability p_{exc} at time $t = 0$ ns, which is radiated with a rate $\beta_f \Gamma$ into the forward-propagating mode. By fitting a linear function without offset to the data in Fig. 5.3(a) for small N , we can extract an average excited state probability of $p_{\text{exc}} = 0.77(10)$ using Eq. (5.1), which is consistent with the measurements based on the number of absorbed photons per atom in section 4.1.4. There, we inferred $p_{\text{exc}} = 0.76(1)$ by measuring the number of absorbed photons per atom for about 300 atoms. For larger atom numbers, the scaling changes. Fitting the data for atom numbers larger than 300, we find a power law exponent of 2.6(2). In the standard case of Dicke superradiance, each atom adds constructively to the total dipole moment of the ensemble once the atomic dipoles have synchronized. Therefore, the emitted peak power increases quadratically, since it is proportional to the dipole moment squared. In this idealized scenario, it is assumed that all atoms couple exclusively to a single optical mode. Therefore, the entire energy stored in the atomic ensemble, E_{st} , must be radiated into this mode, whether the dipoles synchronize or not. However, in our case, the coupling strength of each atom to the shared optical mode, i.e., the forward-propagating nanofiber-guided mode, is only about 1 %. This means that a single atom emits 99 % of its radiation into independent free-space modes. As the

superradiant burst emerges, the atoms synchronize via the forward-propagating mode, such that each atomic dipole acquires an additional propagation phase. The resulting phase pattern leads to constructive interference in the forward direction. Similar to a phased antenna array, the ensemble then emits into a narrower solid angle, as the number of atoms is increased [116]. Therefore, a larger fraction of the emitted light is coupled into the nanofiber-guided mode, since the latter acts as a fixed aperture for the emission pattern. This collectively enhanced coupling efficiency explains the faster-than-quadratic scaling of the peak power with the number of atoms observed in the experiment.

To check the validity of this explanation, we extract the fraction of the stored energy that is emitted into the forward direction, η_f , as we did in section 4.2. Note that we use the SPCM signal to extract η_f from our measurements since the signal from the hybrid photodetector is saturated during the duration of the excitation pulse, see section 2.4. In Fig. 5.3(b), we plot η_f as a function of the number of inverted atoms, N . Also here, we observe a threshold behavior. For small N , η_f stays at a constant value of $\eta_f \approx \beta_f \approx 0.01$, which is what is expected for independently decaying atoms, see gray dashed line. As N surpasses the threshold, beyond which we observe a superradiant burst, η_f starts to increase with a power law exponent of 1.2(1), see purple dash-dotted line. The increase of η_f means that the scattering into the forward-propagating mode is indeed collectively enhanced.

Importantly, this enhancement of η_f has a fundamentally different origin than the enhancement we observed in section 4.2. Also there, the enhancement was due to a phase pattern across the atomic ensemble, which lead to constructive interference in the forward direction. However, in the weak excitation regime, the phases are determined by the excitation laser, which prepares the ensemble close to a timed Dicke state. In contrast, for an initially fully inverted ensemble, the phase pattern emerges spontaneously through the synchronization of the atomic dipoles during their decay. We will pick up on this notion in section 5.5, where we will analyze the coherence properties of the superradiant burst in more detail.

5.3 Scaling in the large- N limit

While it is technically challenging to increase the number of inverted atoms much further in our experiment, we can use the MCSA model to investigate the scaling of the superradiant burst for larger N . To do so, we assume a perfectly homogeneous coupling strength of $\beta_f = 0.011$ as well as perfect inversion at time $t = 0$. In Fig. 5.4(a), we plot the simulated peak-emitted power, P_f , as a function of N as a black line. We observe three different regimes of scaling. For small atom numbers, the peak power scales linearly

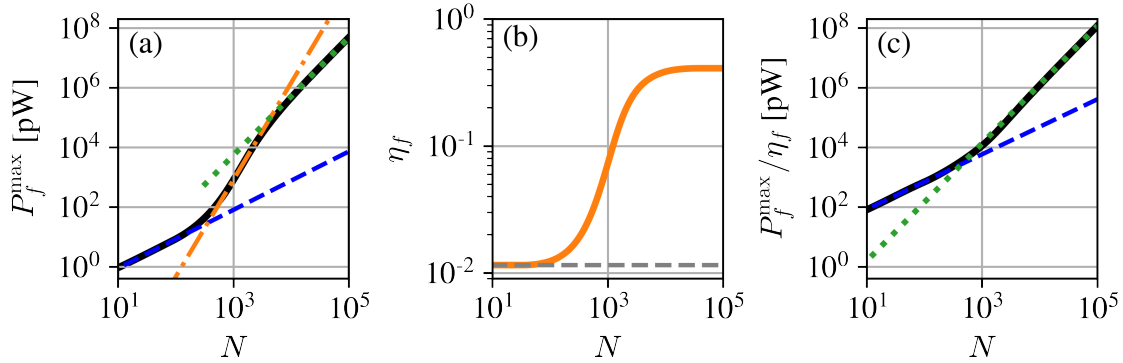


Figure 5.4: MCSA predictions for the scaling of different quantifiers of the superradiant burst with the number of atoms, N . We assume a perfectly homogeneous atom-waveguide coupling strength of $\beta_f = 0.011$ and perfect inversion at time $t = 0$ ns. (a) We observe three regimes, in which P_f^{\max} scales linearly (blue dashed line), super-quadratically (orange dash-dotted line), and quadratically (green dotted line) with N , respectively. (b) For large N , η_f reaches a plateau value of about 0.4. (c) Dividing P_f^{\max} by η_f eliminates the effect of collectively enhanced forward scattering, and, consequently, the super-quadratic scaling is reduced to quadratic scaling.

with N , see blue dashed line. As the threshold atom number for the occurrence of a superradiant burst is surpassed, the scaling becomes faster than quadratic, as observed in our experiment. For atom numbers between 500 and 2000, we fit a power law exponent of 3.25, see orange dash-dotted line. We numerically checked that the difference to the experimentally observed exponent of 2.6(2) is mainly due to the inhomogeneous spread of coupling strengths, β_f . Eventually, the scaling approaches a quadratic scaling for even larger N , see green dotted line. This is expected in the limit of large N , if we attribute the super-quadratic scaling of P_f^{\max} to an increase of the collective coupling efficiency, η_f since the latter can not become larger than 1. Therefore, the scaling of P_f^{\max} reduces to a quadratic scaling as η_f saturates. In panel (b), we plot η_f as a function of N . As expected, η_f saturates for large N , however, at a maximal value of about 0.4, i.e., substantially smaller than 1.

Finally, in panel (c), we divide P_f^{\max} by the collective coupling efficiency, η_f , in order to eliminate the effect of collectively enhanced forward scattering. Indeed, we observe only two different scaling regimes: linear (blue dashed line) and quadratic (green dotted line). This further consolidates our hypothesis that the observed super-quadratic scaling of P_f^{\max} with N appears due to an increased coupling efficiency to the forward-propagating mode, in addition to the usual quadratic enhancement, which is expected for Dicke-like superradiant bursts.

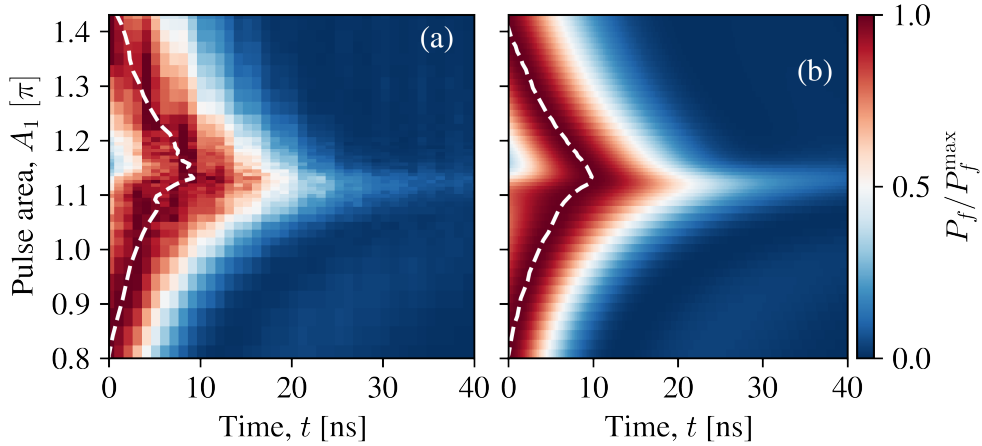


Figure 5.5: Dynamics of the power, P_f , for different pulse areas, A_1 , after switching off the excitation pulse at time $t = 0$ ns. Each time trace is normalized by the peak-emitted power, P_f^{\max} . The ensemble consists of about 1000 atoms and is maximally inverted for a pulse area of $A_1^{\max \text{ inv.}} = 1.12 \pi$. Panel (a) shows the measured data, and panel (b) the corresponding MCSA predictions. The time at which the peak power is emitted, t_D , is indicated as dashed white lines.

5.4 Superradiant burst dynamics for a finite initial dipole moment

A lot of the scientific literature on superradiant burst dynamics has focused on the case of fully inverted ensembles, where the atomic dipole moment is initially zero. In this case, the superradiant burst is seeded by spontaneous or fluorescent emission. Accordingly, superradiant burst dynamics of an initially fully inverted medium is also called superfluorescence [127–129]. However, coherent pulsed excitation of states with a finite dipole moment has already been discussed in the very first paper on superradiance by Dicke [9]. Various works have focused on the influence of an initial, so-called tipping angle, which can be introduced intentionally in order to seed the emission of a superradiant burst [15, 130, 131]. In our case, we coherently excite the ensemble using Rabi pulses, such that we can control the excited state probability, as well as the magnitude of the induced dipole moment via the pulse area, A_1 , see section 4.1. In Fig. 5.5(a), we show time traces of the power emitted into the forward-propagating mode, P_f , for different pulse areas, A_1 , as a colormap for about 1000 atoms. In panel (b), we show the corresponding MCSA prediction, which is in excellent agreement with the experimental data. We note that, in both panels, each time trace is normalized by its peak-emitted power, P_f^{\max} . The delay time, t_D , at which this peak power occurs is shown as the dashed white line. Importantly,

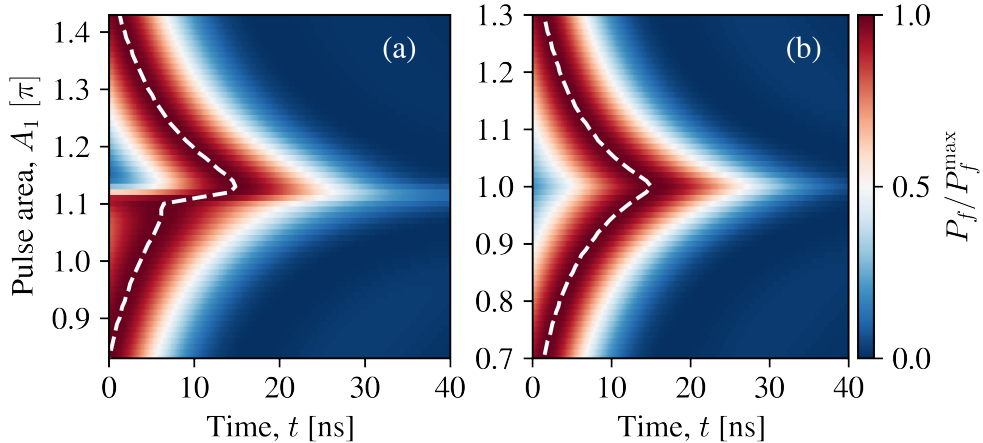


Figure 5.6: Comparison of two different MCSA predictions for the dynamics of the power emitted by 1000 atoms into the forward-propagating mode, P_f , as a function of the pulse area, A_1 . In both (a) and (b), we assume perfectly homogeneous coupling strengths, $\beta_f=0.011$. In (b), we additionally assume that each atom is initially prepared in the ideal state, $|\psi_0\rangle$.

a time delay larger than zero indicates that a burst occurs.

As before, the excitation pulse is switched off at time $t = 0$ ns (not shown). For $A_1 < 0.8\pi$, the maximally emitted power occurs right after switching off the excitation pulse, i.e., $t_D = 0$, and no burst occurs. As we increase the pulse area further, the time delay grows, and a superradiant burst becomes apparent. The maximal delay of $t_D \approx 9$ ns is reached for a pulse area of $A_1^{\max \text{ inv.}} = 1.12\pi$, i.e., it coincides with maximal inversion of the atomic ensemble. Recall that maximal inversion occurs at a pulse area slightly larger than π due to absorption of the excitation pulse along the ensemble. Consequently, the pulse area seen by the first atom, A_1 , is always slightly larger than the average pulse area seen by the ensemble. Indeed, our simplified model of pulse absorption, see section 4.1.2, predicts that maximal inversion should be reached for $A_1^{\max \text{ inv.}} = 1.13\pi$ for our parameters. For even larger pulse areas, the ensemble is coherently de-excited, and the burst vanishes.

Notably, the time traces are not symmetric with respect to maximal inversion. First, the delay t_D is larger for $A_1 > A_1^{\max \text{ inv.}}$ than for $A_1 < A_1^{\max \text{ inv.}}$. Second, the burst seems to be more pronounced for $A_1 > A_1^{\max \text{ inv.}}$, i.e., the ratio between the peak power, P_f^{\max} , and the power at time $t = 0$ ns is larger. Both of these asymmetric features also appear in the MCSA simulation, such that we can assume that the observed asymmetry has a physical, rather than technical reason. In order to further investigate the origin of this asymmetry, we compare different MCSA predictions.

In Fig. 5.6(a), we show the MCSA predictions assuming a perfectly homogeneous coupling

strength, β_f . Qualitatively, the dynamics is very similar to what we observe in the experiment, see Fig. 5.5(a). In particular, the asymmetry with respect to full inversion is even more pronounced. In panel (b), we assume, in addition to perfectly homogenous coupling, that the ensemble is prepared in $|\psi_0\rangle$ at time $t = 0$ ns. We thus neglect the dynamics during the excitation pulse. Then, the asymmetry disappears, and the maximal delay appears at a pulse area of $A_1 = \pi$, since now each atom is initially excited with the same pulse area. These observations suggest that the asymmetry with respect to full inversion is due to a partial absorption of the excitation pulse along the atomic ensemble. The pulse area seen by the atoms decreases along the ensemble, such that each atom is initially prepared in a slightly different state. Since we work with a cascaded quantum system, the first atom emits independently, while the last atom is driven by the light emitted by the entire ensemble. For an average pulse area slightly larger than π , the last atom is prepared closer to full inversion than the first atom, such that the superradiant burst dynamics is more pronounced than for average pulse areas slightly smaller than π .

5.5 Coherence properties of the superradiant burst

In the previous sections, we have interpreted the occurrence of a superradiant burst as the build-up of coherence between the atoms. This interpretation is backed by several observations that are indirectly linked to the coherence of the burst: The fraction of forward-emitted energy, η_f , is collectively enhanced even for maximal inversion, and we have observed a superlinear scaling of the maximally emitted power, P_f , with the number of atoms. To directly analyze the coherence properties of a light field, one typically measures the so-called correlation functions.

5.5.1 Two-time correlation functions

The temporal first- and second-order correlation functions of a light field described by the annihilation operator, $\hat{a}(t)$, and power $P(t) = \langle \hat{a}^\dagger(t)a(t) \rangle$ are defined as [132]:

$$\begin{aligned}
 G^{(1)}(t, \tau) &= \langle \hat{a}^\dagger(t)\hat{a}(t + \tau) \rangle, \\
 g^{(1)}(t, \tau) &= \frac{G^{(1)}(t, \tau)}{\sqrt{P(t)P(t + \tau)}}, \\
 G^{(2)}(t, \tau) &= \langle \hat{a}^\dagger(t)\hat{a}^\dagger(t + \tau)\hat{a}(t + \tau)\hat{a}(t) \rangle, \\
 g^{(2)}(t, \tau) &= \frac{G^{(2)}(t, \tau)}{P(t)P(t + \tau)}.
 \end{aligned}
 \tag{5.2}$$

Here, $g^{(1)}(t, \tau)$ and $g^{(2)}(t, \tau)$ denote the normalized first-order and second-order correlation functions, respectively. Their physical meaning is the correlation between the field (intensity) at time t with the field (intensity) at a later time, $t + \tau$. Therefore, the first-order correlation is called field-field correlation, and the second-order correlation is called intensity-intensity correlation.

In the case of a stationary light field, one can integrate over t and it is sufficient to describe the correlation functions in terms of the delay time τ ,

$$\begin{aligned} G^{(1)}(\tau) &= E_t \left[\langle \hat{a}^\dagger(t) \hat{a}(t + \tau) \rangle \right], \\ g^{(1)}(\tau) &= \frac{G^{(1)}(\tau)}{E_t[P(t)]}, \\ G^{(2)}(\tau) &= E_t \left[\langle \hat{a}^\dagger(t) \hat{a}^\dagger(t + \tau) \hat{a}(t + \tau) \hat{a}(t) \rangle \right], \\ g^{(2)}(\tau) &= \frac{G^{(2)}(\tau)}{E_t[P(t)]^2} \end{aligned} \tag{5.3}$$

where $E_t[x(t)]$ denotes the average over time,

$$E_t[x(t)] = \lim_{T \rightarrow \infty} \left(\frac{1}{T} \cdot \int_{-T/2}^{T/2} x(t) dt \right). \tag{5.4}$$

The normalized first-order correlation function can take values from -1 to 1 and is often described as the degree of first-order coherence since it determines, e.g., the visibility of the interference fringes as a function of the delay time between the two paths, τ . Moreover, according to the Wiener-Khinchin theorem, $g^{(1)}(\tau)$ is related to the power spectrum of the light via the Fourier transform. We also note that, per construction, $g^{(1)}(t, t) = 1 \forall t$ and $g^{(1)}(0) = 1$.

We note that one should take care when interpreting the two-time first-order coherence. For example, a single atom that is inverted at time $t = 0$ emits a field for which $g^{(1)}(t, t + \tau) = 1$, i.e., it does not decrease with time, see section A.6 in the Appendix. This is despite the fact that the process of spontaneous emission is intrinsically incoherent. Indeed, when averaging over time, we obtain $g^{(1)}(\tau) = e^{-\Gamma\tau/2}$.

Finally, we introduce the normalized first-order cross-correlation function between two light fields, $\hat{a}_1(t)$ and $\hat{a}_2(t)$, with powers $P_1(t)$ and $P_2(t)$,

$$\begin{aligned} g_{12}^{(1)}(t, \tau) &= \frac{\langle \hat{a}_1^\dagger(t) \hat{a}_2(t + \tau) \rangle}{\sqrt{P_1(t)P_2(t + \tau)}}, \\ g_{12}^{(1)}(\tau) &= \frac{E_t \left[\langle \hat{a}_1^\dagger(t) \hat{a}_2(t + \tau) \rangle \right]}{E_t \left[\sqrt{P_1(t)P_2(t)} \right]}. \end{aligned} \tag{5.5}$$

Analogous to the first-order (auto-) correlation function, the first-order cross-correlation function gives the visibility of the interference fringes when overlapping the two light fields. For a value of $g_{12}^{(1)}(t, \tau) = 1$, we can thus say that the two fields are coherent with respect to each other. After these definitions, we now turn to our experiment again.

5.5.2 Heterodyne measurement of the superradiant burst

We overlap the light emitted into the forward-propagating mode with a detuned local oscillator (LO), see detection setup in section 2.4. This technique is called heterodyne detection [133]. The LO is a continuous-wave field, which is split off the excitation laser field before the optical pulses are generated. We detune the LO field by $\omega_{\text{LO}} = 2\pi \times 230$ MHz from the excitation laser field using an acousto-optical modulator. If the superradiant burst is coherent with respect to the excitation laser field (and consequently, the local oscillator field), the heterodyne signal should thus feature a beat pattern that oscillates at a frequency of ω_{LO} . However, in our experiment, the relative phase, θ_{LO} , between the local oscillator and the excitation laser field is not actively stabilized. Therefore, θ_{LO} drifts substantially during the 80 ms-long probing sequence due to random thermal and acoustic fluctuations. Since our signal-to-noise ratio is not sufficient for single-shot detection, we have to average the heterodyne signal over many experimental realizations, such that the drift of θ_{LO} dephases any interference pattern. To circumvent this problem, we compute the normalized second-order (intensity-intensity) correlation function of the heterodyne signal, $g_D^{(2)}(t, \tau)$. When the power of the local oscillator is much larger than the superradiant burst signal, $g_D^{(2)}(t, \tau)$ is given by the following expression, see Appendix A.5 for a full derivation,

$$g_D^{(2)}(t, \tau) = 1 + V_{\text{max}}(t, \tau) \cos(\omega_{\text{LO}}\tau) g^{(1)}(t, \tau). \quad (5.6)$$

The intensity-intensity correlation of the heterodyne signal is thus given by the field-field correlation of the superradiant burst signal, $g^{(1)}(t, \tau)$, and oscillates around 1 with the local oscillator frequency, ω_{LO} . The maximal visibility of this beat pattern, $V_{\text{max}}(t, \tau)$, is determined by the power of the local oscillator field, P_{LO} , and the power of the light emitted into the forward-propagating mode, $P_f(t)$,

$$V_{\text{max}}(t, \tau) = \frac{2P_{\text{LO}}\sqrt{P_f(t)P_f(t+\tau)}}{[P_{\text{LO}} + P_f(t)][P_{\text{LO}} + P_f(t+\tau)]}. \quad (5.7)$$

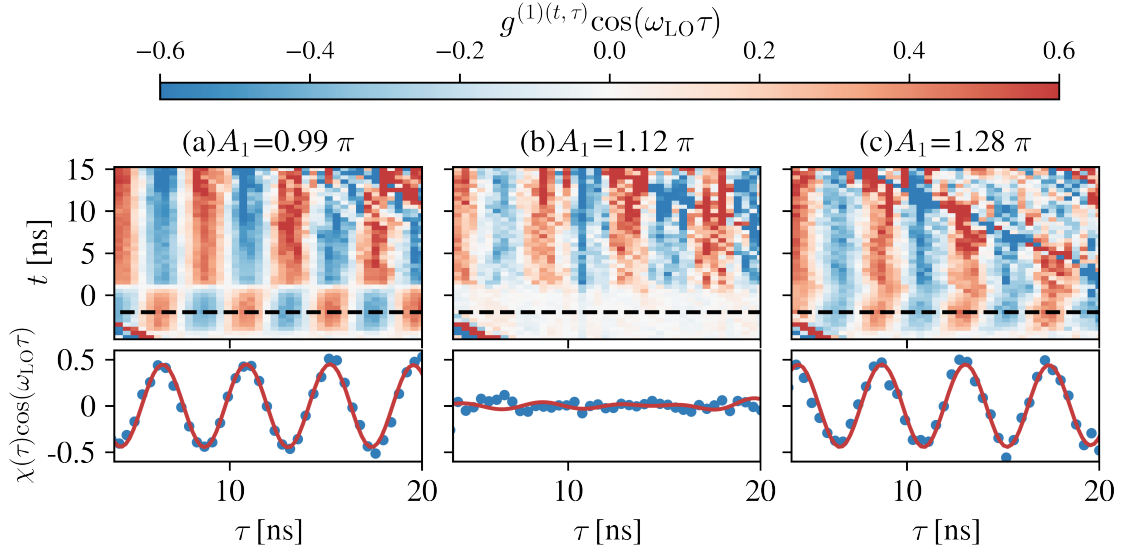


Figure 5.7: First-order coherence function of the light exiting the nanofiber in the forward direction, oscillating at the local oscillator detuning ω_{LO} . The pulse areas are $A_1 = 0.99\pi$, 1.12π , and 1.28π in (a), (b), and (c), respectively. As before, the excitation pulse is switched off at $t_1 = 0$ ns. Note that a pulse area of $A_1^{\text{max inv.}} = 1.12\pi$ in panel (b) maximally inverts the ensemble of about 1000 atoms.

Top part: Two-time first-order coherence function as a color plot.

Bottom part: Cut through the color plot along the black dashed line, i.e., $t = -2$ ns. For $t < 0$, the first-order coherence function can be interpreted as the first-order cross-correlation function between the excitation laser field and the superradiant burst, $\chi(\tau)$.

We can thus extract the following quantity by measuring both $V_{\text{max}}(t, \tau)$ and $g_D^{(2)}(t, \tau)$,

$$\cos(\omega_{\text{LO}}\tau)g^{(1)}(t, \tau) = \frac{g_D^{(2)}(t, \tau) - 1}{V_{\text{max}}(t, \tau)}. \quad (5.8)$$

Since we measure both the time-dependent power of the signal field and the power of the local oscillator field, it is straightforward to extract $V_{\text{max}}(t, \tau)$ from the experimental data. However, the measurement of the intensity-intensity correlation, $g_D^{(2)}(t, \tau)$, usually requires two detectors in a so-called Hanbury-Brown-Twiss configuration since our detectors are not photon-number resolving. However, here, we are not interested in the correlation functions for zero time delay, $\tau = 0$ ns, since the field-field correlation, $g^{(1)}(t, t)$, is equal to one per definition. Since the hybrid photodetector features a dead time of only about 2 ns, we can measure $g_D^{(2)}(t, \tau)$, for $\tau > 2$ ns, even with one detector.

In the top part of Fig. 5.7, we show the first-order correlation function of the light exiting

the nanofiber oscillating at the local oscillator detuning, $\cos(\omega_{\text{LO}}\tau)g^{(1)}(t, \tau)$, as a function of t and τ as a color map. In (a), (b), and (c), we show measurements for about 1000 trapped atoms and pulse areas of $A_1 = 0.99\pi, 1.12\pi$, and 1.28π , respectively. As before, the excitation laser pulse is switched off at time $t_1 = 0$ ns.

For $t > 0$ ns, we observe oscillations with large contrast, irrespective of the pulse area. By extrapolating the oscillations to $\tau = 0$ ns, we infer that the first-order coherence is positive-valued.

For $t < 0$ ns, the signal exiting the nanofiber is dominated by the excitation laser pulse since the power of the latter is much larger than the power of the light emitted by the atoms. Thus, $g^{(1)}(t < 0, \tau > -t)$ can be interpreted as the first-order cross-correlation function between the excitation laser field and the field emitted by the atoms. We plot the quantity $\mathcal{X}(\tau) = g^{(1)}(t = -2 \text{ ns}, \tau)$, modulated with the local oscillator detuning, in the lower part of Fig. 5.7. The modulus of $\mathcal{X}(\tau)$, i.e., the visibility of the oscillations, quantifies the coherence of the superradiant burst with respect to the excitation laser field. Its sign is equal to the relative phase factor, $e^{i\theta_{\text{rel}}}$ between the excitation laser field and the superradiant burst. This phase factor can only be equal to 1 or -1 for resonant excitation, corresponding to a relative phase of $\theta_{\text{rel}} = 0$ or $\theta_{\text{rel}} = \pi$, respectively, see Appendix A.5. In (a), the pulse area, $A_1 = 0.99\pi$, is slightly smaller than the pulse area required to maximally invert the ensemble, $A_1^{\text{max inv.}} = 1.12\pi$. We observe oscillations with large contrast, i.e., the light emitted by the atoms is coherent with respect to the excitation laser field. We extrapolate that $\mathcal{X}(\tau)$ is negative, i.e., the light emitted by the atoms is phase shifted by π with respect to the excitation laser field. This is expected for pulse areas smaller than $A_1^{\text{max inv.}}$ since the field radiated by the induced atomic dipoles oscillates π out of phase with the excitation laser field, see section 4.1. This phase shift can also be seen in the top part of panel (a), where we observe a clear phase jump of π as t changes from negative to positive values.

In (b), the pulse area of $A_1 = 1.12\pi$ is chosen such that the atomic ensemble is maximally inverted at time $t = 0$ ns. Then, the induced atomic dipole moment is zero, and correspondingly, there is no fixed phase relationship with respect to the excitation laser field. Indeed, we practically do not observe oscillations in the lower panel of (b), i.e., $\mathcal{X}(\tau) \approx 0$. This confirms that the light emitted by the atoms is incoherent with respect to the excitation laser field.

Finally, in (c), the pulse area of $A_1 = 1.28\pi$ is slightly larger than $A_1^{\text{max inv.}}$. Again, we observe oscillations with large visibility, i.e., the emitted light is coherent with respect to the excitation laser field. In contrast to the data shown in (a), here we extract a relative phase of zero, indicating that the emitted light oscillates in phase with the excitation laser field. Also this behavior is expected since the average induced atomic dipole switches sign

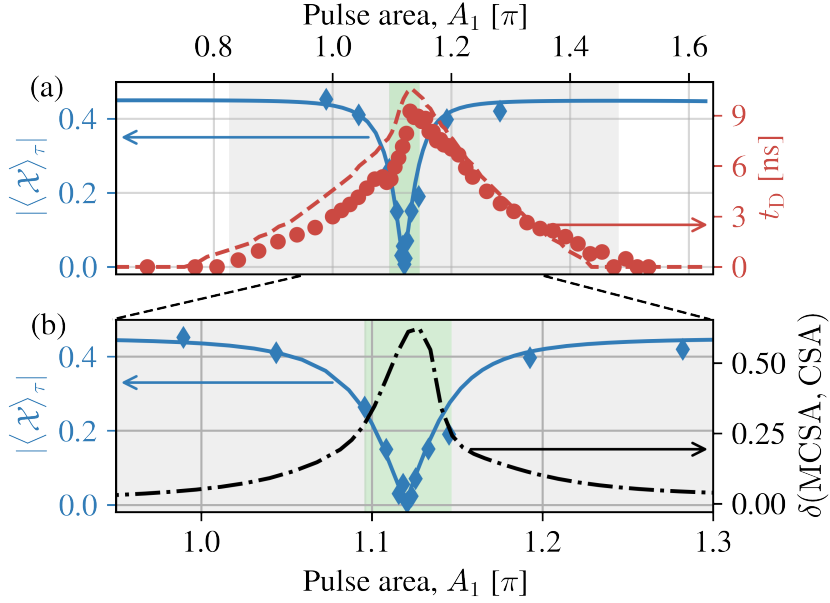


Figure 5.8: (a) Average coherence of the superradiant burst with respect to the excitation laser field, $|\langle \mathcal{X} \rangle_\tau|$, and time delay of the peak-emitted power, t_D , as a function of the pulse area, A_1 . The corresponding MCSA model predictions are shown as a solid blue and dashed red line, respectively. We observe a time delay of $t_D > 0$ ns over a wide range of pulse areas, see gray shaded area, indicating that a superradiant burst occurs. We observe superradiant bursts that are incoherent with respect to the excitation laser only for a narrow range of pulse areas, see green shaded area. This regime coincides with the regime in which it is necessary to model the dynamics with the MCSA model. Panel (b) shows a zoom into (a), where we again plot $|\langle \mathcal{X} \rangle_\tau|$ in blue, as well as the relative difference between the MCSA and CSA predictions as the black dash-dotted line.

when the pulse becomes larger than $A_1^{\text{max inv.}}$, such that the emitted light is in phase with the driving field.

5.5.3 Identification of two regimes of burst dynamics

In section 5.4, we have investigated the superradiant burst dynamics as a function of the initial excitation. In particular, we extracted the time t_D , at which the peak power emitted into the forward-propagating mode, P_f^{max} , is reached. Let us recall that a time delay of $t_D > 0$ ns indicates the occurrence of a superradiant burst.

In the previous section 5.5.2, we have analyzed the coherence properties of the superradiant burst. In particular, we extracted the first-order cross-correlation function between the

excitation laser field and the superradiant burst, $\mathcal{X}(\tau)$, oscillating at the local oscillator detuning, ω_{LO} , see bottom part of Fig. 5.7. We now fit this quantity using a cosine function, with only an amplitude C as a free fit parameter. The fitted amplitude corresponds to $\mathcal{X}(\tau)$, averaged over $\tau \in [4, 20]$ ns. Its modulus quantifies the average coherence with respect to the excitation laser field, $|\langle \mathcal{X} \rangle_\tau|$.

We now compare the two sets of measurements discussed in sections 5.4 and 5.5.2 by plotting both t_D and $|\langle \mathcal{X} \rangle_\tau|$ as a function of the pulse area, A_1 , in Fig. 5.8(a). The solid blue and dashed red lines show the corresponding MCSA predictions. We find that $|\langle \mathcal{X} \rangle_\tau|$ vanishes in a very narrow range of pulse areas, A_1 , in excellent agreement with the MCSA prediction. In this regime, the light emitted by the atoms is incoherent with respect to the excitation laser field. However, superradiant burst dynamics, characterized by a non-zero time delay, t_D , occurs over a much wider range of pulse areas. This allows us to identify two regimes of superradiant burst dynamics.

In the first regime, we observe superradiant bursts that are coherent with respect to the excitation laser field, see gray shaded area in Fig. 5.8. This occurs when the pulse area is well below or above the pulse area required to maximally invert the ensemble, but the average excited state probability is still substantially larger than 0.5. Then, the laser induces an initial atomic dipole moment, d_0 , which further builds up during the decay, resulting in the emission of a burst. The induced dipole moment features a fixed phase relationship with the excitation laser field, which is inherited by the light emitted by the atoms after the excitation pulse is switched off. In particular, the superradiant burst is either in phase ($A_1 < A_1^{\text{max inv.}}$) or π out of phase ($A_1 > A_1^{\text{max inv.}}$) with the excitation laser field, see Fig. 5.7.

In the second regime, see green shaded area in Fig. 5.8, we observe superradiant bursts that are incoherent with respect to the excitation laser field, i.e., $|\langle \mathcal{X} \rangle_\tau| \approx 0$. There, the initial dipole moment of the ensemble practically vanishes. The build-up of coherence during the decay is thus seeded by vacuum fluctuations. This process is indeed a spontaneous synchronization of the atomic dipoles since, in this regime of superfluorescence, there is no external reference that determines the phase of the emitted light.

Figure 5.8(b) shows a zoom into panel (a), where we again plot $|\langle \mathcal{X} \rangle_\tau|$, as well as the relative difference between the MCSA and CSA prediction, $\delta(\text{CSA})$, as a black dash-dotted line². The superfluorescent regime, i.e., the green shaded area, coincides with the regime in which the MCSA prediction substantially differs from the CSA prediction. There, the atomic dynamics is predominantly driven by incoherently emitted light, which is not captured in the CSA. For pulse areas in the gray shaded area, the initially induced average dipole moment, d_0 , is large enough such that the atomic dynamics is driven by

²We use the same definition for the relative difference δ as in section 3.5, see Eq.(3.31)

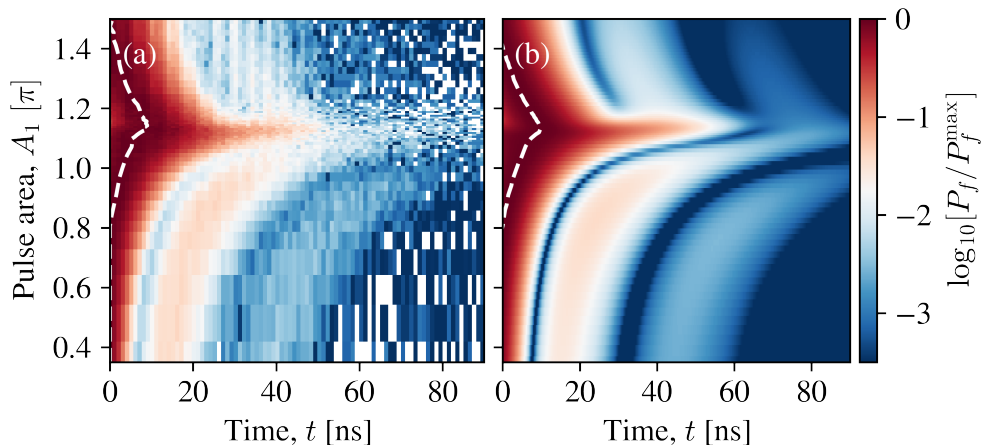


Figure 5.9: Time traces of the power emitted into the forward-propagating mode, P_f , for different pulse areas, A_1 , as a color map with logarithmic scaling. Except at the point of maximal inversion, we observe minima of the emitted power, which indicates that the ensemble has evolved into a subradiant state. (a) shows the measured data, and (b) the corresponding MCSA model prediction.

coherently emitted light. In this regime of “laser-seeded” superradiant bursts, the CSA models the dynamics reasonably well, i.e., it deviates by less than about 20 % from the MCSA prediction.

5.6 Subradiant dynamics following a superradiant burst

So far, we have focused on the dynamics shortly after switching off the excitation laser pulse. This early dynamics is dominated by superradiant, i.e., collectively enhanced emission. Following this initial superradiant dynamics, collectively inhibited decay has been observed in dilute clouds of cold atoms in the weak excitation regime [36]. This phenomena is termed “subradiance” and has since been studied in a variety of different atomic systems [39, 51, 63, 134].

In particular, subradiance has been observed in waveguide QED in the form of sudden, temporary switch-offs of the optical power emitted into the waveguide [45, 47, 135]. This phenomenon is well captured by linear response theory and has, e.g., also been observed in the resonant transmission of synchrotron radiation through effectively continuous media, such as metal foils [136]. For an ensemble consisting of a discrete number of emitters, one can understand this dynamics as a coherent evolution of the atomic state through all $N - 1$ subradiant states of the single-excitation manifold, as described in Ref. [47]: Initially, a weak, resonant laser pulse prepares the atoms in the so-called timed Dicke

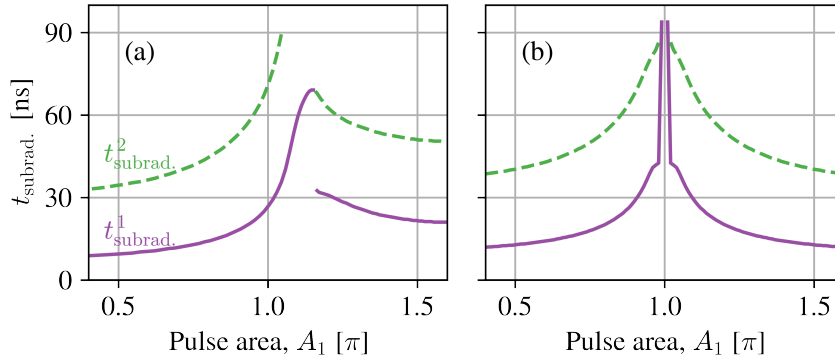


Figure 5.10: MCSA predictions for the times at which the first and second minimum of the forward-emitted power, P_f , occurs, as a function of pulse area, A_1 . (a) We also simulate the excitation dynamics and assume an inhomogeneous spread of coupling strengths, β_f . (b) We assume perfectly homogeneous coupling strengths and that each atom is initially prepared in the ideal state, $|\psi_0\rangle$.

state, see Eq. (4.14), which is superradiant with respect to the forward-propagating guided mode. However, one can also define a set of $N - 1$ orthogonal single-excitation states, which are subradiant, i.e., the corresponding phase patterns interfere destructively in the forward-propagating mode. As the ensemble decays, its state passes through all $N - 1$ subradiant states, and correspondingly, the optical power features $N - 1$ minima [47]. We note that this decay dynamics is of course still primarily dissipative and that the coherent evolution through the subradiant states only occurs until a photon has been emitted. Beyond the regime of linear response, the interpretation becomes more complex since there are many more states that the system can explore.

Here, we observe subradiant dynamics that is very similar to what was reported in Refs. [45, 47, 135], even beyond the weak excitation regime. To make these features more visible, we plot time traces of the power, P_f , as a function of A_1 as a color map with logarithmic scaling in Fig. 5.9(a). We note that this data is taken from the same set of measurements that is depicted in Fig. 5.5. As before, we plot the time delay, t_D , as a white dashed line. For the smallest pulse areas, A_1 , we observe two minima in the emitted power, P_f . As we increase A_1 , these minima occur at later times. For $A_1 \approx 1.12\pi = A_1^{\max \text{ inv.}}$, i.e., maximal inversion, we do not observe a clear minimum anymore. Finally, for $A_1 > A_1^{\max \text{ inv.}}$, there is again at least one minimum. The corresponding MCSA prediction is shown in panel (b) and qualitatively agrees with our experimental data.

In the following, we denote the time at which the k th minima of P_f occurs as $t_{\text{subrad.}}^k$. We note that the occurrence of a minimum in the emitted power is not necessarily synonymous

to a subradiant decay. A better definition of subradiance involves the ensemble decay rate [47],

$$\Gamma_{\text{ens}}(t) = -\frac{\sum_{k=1}^N \dot{\rho}_{ee}^k(t)}{\sum_{k=1}^N \rho_{ee}^k(t)}. \quad (5.9)$$

The ensemble is subradiant when $\Gamma_{\text{ens}}(t) < \Gamma$. We numerically checked that t_{subrad}^k coincides with the time at which a local minimum of $\Gamma_{\text{ens}}(t)$ occurs, and that $\Gamma_{\text{ens}}(t) < \Gamma$. Therefore, we will treat the occurrence of a local minimum of P_f as an indicator for subradiance in the following.

We extract t_{subrad}^1 and t_{subrad}^2 from the MCSA predictions and plot them as a solid purple and dashed green lines in Fig 5.10(a), respectively. We observe that the first minimum for pulse areas of $A_1 > A_1^{\text{max inv.}}$ suddenly disappears as the pulse area approaches $A_1^{\text{max inv.}}$, while the second minimum smoothly transitions into the first minimum for pulse areas of $A_1 < A_1^{\text{max inv.}}$. Recall that we discussed a similar asymmetry with respect to maximal inversion for the delay time of the peak-emitted power, t_D , in section 5.4. There, we identified a systematic change of the induced atomic dipole moment along the atomic ensemble due to a partial absorption of the excitation pulse while propagating through the ensemble.

To check if the asymmetry for t_{subrad}^k also stems from a similar effect, we plot the MCSA prediction for perfectly homogeneous coupling, assuming that each atom is initially prepared in the same state, $|\psi_0\rangle$, in panel (b). Indeed, the times at which the minima of P_f appear are now completely symmetric around $A_1 = \pi$. This suggests that the asymmetry observed in (a) and, in particular, the connection of t_{subrad}^1 and t_{subrad}^2 is caused by an ordering of the atomic dipole moments along the ensemble due to the finite excitation pulse duration. Finally, when we neglect any experimental imperfections, see panel (b), we do not observe any minimum at all for pulse areas very close to π .

Importantly, we note that the MCSA prediction deviates from the dynamics predicted by solving the many-body master equation for longer times and full inversion, see section 3.5. The following analysis of the subradiant dynamics using the MCSA model is motivated by the qualitative agreement of our data with the MCSA model prediction away from full inversion.

5.6.1 Phase pattern of the subradiant states

To gain more insight into the physical mechanism underlying the subradiant dynamics, we perform an analysis similar to what was done in Ref. [47]. We simulate the dynamics of 1000 atoms that are each perfectly prepared in state $|\psi_0\rangle$ at time $t = 0$ ns using the MCSA model and neglect the inhomogeneous spread of β_f values. In Fig. 5.11, we plot

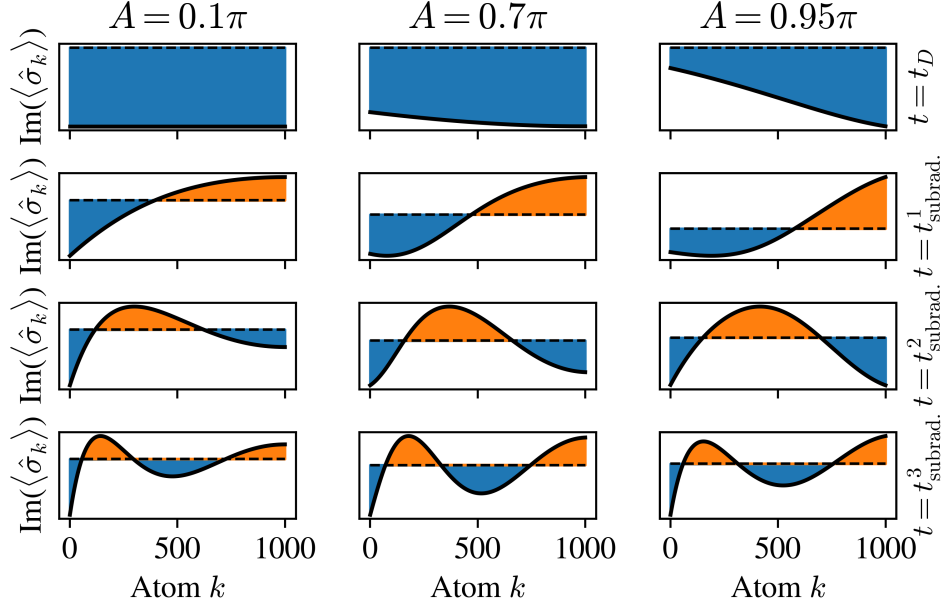


Figure 5.11: Values of $\text{Im}(\langle \hat{\sigma}_k \rangle)$ for different pulse areas, A . Positive and negative values are indicated in orange and blue, respectively. Each row corresponds to a different time, which is indicated on the right-hand side of the plot. At time t_D , the peak power, P_f^{\max} , is emitted into the forward-propagating mode. The time t_{subrad}^i corresponds to the time at which the i th local minimum of P_f occurs. We simulate the dynamics of 1000 atoms using the MCSA model, assuming perfect state preparation and homogeneous coupling strengths. Note that the units are arbitrary.

the values of $\text{Im}(\langle \hat{\sigma}_k \rangle)$, which are proportional to the atomic dipole moment of atom k at different times. The zeros in each plot are indicated as black dashed lines. Recall that the atomic dipole moment is imaginary for resonant excitation, see section 4.1. For the first row, we evaluate $\text{Im}(\langle \hat{\sigma}_k \rangle)$ at time $t = t_D$, i.e., the time at which the peak power is emitted into the forward-propagating mode. The second to fourth rows correspond to the times at which we observe the first to third subradiant state, respectively. In the first row, all dipole moments are negative and imaginary, i.e., they are all in phase. Indeed, we expect constructive interference of the atomic dipoles at the point of maximal emission. For $A = 0.7\pi$ and $A = 0.95\pi$, we observe that the magnitude of the dipole moment increases along the ensemble. In this regime, we observe a superradiant burst, which is coherent with respect to the excitation laser field, see section 5.5. The phase patterns of the subradiant states, see second to fourth row, are quite similar for all pulse areas. For the first subradiant state, we observe that one part of the ensemble

features negative imaginary dipole moments while the other part features positive imaginary dipole moments. These two “domains” interfere destructively, which leads to a minimum in the emitted power. For the second subradiant state, the total dipole moment also vanishes. However, now there are three domains, i.e., the imaginary parts of the dipole moments are negative for the first atoms, then positive, and again negative for the last atoms. Finally, there are four domains for the third subradiant state, and so on. In total, there are $N - 1$ ways to split the ensemble into such destructively interfering domains. This means that, at most, $N - 1$ minima of the forward-emitted power can occur.

We note that the last subradiant state corresponds to a configuration in which each atomic dipole moment points in the opposite direction of the dipole moment of the neighboring atom. For even longer times, $t > t_{\text{subrad.}}^{N-1}$, the dipole moments decrease in a non-uniform way, where the dipole moment of the last atoms decreases slower than the dipole moment of the first atoms. However, the alternating sign pattern resembles antiferromagnetic order, which is stable and does not change anymore.

5.6.2 Subradiant states for full inversion

The MCSA model does not predict subradiance for full inversion, see Fig. 5.10(b). However, when solving the many-body master equation in chapter 3, we have observed the occurrence of $N - 1$ minima of the emitted power even for full inversion. Note that, strictly speaking, $N - 1$ minima of the ensemble decay rate, Γ_{ens} , occur, which are not necessarily accompanied by local minima of the emitted power. For the following simulations, we checked that the times at which the respective minima of P_f and Γ_{ens} occur coincide. To investigate if this dynamics is related to the same mechanism of domain splitting observed in the previous section, we will calculate the dynamics for $N = 10$ atoms with unidirectional coupling, $\beta_f = 1$. One could again evaluate the expectation values of each atomic dipole moment at the times at which the different subradiant states are observed. However, for full inversion, $\langle \hat{\sigma}_k \rangle(t) = 0 \forall t$. Instead, we will calculate the expectation value of the correlation between the total dipole moment and the dipole moment of each atom, $\langle \hat{S}^\dagger \hat{\sigma}_k \rangle$. Here, \hat{S} is the collective lowering operator,

$$\hat{S} = \frac{1}{\sqrt{N}} \sum_{k=0}^N e^{ik_f z_k} \hat{\sigma}_k \quad (5.10)$$

We plot the strength of these correlations for each atom in Fig. 5.12 for different times. Importantly, we are mainly interested in the sign of each correlation, which is indicated by the light orange and light blue shaded bars, respectively. In (a), we evaluate the correlations at the time at which the peak power is emitted into the forward-propagating mode, t_D . There, all dipoles have the same sign, as before. For each subsequent subradiant

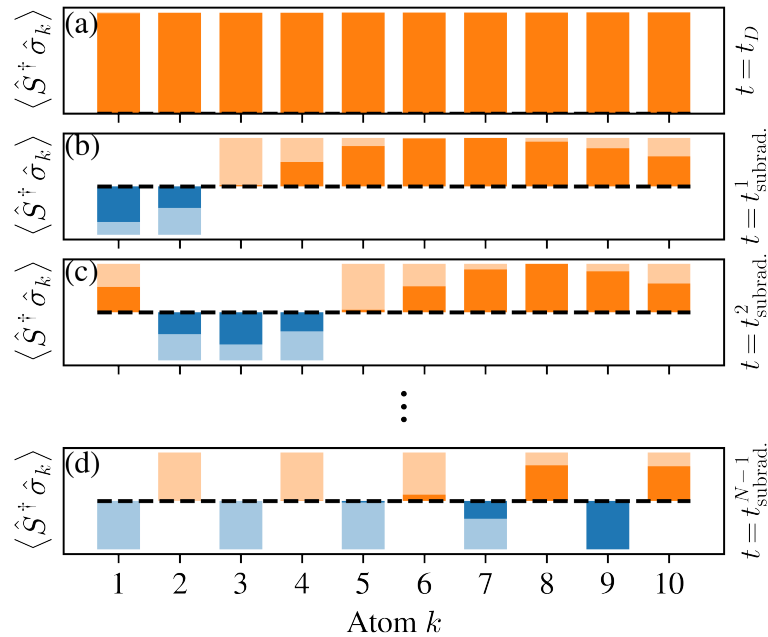


Figure 5.12: Dynamics of $\langle \hat{S}^\dagger \hat{\sigma}_k \rangle$ for an initially fully inverted ensemble. Positive and negative values are indicated in orange and blue, respectively. For clarity, the light-shaded bars indicate the sign of $\langle \hat{S}^\dagger \hat{\sigma}_k \rangle$. Panels (a)–(d) correspond to different times, which we indicate on the right-hand side of the plot. We simulate the dynamics of 10 atoms using the many-body master equation, assuming perfect state preparation and homogeneous coupling strengths. Note that the units are arbitrary.

state, see panels (b)–(d), we observe the same behavior that is predicted by the MCSA for pulse areas smaller than π . The ensemble first splits into two domains, then three, and so on. Finally, the last subradiant state features $N - 1$ domains. Each correlation, $\langle \hat{S}^\dagger \hat{\sigma}_k \rangle$, has the opposite sign of the correlation of the neighboring atoms, $\langle \hat{S}^\dagger \hat{\sigma}_{k\pm 1} \rangle$. It thus seems that the subsequent splitting in more and more domains described above is a universal feature of collective decay for unidirectional coupling. Understanding the origin of this dynamics is, therefore, an exciting prospect for both experimental and theoretical research on the subradiant dynamics in a cascaded quantum system.

5.7 Intermediate summary and conclusion

We have, for the first time, realized superradiant bursts in wQED. In particular, we observed that the peak power emitted into the forward-propagating mode scales even faster with the number of atoms than in the ideal Dicke case due to an increasingly

directed emission pattern, which is thus more efficiently collected by the nanofiber-guided mode. We explored the dynamics as a function of the pulse area of the excitation pulse and found that burst dynamics persists over a wide range of initial excitations. By measuring the first-order cross-correlation function between the superradiant burst and the excitation laser, we were able to directly identify two regimes of superradiant burst dynamics. In the first regime, the burst is seeded by an initial atomic coherence induced by the excitation laser. In the second regime of superfluorescence, the burst is seeded by vacuum fluctuations, i.e., it appears due to spontaneous synchronizations of the atomic dipoles. Finally, we discussed the subradiant dynamics following the initial superradiant decay. We found that the ensemble successively passes through $N - 1$ subradiant states. These states are characterized by the same atomic phase patterns, from weak excitation to full inversion.

In order to further study the late subradiant dynamics of the fully inverted state, it would be advantageous to excite the atoms using either a free-space laser beam or a nanofiber-guided beam that propagates in the opposite direction of the preferred direction of photon emission. Then, the effect of coherent forward scattering can be switched off since the excitation laser field does not imprint any phase pattern that constructively interferes in the forward direction. This could be implemented, e.g., by preparing atoms in the same ground state, $|6S_{1/2}, F = 4, m_F = -4\rangle$, but on the other side of the nanofiber. If one then excites the atoms to the $|6P_{3/2}, F = 5, m_F = -4\rangle$ state using a π -polarized laser field that propagates in the forward direction, the subsequent decay predominantly couples to the backward-propagating mode, with a directionality of $D = 0.68$, see section A.7 in the Appendix.

Here, we implemented almost unidirectional atom-waveguide coupling. However, one can also implement symmetric coupling by choosing an appropriate level scheme. E.g., one could prepare the atoms in $|6S_{1/2}, F = 4, m_F = 0\rangle$ via optical pumping and then coherently excite the atoms to $|6P_{3/2}, F = 5, m_F = 0\rangle$ using a π -polarized excitation laser field. The subsequent decay is then either σ^- , σ^+ , or π -polarized with branching ratios of $2/9$, $2/9$, and $5/9$, respectively, and the coupling is symmetric. However, one does not deal with a two-level system anymore, which makes the dynamics and its theoretical modeling much more complex. Still, it would be an interesting avenue for future research to investigate the differences between symmetric and asymmetric coupling. It has been recently proposed that superradiant bursts in wQED can give rise to an emergent chirality, i.e., the superradiant burst is either predominantly emitted into the forward- or backward direction [99]. One would then expect antibunching in the intensity-intensity cross-correlation function between forward- and backward-propagating modes. While this effect is most pronounced for symmetric coupling, it should also occur in the case of

directional atom-waveguide coupling.

Measuring the intensity-intensity correlation function of the superradiant burst itself is also an interesting prospect, which we currently investigate in our experiment. Initially, one expects bunching since the emission of the first photon into the waveguide increases the emission rate for the second photon [137]. The later dynamics is much more complicated and, to our knowledge, not yet well understood. In this context, it would be worthwhile to further study the subradiant dynamics of a fully inverted ensemble, which we have only briefly touched on in this thesis.

6 Observation of oscillatory Raman gain associated with two-photon Rabi oscillations

This chapter is based on Ref. [138]:

C. Liedl, S. Pucher, P. Schneeweiss, L. P. Yatsenko, and A. Rauschenbeutel. [Observation of oscillatory Raman gain associated with two-photon Rabi oscillations of nanofiber-coupled atoms](#). *J. Phys. B: At. Mol. Opt. Phys.*, 55(23):234005, 2022.

In the previous chapters, we assumed that the atomic dynamics is equivalent to the dynamics of a two-level system. However, the actual atomic level structure of cesium is much more complex. By a suitable choice of the initial atomic state, as well as the polarization and frequency of the driving fields, one can realize different level schemes using the same atomic species. In particular, three-level systems with a Λ -type level structure have played an important role in atomic and molecular physics. There, the excited state spontaneously decays into two different ground states. By driving the two respective transitions with suitable laser fields, one can control and manipulate the atomic ensemble, enabling the observation of a wealth of physical phenomena, like, e.g., electromagnetically induced transparency (EIT) [139], and slow light [140]. Moreover, three-level emitters find application in quantum information, where they can be used to construct quantum memories and quantum repeaters [141, 142].

Several techniques have been developed in order to control the populations and coherences of the two ground states. For example, stimulated Raman adiabatic passage (STIRAP) can be used to transfer population between the two ground states with almost unity efficiency [143]. Similar to a two-level system, one can also coherently drive the atoms with two suitable laser fields, leading to so-called two-photon Rabi oscillations between the two ground states of a Λ system[144].

In order to observe this effect, one typically exposes the atoms to two-photon Rabi pulses with varying pulse duration and subsequently measures the atomic populations [145, 146]. However, this method does not give access to the dynamics of the light fields. Two-photon

Rabi oscillations involve the coherent absorption of one driving field and the coherent emission into the mode of the other driving field. The corresponding energy difference between photons of the two driving fields is then transferred to (taken from) the atoms. The oscillation of the atomic population is therefore accompanied by oscillatory Raman gain and absorption of the two driving fields [138]. Raman gain and Raman lasing have been experimentally observed using cold atoms, both in the steady-state and in a transient regime [93, 147–150]. In order to observe oscillatory Raman gain, one has to maximize the optical density of the atomic ensemble. At the same time, the two-photon Rabi frequency has to be well-defined, meaning that all atoms have to be exposed to approximately the same light intensity. In experiments with free-space optics, these two requirements are challenging to meet simultaneously. In this context, coupling the atoms to a waveguide allows for both efficient and homogeneous atom-light coupling. This has facilitated what is, to our knowledge, the first observation of the oscillatory Raman gain and absorption associated with two-photon Rabi oscillations.

In the following, we will first present a theoretical model to describe the oscillatory Raman gain analytically. We then describe the experimental setting and the observation of Autler-Townes splitting in the transmission spectrum of a nanofiber-guided probe field, which allows us to precisely measure the Rabi frequency of a free-space laser field. Finally, we present the observation of the oscillatory Raman gain associated with two-photon Rabi oscillations and analyze the scaling of the two-photon Rabi frequency with the two-photon detuning and the power of one of the driving fields. Finally, we will briefly discuss the role of collective radiative effects in effective two-level systems.

6.1 Theoretical modeling

6.1.1 Three-level system

In this section, we describe the interaction between two classical laser fields with an ensemble of nanofiber-trapped cesium atoms. The relevant energy levels are schematically depicted in Fig. 6.1(a), where we have applied a magnetic offset field along the z -direction in order to stabilize the atomic spin states. The two ground states, $|a\rangle = |6S_{1/2}, F = 4, m_F = -4\rangle$ and $|b\rangle = |6S_{1/2}, F = 3, m_F = -3\rangle$, and the excited state, $|e\rangle = |6P_{3/2}, F = 4, m_F = -4\rangle$, constitute the Λ system, which we address optically in the following. The excited state, $|e\rangle$, radiatively decays with a rate $\Gamma = 2\pi \times 5.2$ MHz to the two ground states $|a\rangle$ and $|b\rangle$, with partial decay rates $\Gamma_{ea} = 5/12 \Gamma$ and $\Gamma_{eb} = 7/15 \Gamma$, respectively. Note that we neglect the decay to the dark state, $|c\rangle = |6S_{1/2}, F = 4, m_F = -3\rangle$, since the corresponding decay rate of $\Gamma_{ec} = 7/60 \Gamma \approx 0.1 \Gamma$ is quite small and does not

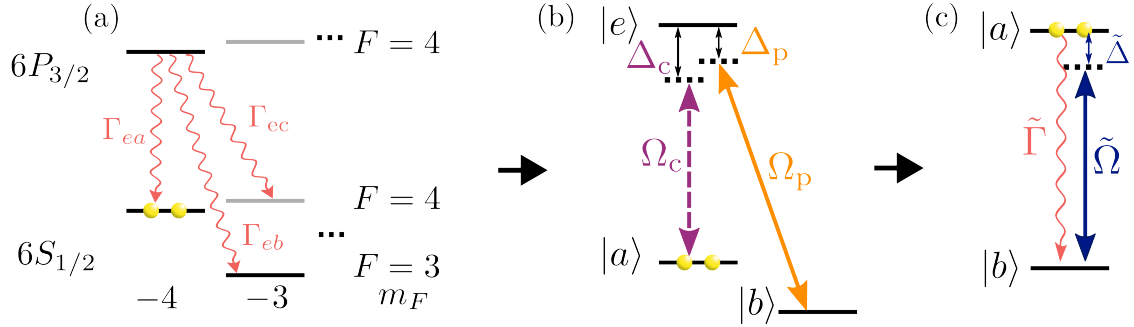


Figure 6.1: Illustration of the approximations we make to describe the atomic dynamics in our system. (a) Relevant cesium energy levels and partial decay rates for the decay from the excited state $|e\rangle = |6P_{3/2}, F = 4, m_F = -4\rangle$. The three levels comprising the relevant Λ system are indicated by the black lines. (b) By neglecting the levels shown as gray lines in (a), the system features a closed Λ configuration, which we drive with two laser fields. (c) By adiabatically eliminating the excited state, $|e\rangle$, we can describe the system as an effective two-level system. Here we assumed that $\Omega_p \ll \Omega_c$, and therefore neglect the effective decay from $|b\rangle$ to $|a\rangle$.

substantially alter the dynamics on the short time scales we are interested in here. We drive the atoms with a π -polarized coupling laser field and a σ^- -polarized probe laser field, which are near-resonant to the $|a\rangle \rightarrow |e\rangle$ - and $|b\rangle \rightarrow |e\rangle$ -transition, respectively, see Fig. 6.1(b). Due to polarization selection rules, we can also neglect the excited state $|6P_{3/2}, F = 4, m_F = -3\rangle$. We thus assume a closed system in Λ configuration, as depicted in (b). This means that we assume that the sum of the partial decay rates equals the total decay rate, $\Gamma_{ea} + \Gamma_{eb} = \Gamma$. The coupling laser field with Rabi frequency Ω_c is detuned by Δ_c from the $|a\rangle \rightarrow |e\rangle$ transition. The probe laser field with a Rabi frequency Ω_p is detuned by Δ_p from the $|b\rangle \rightarrow |e\rangle$ transition. We can then write down the standard Hamiltonian of a driven Λ system [151]:

$$\hat{\mathcal{H}} = -\hbar \frac{\Omega_p}{2} (\hat{\sigma}_{be} + \hat{\sigma}_{be}^\dagger) - \hbar \frac{\Omega_c}{2} (\hat{\sigma}_{ae} + \hat{\sigma}_{ae}^\dagger) - \hbar \Delta_p \hat{\sigma}_{ee}^\dagger \hat{\sigma}_{ee} - \hbar (\Delta_p - \Delta_c) \hat{\sigma}_{bb}^\dagger \hat{\sigma}_{bb}. \quad (6.1)$$

The first two terms describe the coherent drive of the atoms by the probe and coupling laser fields, where we have chosen both Rabi frequencies to be real. The operators $\sigma_{ij} = |i\rangle\langle j|$, where $i, j \in \{a, b, e\}$, describe the atomic annihilation and creation operators corresponding to the different transitions. The dynamics of the density matrix, $\hat{\rho}$, is then determined by the Lindblad master equation [103],

$$\frac{d\hat{\rho}}{dt} = -\frac{i}{\hbar} [\hat{\mathcal{H}}, \hat{\rho}] + \sum_{n=1}^2 \frac{1}{2} \left(2\hat{c}_n \hat{\rho} \hat{c}_n^\dagger - \hat{\rho} \hat{c}_n^\dagger \hat{c}_n - \hat{c}_n^\dagger \hat{c}_n \hat{\rho} \right), \quad (6.2)$$

where \hat{c}_n are the collapse operators describing spontaneous decay from the excited state, $|e\rangle$,

$$\hat{c}_1 = \sqrt{\Gamma_{ea}} \cdot \hat{\sigma}_{ae} \quad (6.3)$$

$$\hat{c}_2 = \sqrt{\Gamma_{eb}} \cdot \hat{\sigma}_{be}, \quad (6.4)$$

6.1.2 Adiabatic elimination

We could now numerically solve Eq. (6.2). However, in the specific parameter regime we are interested in, we are able to further simplify our model and will eventually obtain an analytical solution of the atomic dynamics. Here, we only describe the main steps and assumptions and refer to section A.8 in the Appendix for a more detailed derivation. Since we want to observe two-photon Rabi oscillations, we drive the system close to two-photon resonance with a large single-photon detuning, $\Delta_c \approx \Delta_p \gg \Gamma$. Therefore, the excited state is almost unpopulated, and we can neglect the time derivative of the optical coherences and populations of the excited state, i.e. $\dot{\rho}_{ae} = \dot{\rho}_{be} = \dot{\rho}_{ee} = 0$. This assumption is referred to as adiabatic elimination of the excited state [152] and is valid if the excited state population, ρ_{ee} , is very small, i.e.,

$$\Omega_p^2 \ll 4\Delta_p^2 + \Gamma^2, \quad (6.5)$$

$$\Omega_c^2 \ll 4\Delta_c^2 + \Gamma^2. \quad (6.6)$$

In this limit, the system dynamics is solely described by the differential equations for the matrix elements involving the two ground states. In addition, we will make the following assumptions.

- For simplicity, we assume that $\Gamma_{ea} = \Gamma_{eb} = \Gamma/2$.
- We assume that the probe field is much weaker than the coupling field, $\Omega_p \ll \Omega_c$.
- We assume that we have tuned the two laser fields to the light-shifted two-photon resonance, i.e., $\tilde{\Delta} = \Delta_p - \Delta_c + \frac{\Omega_c^2}{2\Delta_c} = 0$.

We are then left with the following differential equations,

$$\dot{\rho}_{aa} = -\tilde{\Gamma}\rho_{aa} - \frac{i}{2}\tilde{\Omega}(\rho_{ba} - \rho_{ab}), \quad (6.7)$$

$$\dot{\rho}_{ab} = -\frac{i}{2}\tilde{\Omega}(\rho_{bb} - \rho_{aa}) - \tilde{\Gamma}\rho_{ab}, \quad (6.8)$$

which are qualitatively equivalent to the optical Bloch equations for a two-level atom. Therefore, a driven three-level system, for which adiabatic elimination is justified, is also

referred to as an effective two-level system [152]. Here, we have introduced an effective Rabi frequency, $\tilde{\Omega}$, an effective detuning $\tilde{\Delta}$, and an effective decay rate, $\tilde{\Gamma}$,

$$\tilde{\Omega} = \frac{\Omega_p \Omega_c}{2\tilde{\Delta}}, \quad (6.9)$$

$$\tilde{\Gamma} = \frac{\Omega_c^2 \Gamma}{8\tilde{\Delta}^2}. \quad (6.10)$$

The effective two-level system and the effective quantities are schematically depicted in Fig. 6.1(c). Here, the ground state, $|a\rangle$, is equivalent to the excited state in a usual two-level atom, which decays to the ground state, $|b\rangle$, with the rate $\tilde{\Gamma}$. The underlying process of this effective decay is off-resonant one-photon scattering of the coupling laser field, which populates the excited state, $|e\rangle$, which subsequently decays to the ground state, $|b\rangle$. $\tilde{\Delta}$ denotes the detuning from the light-shifted two-photon resonance. Since we are interested in resonant, two-photon Rabi oscillations, we will set $\tilde{\Delta} = 0$ in the following. Importantly, there is one major difference compared to a real two-level atom. The population in Eq. (6.7) decays with the same rate, $\tilde{\Gamma}$, as the coherence in Eq. (6.8). In contrast, in the usual closed two-level system, the coherence decays with half the decay rate of the excited state population. The additional decoherence channel in the effective two-level system can be attributed to a transition from $|a\rangle$ to the excited state, $|e\rangle$, and subsequent decay back into the initial state, $|a\rangle$. This process does not affect the atomic populations but results in additional decoherence.

6.1.3 Analytical solution and probe transmission

In the experiment, we initially prepare the atoms in $|a\rangle$, such that the initial conditions for solving Eqs. (6.7) and (6.8) are $\rho_{aa}(t=0) = 1$ and $\rho_{ab}(t=0) = 0$, respectively. We then solve the optical Bloch equations for the effective two-level system analytically and express the solutions in terms of the two components of the Bloch vector, the inversion, $w = \rho_{aa} - \rho_{bb}$, and twice the imaginary part of the coherence, $v = 2\Im(\rho_{ab})$,

$$v(t) = \frac{\tilde{\Gamma}\tilde{\Omega}}{\tilde{\Gamma}^2 + \tilde{\Omega}^2} \left[1 - e^{-\tilde{\Gamma}t} \left(\cos \tilde{\Omega}t + \frac{2\tilde{\Gamma}^2 + \tilde{\Omega}^2}{\tilde{\Omega}\tilde{\Gamma}} \sin \tilde{\Omega}t \right) \right], \quad (6.11)$$

$$w(t) = \frac{\tilde{\Gamma}^2}{\tilde{\Gamma}^2 + \tilde{\Omega}^2} \left[1 + e^{-\tilde{\Gamma}t} \left(\frac{2\tilde{\Gamma}^2 + \tilde{\Omega}^2}{\tilde{\Gamma}^2} \cos \tilde{\Omega}t - \frac{\tilde{\Omega}}{\tilde{\Gamma}} \sin \tilde{\Omega}t \right) \right]. \quad (6.12)$$

Since the coherently absorbed (emitted) power is proportional to the optical coherence created by the probe field, $v(t)$, and the optical depth on the light-shifted two-photon

resonance, \widetilde{OD} , we can write the probe power transmission coefficient as

$$T_{\text{probe}} = \exp \left[-A \widetilde{OD} v(t) \right]. \quad (6.13)$$

To find the factor A , we use the fact that the optical depth on the two-photon resonance, \widetilde{OD} is defined in the steady state, and for vanishing probe power,

$$\widetilde{OD} = -\log \left[\lim_{\tilde{\Omega} \rightarrow 0} \lim_{t \rightarrow \infty} T_{\text{probe}} \right] = A \widetilde{OD} \lim_{\tilde{\Omega} \rightarrow 0} \lim_{t \rightarrow \infty} v(t) = A \widetilde{OD} \frac{\tilde{\Gamma}}{\tilde{\Omega}}. \quad (6.14)$$

Thus, we find that $A = \tilde{\Gamma}/\tilde{\Omega}$ and can therefore write,

$$T_{\text{probe}} = \exp \left[-\widetilde{OD} \frac{\tilde{\Gamma}}{\tilde{\Omega}} v(t) \right]. \quad (6.15)$$

The optical depth on the two-photon resonance, \widetilde{OD} , is related to the optical depth on the one-photon resonance, OD , via the ratio of the (effective) decay rates,

$$\widetilde{OD} = \frac{\tilde{\Gamma}}{\Gamma} OD = \frac{\Omega_c^2}{8\Delta^2} OD \quad (6.16)$$

6.2 Experimental setting

In our experiment, we want to measure the modulation of the probe field that results from two-photon Rabi oscillations of the atomic ensemble. Therefore, we use a fiber-guided probe laser field to maximize the atom-light coupling strength. It is locally σ^- -polarized at the position of the atoms, as in chapters 4 and 5. For all measurements presented in this chapter, we record time traces of the power transmitted through the nanofiber using two SPCMs, see detection setup in section 2.4. For the coupling field, we use a free-space laser beam propagating in the $+x$ -direction, see Fig. 6.2(a). We set its polarization to be linear along z , i.e., π -polarization. We apply a magnetic offset field of about 5 G along the z -direction to stabilize the atomic spin state. In order to tune the two laser fields to the correct frequencies, we stabilize the coupling laser frequency using saturation absorption spectroscopy of a cesium vapor cell. To maximize the relative phase stability between the probe and coupling laser fields, we optically lock the phase of the probe laser field to that of the coupling laser field, with a frequency offset that corresponds to the hyperfine splitting of about $2\pi \times 9.2$ GHz. Both laser frequencies can be tuned individually using acousto-optical modulators.

In order to calculate the Rabi frequency of the free-space coupling laser field, one has to estimate the local intensity and polarization of the coupling field at the position of the

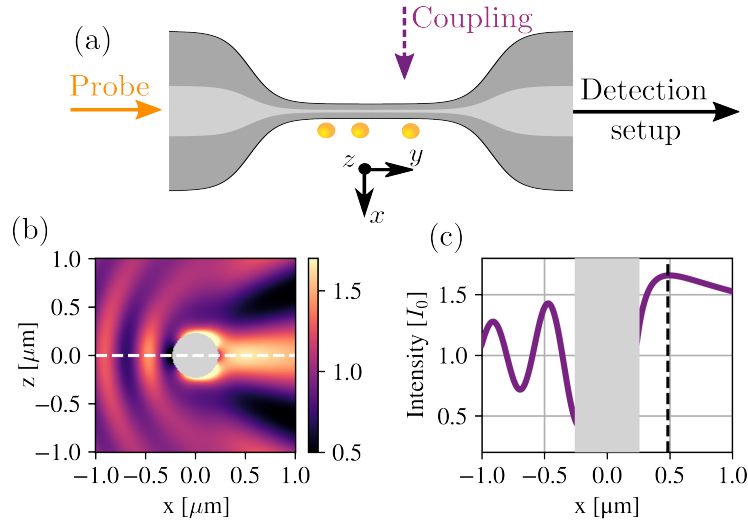


Figure 6.2: (a) We expose the atoms to a fiber-guided probe field propagating in the $+y$ -direction and a free space coupling laser field propagating in the $+x$ -direction. (b) and (c) Calculated coupling laser field scattered by the nanofiber, assuming an incident plane wave with a linear polarization along z . (b) Intensity distribution in the $x - z$ plane. The nanofiber cross-section is indicated in gray. (c) Intensity along the white dashed line shown in (b). The location of the trapped atoms is indicated by the black dashed vertical line.

atoms. Since the atoms are trapped only a few hundred nanometers from the nanofiber surface, scattering by the nanofiber has to be taken into account. To do so, we assume an incident plane wave with intensity I_0 that propagates in the $+x$ -direction and is linearly polarized along z . We then use the analytical solution for the scattering of a plane wave by an infinitely long cylinder to compute the intensity distribution of the scattered field around the nanofiber, see Fig. 6.2(b) and (c) [153]. In (c), we show a cut through the intensity distribution along x for $z = 0$. For $x < 0$, we observe an intensity modulation, since the reflected light from the nanofiber surface interferes with the incident field to create a standing wave pattern. Behind the fiber ($x > 0$), the light is focused by the cylindrical nanofiber and the intensity features a maximum of about $1.7 I_0$. The location of the maximal intensity almost coincides with the location of the trapped atoms, which is indicated by the black dashed line. Since the intensity gradient is smallest behind the nanofiber, it is beneficial to illuminate the atoms through the fiber. In this configuration, the intensity seen by the atoms is more homogeneous. Using the analytical solution for the scattered field, we also checked that the scattered field in the trapping region stays almost perfectly π -polarized [82].

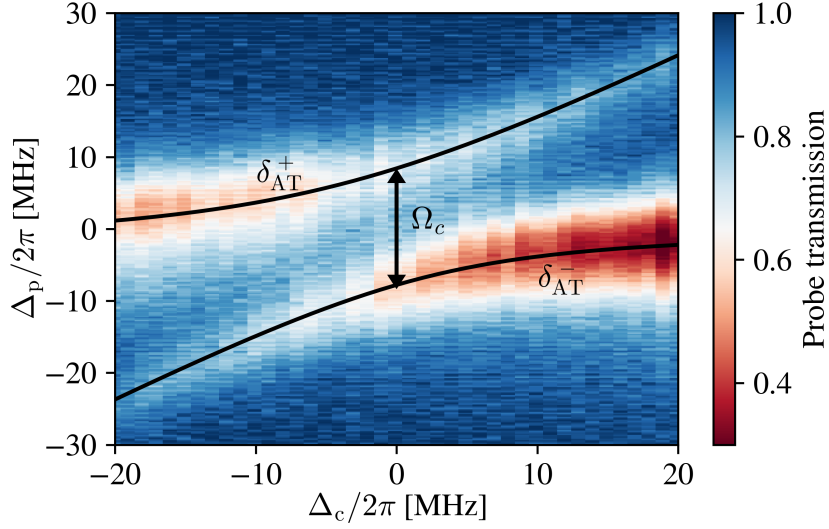


Figure 6.3: Probe transmission spectra for different coupling laser detunings, Δ_c . Autler-Townes splitting of the resonance leads to an avoided crossing, where the splitting on resonance is given by the Rabi frequency of the coupling laser field, Ω_c . The black solid lines indicate the Autler-Townes shift for a fitted Rabi frequency of $\Omega_c = 2\pi \times 16.1(1)$ MHz, indicated by the black double arrow.

6.3 Autler-Townes splitting

In the above calculation of the field scattered by the nanofiber, we assumed an incident plane wave. However, in the experiment, the coupling laser field features a Gaussian intensity profile. While the corresponding Gaussian waist of about 4 mm is much larger than the extent of the nanofiber-trapped atomic ensemble (about 1 mm), the finite waist could lead to deviations from the calculated local intensity. Furthermore, both the polarization and the intensity of the coupling laser field can be modified due to other experimental imperfections, e.g., a non-zero angle of incidence, absorption, and birefringence of the windows of the vacuum chamber. In order to directly measure the Rabi frequency of the coupling laser field, Ω_c , we make use of the Autler-Townes effect [154–156]. There, the strong driving of the atoms by the coupling laser field mixes the bare eigenstates of the Λ system. The new eigenstates, the so-called dressed states, are then split and shifted from the $|g\rangle \rightarrow |e\rangle$ transition frequency by

$$\delta_{\text{AT}}^{\pm} = \frac{1}{2} \left(\Delta_c \pm \sqrt{\Omega_c^2 + \Delta_c^2} \right). \quad (6.17)$$

Thus, the Rabi frequency, Ω_c , can be inferred from the Autler-Townes splitting for zero detuning, $\Delta_c = 0$. In order to measure this splitting, we first turn on the coupling laser field for 0.1 ms, such that almost all atoms are optically pumped to state $|b\rangle$. Then, we additionally turn on a weak probe field, with a saturation parameter of about 0.1, and scan its detuning, Δ_p , over the resonance in about 700 μs . From the transmitted power and a reference measurement without atoms, we then infer the transmission spectrum. In Fig. 6.3, we show the probe transmission spectra for different coupling laser detunings as a colormap. We clearly observe an avoided crossing, which is characteristic for the Autler-Townes effect. We note that we observe an asymmetry in the depth of the transmission dips for large Δ_c . This effect is likely caused by the direction of the frequency ramp: Since we sweep from negative to positive Δ_p , and resonant probing leads to recoil heating, the atom number is slightly reduced during the sweep, leading to a shallower transmission dip. We then fit each individual transmission spectrum to a double Lorentzian line shape and extract the frequency splitting between the two respective resonances as a function of the coupling laser detuning, Δ_c . We then fit the resulting data using the equation for the Autler-Townes splitting

$$\delta_{\text{AT}}^+ - \delta_{\text{AT}}^- = \sqrt{\Omega_c^2 + \Delta_c^2}, \quad (6.18)$$

which yields a coupling laser Rabi frequency of $\Omega_c = 2\pi \times 16.1(1)$ MHz. When estimating the local intensity from the power and diameter of the coupling laser field, we obtain $\Omega_c = 2\pi \times 11.9(2)$ MHz. When taking into account the focusing effect of the nanofiber, this calculated value increases to $\Omega_c = 2\pi \times 15.4(3)$ MHz, which is in reasonable agreement with the value extracted from our measurements. It is thus indeed important to take into account the intensity pattern around the nanofiber. In the following, we use the measured Rabi frequency of the coupling field as a calibration value to infer the Rabi frequency for any given power of the coupling laser field.

6.4 Observation of oscillatory Raman gain

In Fig. 6.3, we observe that one of the resonances converges to $\Delta_p \approx \Delta_c$ for large detunings, Δ_c . This resonance is the light-shifted two-photon resonance, i.e., where the detuning in the effective two-level system is zero, $\tilde{\Delta} = \Delta_p - \delta_{\text{AT}}^\pm = 0$. In the following, we tune the probe laser field to this light-shifted two-photon resonance. To fulfill the requirements of adiabatic elimination, the single-photon scattering rates of the two laser fields have to be small compared to the excited state decay rate, Γ , see Eq. 6.6.

For the coupling laser field, we chose a detuning of $\Delta_c = -2\pi \times 32.5(3)$ MHz and a Rabi frequency of $\Omega_c = 2\pi \times 28.2$ MHz. For these parameters, we can now check whether the

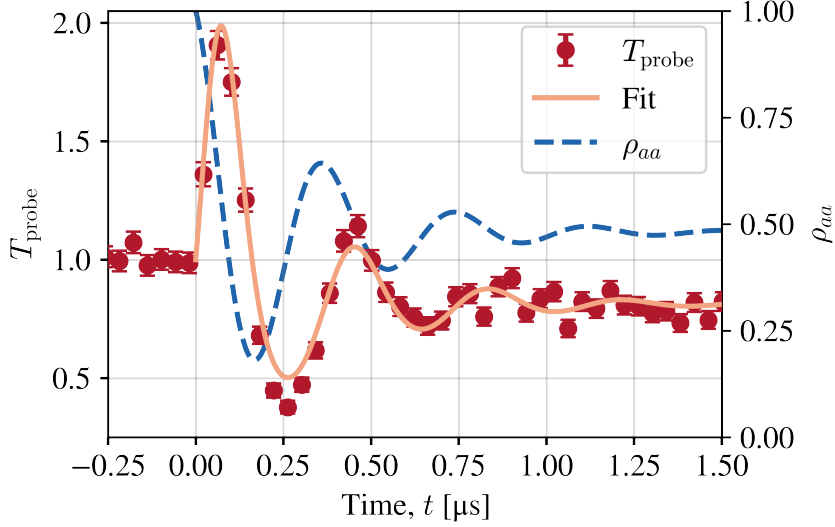


Figure 6.4: Measured probe transmission coefficient as a function of time after switching on the coupling field at time $t = 0 \mu\text{s}$. We observe the oscillatory Raman gain that is associated with two-photon Rabi oscillations of the atoms. We fit the data using the analytical expression for the probe transmission, see orange solid line. Using the fit results, we also show the corresponding average population in $|a\rangle$, given by ρ_{aa} as the dashed blue line.

coupling laser field fulfills the criterion for adiabatic elimination, see Eq. (6.6). We get $\Omega_c^2/(4\Delta_c^2 + \Gamma^2) = 0.19$, which is substantially smaller than one. Thus, the condition for adiabatic elimination is fulfilled for the coupling laser field.

In order to maximize the modulation of the probe transmission due to two-photon Rabi oscillations, the probe laser Rabi frequency, Ω_p , should be as small as possible. However, a minimal requirement for observing Rabi oscillations is that the oscillation frequency is faster than the effective decay rate, $\tilde{\Omega} > \tilde{\Gamma}$. For our effective two-level system, this condition can be written as

$$\Omega_p > \frac{\Omega_c \Gamma}{4\Delta_c}, \quad (6.19)$$

where we have used the definitions of $\tilde{\Omega}$ and $\tilde{\Gamma}$, see Eqs. (6.9) and (6.10), respectively. For our parameters, this condition gives $\Omega_p > 2\pi \times 1.1 \text{ MHz}$. In order to calculate the probe Rabi frequency, we can use Eq. (4.5), with an extra factor of $\sqrt{5/12}$ to account for the branching ratio of the probe transition,

$$\Omega_p = \sqrt{\frac{5}{12} \frac{4\beta_f \Gamma P_p}{\hbar \omega_p}}, \quad (6.20)$$

where ω_p is the optical frequency of the probe field, and P_p is the probe input power. In order to increase the atom-light coupling strength, β_f , we adiabatically ramp the red trapping power from 2.4 mW to 2.8 mW in 100 μs shortly before the probing. This moves the location of the trapping minima closer to the nanofiber surface, resulting in an increased coupling strength. From the increase of the optical density on the D2 cycling transition, we infer a coupling strength of $\beta_f = 0.015$, which corresponds to a roughly 40 % increase compared to our standard trapping configuration. We choose a probe input power of $P_p \approx 480$ pW, which corresponds to a Rabi frequency of $\Omega_p = 2\pi \times 6.5$ MHz, i.e., about six times larger than the minimum value to observe two-photon Rabi oscillations for our parameters, see above. At the same time, $\Omega_p^2/\Omega_c^2 \approx 0.05 \ll 1$, justifying that we neglected the effective decay rate from $|b\rangle \rightarrow |a\rangle$ in our modeling. Now that we have identified an experimental setting for which we can expect to observe oscillatory Raman gain and absorption, let us turn to the experimental realization.

First, we only switch on the probe laser field for 200 μs . We observe a transmission coefficient of one since the probe laser field does not couple to the about 700 trapped atoms in the initial state, $|a\rangle$. At the time, $t = 0$ μs , we then also switch on the coupling laser field and plot the resulting dynamics of the probe transmission coefficient in Fig. 6.4. Initially, the atoms are prepared in state $|a\rangle$, which corresponds to full inversion of the effective two-level system, see Fig. 6.1(c). Therefore, the probe transmission increases first and the probe field experiences a Raman gain of up to about 2. Then, the transmission oscillates between Raman gain and Raman absorption. This dynamics can be understood as a coherent exchange of photons between the probe and the coupling laser fields. As the atoms are transferred from $|a\rangle$ to $|b\rangle$, photons in the coupling laser field are coherently scattered into the probe laser field, which therefore experiences gain. For the reverse process, photons are coherently scattered from the probe laser field into the coupling laser field, such that the probe field experiences coherent absorption. Two-photon Rabi oscillations between $|a\rangle$ and $|b\rangle$ therefore manifest as oscillatory Raman gain and absorption in the probe field. If we would monitor the transmission of the coupling laser field at the same time, we would also expect oscillatory Raman gain and absorption. However, the oscillation would be π out of phase with the oscillations of the probe transmission coefficient. After about two oscillation periods, the system reaches a steady state.

We fit the analytical solution for the probe transmission coefficient to our data, see Eq. (6.15), where we use $\tilde{\Omega}$, $\tilde{\Gamma}$ and \widetilde{OD} as fit parameters. Our model fits well to the experimental data, and we extract a two-photon Rabi frequency of $\tilde{\Omega} = 2\pi \times 2.63(3)$ MHz, which is in reasonable agreement with our estimate based on independently calibrated parameters, $\tilde{\Omega} = 2\pi \times 2.83(3)$ MHz. Also the fitted value for the effective decay rate, $\tilde{\Gamma} = 2\pi \times 516(21)$ kHz is in good agreement with the expected value, $\tilde{\Gamma} = 2\pi \times 490$ kHz.

Since the effective decay rate is given by the rate of spontaneous emission from the excited state, $|e\rangle$, we can assume that $\tilde{\Gamma} = \Gamma\rho_{ee}$. From this relation, we infer an average excited state probability of $\rho_{ee} = 0.100(1) \ll 1$, confirming that adiabatic elimination is appropriate in our parameter regime. For the optical depth on the light-shifted two-photon resonance, we obtain $\widetilde{OD} = 5.6(2)$. This is in good agreement with the expected value of 5.5, see Eq. (6.16).

Finally, we use the fit results to calculate the average population in $|a\rangle$, given by ρ_{aa} , and plot it as the dashed red line in Fig. 6.4. As expected for two-photon Rabi oscillations, ρ_{aa} features damped oscillations, reaching a steady state value of 0.481(4). The oscillation is 90° out of phase with the oscillation of the probe transmission coefficient. This can be understood by considering Rabi oscillations in the (hypothetical) perfectly coherent case, i.e., $\tilde{\Gamma} = 0$. There, the atomic coherence is proportional to the time derivative of the population in the effective excited state, $v(t) \sim \dot{\rho}_{aa}(t)$, see Eq. 6.8. Therefore, if ρ_{aa} features sinusoidal (Rabi) oscillations, its derivative, and thus, $v(t)$, features oscillations with the same frequency but with a phase shift of 90° . The associated modification of the power of the light field is quantified by the transmission coefficient, T_{probe} , which is determined by the coherence, $v(t)$, see Eq. (6.15). Therefore, the oscillations of T_{probe} are also 90° out of phase with the oscillations of population, ρ_{aa} .

More intuitively, one can understand the fact that T_{probe} is related to the time derivative of ρ_{aa} as follows: ρ_{aa} is a measure of the energy stored in the atoms. Its derivative thus indicates how fast the atoms lose (gain) energy by coherently emitting (absorbing) photons into (from) the guided mode.

6.4.1 Scaling with probe power and detuning

To further consolidate our hypothesis that the observed oscillatory Raman gain results from two-photon Rabi oscillations, we repeat our measurement for different detunings, $\tilde{\Delta}$, and probe powers, P_p . In Fig. 6.5(a), we show the fitted two-photon Rabi frequency as a function of the detuning from the light-shifted two-photon resonance, $\tilde{\Delta}$. For a finite detuning, $\tilde{\Delta}$, the oscillation frequency is determined by the generalized Rabi frequency, $\tilde{\Omega}_g = (\tilde{\Omega}^2 + \tilde{\Delta}^2)^{1/2}$ [157]. Indeed, our data fits well to this expression for an on-resonance Rabi frequency of $\tilde{\Omega} = 2\pi \times 2.12(4)$ MHz, see green solid line. This is in reasonable agreement with the estimated Rabi frequency of $\tilde{\Omega} = 2\pi \times 2.0(2)$ MHz for the slightly different probe power used in this measurement.

Finally, we show the dependence of the resonant Rabi frequency, $\tilde{\Omega}$, on the probe power, P_p , in Fig. 6.5(b). Recalling the expressions for the two-photon Rabi frequency and the Rabi frequency of the probe field, Eqs. (6.9) and (6.20), respectively, we expect the

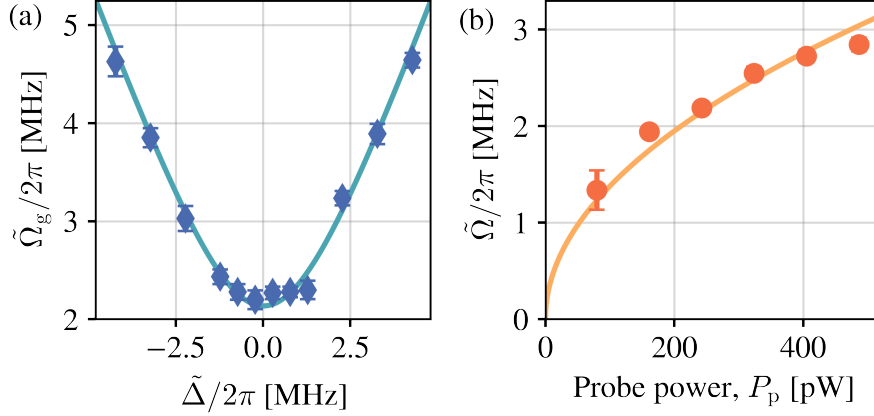


Figure 6.5: Scaling of the oscillation frequency of the probe transmission coefficient. (a) For finite detuning, the oscillation frequency is determined by the generalized Rabi frequency, $\tilde{\Omega}_g$, which increases with the detuning, $\tilde{\Delta}$. (b) The resonant Rabi frequency, $\tilde{\Omega}$, increases with the square root of the probe power, P_p .

following scaling with the probe power, P_p ,

$$\tilde{\Omega} = A\sqrt{P_p} = \frac{\Omega_c}{2\Delta_c} \sqrt{\frac{5}{12} \frac{4\beta_f\Gamma}{\hbar\omega_p}} \sqrt{P_p}. \quad (6.21)$$

Indeed, the data in (b) fits well to a square root function, and we obtain a fitted amplitude of $A = 2\pi \times 138(3)\text{kHz}/\sqrt{\text{pW}}$, see orange solid line in (b). Using Eq. (6.21) and our independent calibrations of Ω_c and Δ_c , we can then extract the atom-light coupling strength, $\beta_f = 0.0171(8)$ from the fitted amplitude, A . This is in reasonable agreement with our expectation, given the increased red trapping power in this measurement.

6.5 Intermediate summary and conclusion

We have experimentally studied the temporal dynamics of an ensemble of driven three-level systems in Λ configuration, which are coupled to an optical nanofiber. By far-off-resonantly driving the atoms, we were able to realize an effective two-level system in which the excited state can be adiabatically eliminated. In this setting, we observed oscillatory Raman gain and absorption. This dynamics is the manifestation of two-photon Rabi oscillations in the driving field. The fact that the fitted values for $\tilde{\Omega}$ and $\tilde{\Gamma}$ are so close to the expected values is evidence that the approximations that we made in our model are justified. This is not obvious since there are several effects that we neglect in our modeling. First, we do not include temperature-induced fluctuations of the coupling strength, β_f , as it was

necessary when modeling the data presented in chapters 4 and 5. This effect leads to an inhomogeneous broadening of the two-photon Rabi frequency, leading to additional dephasing. Second, we assume that the dynamics of the entire ensemble can be described by the dynamics of a single atom with a large, effective optical depth, i.e., we neglect any collective effects. The latter could be modeled by the cascaded interaction models described in sections 3.3 and 3.4, adapted for three-level atoms. However, as we have seen in section 4.1, the strongly driven dynamics is not substantially altered by collective effects.

It would be an interesting avenue for further research to study the superradiant decay dynamics in an effective two-level system. In order to do so, one would simply turn off the probe laser field. The system is then effectively equivalent to a fully inverted ensemble of two-level atoms. As we have seen in chapter 5, the decay dynamics of such a system can feature superradiant burst dynamics. Indeed, so-called Raman superradiance has been observed in BECs and thermal vapors [17, 20, 158]. It can be advantageous to use an effective two-level system since one can perfectly invert the ensemble by simply preparing atoms in state $|a\rangle$ via optical pumping and then switch on the effective decay rate by turning on the coupling laser field. One could also prepare atoms in different m_F -states of the $F = 4$ ground state manifold, thereby controlling the directionality of the photon emission. In addition, one can tune the effective decay rate, $\tilde{\Gamma}$, via the detuning and Rabi frequency of the coupling laser field. This would change the timescale of the superradiant burst dynamics, relaxing the required temporal resolution of the detectors. However, the effective optical depth is much smaller than for a one-photon transition. Therefore, one would likely need many more atoms to surpass the critical threshold atom number, beyond which superradiant burst dynamics appears.

7 Conclusion and perspectives

We have experimentally explored collective radiative dynamics in waveguide quantum electrodynamics (wQED). In particular, we demonstrated the coherent excitation of nanofiber-coupled atomic ensembles using guided optical pulses. This technique allowed us to explore the collective decay dynamics for a wide range of initial excitations, from the weak excitation regime to full inversion. By unidirectionally coupling the atoms to the guided modes of an optical nanofiber, we implemented a cascaded quantum system. We introduced two new models that are based on the cascaded interaction between the atoms to accurately describe the dynamics in our system. We showed that many of the collective radiative effects known to occur in the Dicke regime can also be observed in wQED systems. There, the requirement of tight confinement is relaxed, making wQED an excellent testbed for studying the fundamental mechanisms underlying sub- and superradiance. Moreover, the possibility of tuning the directionality of the atom-waveguide coupling provides a new tool for tailoring collective radiation. Finally, we realized an ensemble of effective two-level atoms by driving two-photon Rabi oscillations between the two ground states in a Λ system. We observed this effect dynamically by measuring oscillatory Raman gain and absorption of a nanofiber-guided laser field.

Beyond the effects studied in this thesis, interesting avenues for future research open up. It has been predicted that the light emitted as a superradiant burst can feature a large overlap with a multi-photon Fock state [59]. To make use of the excellent metrological properties of these photonic states, it would in principle be advantageous to implement unidirectional coupling, as the light would then be emitted into a single, well-defined mode. In this context, a first step towards characterizing the photonic state of the collectively emitted light would be to measure the second-order autocorrelation function of the superfluorescent light.

It is an open question how directional atom-waveguide coupling influences the properties of this photonic state. In particular, the emergence of subradiant states seems to be a universal feature of collective emission in a cascaded quantum system. However, it is not yet clear how to quantitatively model this subradiant dynamics for hundreds of atoms since higher-order correlations between the atoms are expected to play an important role for a fully inverted ensemble [159]. The study of subradiance in a cascaded quantum

system is thus an interesting avenue for both experimental and theoretical research.

A dynamical symmetry breaking due to the emission of a superradiant burst in wQED has been proposed, leading to an emergent chirality [99]. We expect this effect to manifest as antibunching in the second-order cross-correlation function between the forward- and backward-emitted light. Measuring this effect is well within reach of our current experimental capabilities. It is expected to be most pronounced for symmetric atom-waveguide coupling, which could also be implemented in our experiment.

For many of the above-described effects, it might be advantageous to work with an effective two-level system, i.e., a Λ system driven on a light-shifted two-photon resonance. There, one can prepare the fully inverted state perfectly via optical pumping. In addition, one can modify the effective decay rate by suitably choosing the detuning and power of the coupling laser field. First results on Raman superradiant bursts in wQED have recently been obtained [160].

It would also be intriguing to lift the axial confinement of the nanofiber-based dipole trap. One could then study the motional dynamics of the ensemble due to the recoil induced by superradiant emission into the guided modes. Since collective effects in a cascaded quantum system build up along the ensemble, this recoil could result in a compression of the atomic ensemble. Imaging of a nanofiber-trapped ensemble, even of single atoms, has already been demonstrated in our setup [91], making the observation of such a dissipation-induced compression, in principle, feasible.

While here, we have investigated collective radiation of waveguide-coupled atomic ensembles in a pulsed regime, one can also expose the atoms to a continuous-wave driving field in order to study the steady-state properties of the system. For example, we could study the influence of directional coupling on superradiant phase transitions [123]. Moreover, it would be interesting to explore photon transport in continuously driven ensembles of effective two-level system. There, the effective decay rate can be tuned, which may be beneficial for applications such as single-photon sources and squeezed light [161–163].

Finally, many protocols in wQED rely on an almost unity atom-waveguide coupling strength. This could possibly be realized by coupling so-called Rydberg superatoms to a nanofiber-guided mode [164]. Reaching near-unity coupling with many emitters would be a transformative milestone for wQED, paving the way towards generating complex quantum states of light as a resource for quantum technologies [56, 57, 59, 60, 165]. Moreover, it has been predicted that a driven dissipative cascaded quantum system can evolve into a pure atomic many-body state, which may also feature multi-partite entanglement [166–168].

Bibliography

- [1] S. Haroche. [Nobel lecture: Controlling photons in a box and exploring the quantum to classical boundary](#). *Rev. Mod. Phys.*, 85(3):1083, 2013. 1
- [2] D. J. Wineland. [Nobel lecture: Superposition, entanglement, and raising Schrödinger's cat](#). *Rev. Mod. Phys.*, 85(3):1103, 2013. 1
- [3] C. D. Bruzewicz, J. Chiaverini, R. McConnell, and J. M. Sage. [Trapped-ion quantum computing: Progress and challenges](#). *Appl. Phys. Rev.*, 6(2):021314, 2019. 1
- [4] L. Henriet, L. Beguin, A. Signoles, T. Lahaye, A. Browaeys, G.-O. Reymond, and C. Jurczak. [Quantum computing with neutral atoms](#). *Quantum*, 4:327, 2020. 1
- [5] H. J. Kimble. [The quantum internet](#). *Nature*, 453(7198):1023, 2008. 1
- [6] S. Wehner, D. Elkouss, and R. Hanson. [Quantum internet: A vision for the road ahead](#). *Science*, 362(6412):eaam9288, 2018. 1
- [7] C. L. Degen, F. Reinhard, and P. Cappellaro. [Quantum sensing](#). *Rev. Mod. Phys.*, 89(3):035002, 2017. 1
- [8] C. Gross and I. Bloch. [Quantum simulations with ultracold atoms in optical lattices](#). *Science*, 357(6355):995, 2017. 1, 2
- [9] R. H. Dicke. [Coherence in spontaneous radiation processes](#). *Phys. Rev.*, 93(1):99, 1954. 1, 24, 25, 66
- [10] M. Gross and S. Haroche. [Superradiance: An essay on the theory of collective spontaneous emission](#). *Phys. Rep.*, 93(5):301, 1982. 1, 24, 25, 28
- [11] M. G. Benedict, A. M. Ermolaev, V. Malyshev, I. Sokolov, and D. Trifonov, Evgenii. [Super-radiance: Multiatomic coherent emission](#). *CRC Press*, 2018. 1
- [12] N. Skribanowitz, I. Herman, J. MacGillivray, and M. Feld. [Observation of Dicke superradiance in optically pumped HF gas](#). *Phys. Rev. Lett.*, 30(8):309, 1973. 1, 2

- [13] H. J. Metcalf and P. Van der Straten. [Laser cooling and trapping of neutral atoms](#). *The Optics Encyclopedia: Basic Foundations and Practical Applications*, 2007. 2
- [14] M. Gross, P. Goy, C. Fabre, S. Haroche, and J. Raimond. [Maser oscillation and microwave superradiance in small systems of Rydberg atoms](#). *Phys. Rev. Lett.*, 43(5):343, 1979. 2
- [15] D. D. Grimes, S. L. Coy, T. J. Barnum, Y. Zhou, S. F. Yelin, and R. W. Field. [Direct single-shot observation of millimeter-wave superradiance in Rydberg–Rydberg transitions](#). *Phys. Rev. A*, 95(4):043818, 2017. 2, 66
- [16] S. Inouye, A. Chikkatur, D. Stamper-Kurn, J. Stenger, D. Pritchard, and W. Ketterle. [Superradiant Rayleigh scattering from a Bose-Einstein condensate](#). *Science*, 285(5427):571, 1999. 2
- [17] D. Schneble, G. K. Campbell, E. W. Streed, M. Boyd, D. E. Pritchard, and W. Ketterle. [Raman amplification of matter waves](#). *Phys. Rev. A*, 69(4):041601, 2004. 2, 96
- [18] Y. Kaluzny, P. Goy, M. Gross, J. Raimond, and S. Haroche. [Observation of self-induced Rabi oscillations in two-level atoms excited inside a resonant cavity: the ringing regime of superradiance](#). *Phys. Rev. Lett.*, 51(13):1175, 1983. 2
- [19] M. A. Norcia, M. N. Winchester, J. R. Cline, and J. K. Thompson. [Superradiance on the millihertz linewidth strontium clock transition](#). *Science Adv.*, 2(10):e1601231, 2016.
- [20] Y. Yoshikawa, T. Sugiura, Y. Torii, and T. Kuga. [Observation of superradiant Raman scattering in a Bose-Einstein condensate](#). *Phys. Rev. A*, 69(4):041603, 2004. 2, 96
- [21] R. DeVoe and R. Brewer. [Observation of superradiant and subradiant spontaneous emission of two trapped ions](#). *Phys. Rev. Lett.*, 76(12):2049, 1996. 2
- [22] G. Ferioli, A. Glicenstein, F. Robicheaux, R. T. Sutherland, A. Browaeys, and I. Ferrier-Barbut. [Laser-driven superradiant ensembles of two-level atoms near Dicke regime](#). *Phys. Rev. Lett.*, 127(24):243602, 2021. 2
- [23] A. Glicenstein, G. Ferioli, A. Browaeys, and I. Ferrier-Barbut. [From superradiance to subradiance: exploring the many-body Dicke ladder](#). *Opt. Lett.*, 47(6):1541, 2022. 2

- [24] A. Angerer, K. Streltsov, T. Astner, S. Putz, H. Sumiya, S. Onoda, J. Isoya, W. J. Munro, K. Nemoto, J. Schmiedmayer, et al. [Superradiant emission from colour centres in diamond](#). *Nat. Phys.*, 14(12):1168, 2018. 2
- [25] J. A. Mlynek, A. A. Abdumalikov, C. Eichler, and A. Wallraff. [Observation of Dicke superradiance for two artificial atoms in a cavity with high decay rate](#). *Nat. Commun.*, 5(1):1, 2014. 2
- [26] M. Scheibner, T. Schmidt, L. Worschech, A. Forchel, G. Bacher, T. Passow, and D. Hommel. [Superradiance of quantum dots](#). *Nat. Phys.*, 3(2):106, 2007. 2
- [27] K. Cong, Q. Zhang, Y. Wang, G. T. Noe, A. Belyanin, and J. Kono. [Dicke superradiance in solids](#). *JOSA B*, 33(7):C80, 2016. 2
- [28] D. Pavolini, A. Crubellier, P. Pillet, L. Cabaret, and S. Liberman. [Experimental evidence for subradiance](#). *Phys. Rev. Lett.*, 54(17):1917, 1985. 2
- [29] Y. Takasu, Y. Saito, Y. Takahashi, M. Borkowski, R. Ciuryło, and P. S. Julienne. [Controlled production of subradiant states of a diatomic molecule in an optical lattice](#). *Phys. Rev. Lett.*, 108(17):173002, 2012.
- [30] C. Hettich, C. Schmitt, J. Zitzmann, S. Kuhn, I. Gerhardt, and V. Sandoghdar. [Nanometer resolution and coherent optical dipole coupling of two individual molecules](#). *Science*, 298(5592):385, 2002.
- [31] B. H. McGuyer, M. McDonald, G. Z. Iwata, M. G. Tarallo, W. Skomorowski, R. Moszynski, and T. Zelevinsky. [Precise study of asymptotic physics with subradiant ultracold molecules](#). *Nat. Phys.*, 11(1):32, 2015. 2
- [32] M. O. Scully, E. S. Fry, C. R. Ooi, and K. Wódkiewicz. [Directed spontaneous emission from an extended ensemble of N atoms: Timing is everything](#). *Phys. Rev. Lett.*, 96(1):010501, 2006. 2, 53
- [33] M. O. Scully and A. A. Svidzinsky. [The super of superradiance](#). *Science*, 325(5947):1510, 2009. 2, 22, 26
- [34] M. O. Scully. [Collective Lamb shift in single photon Dicke superradiance](#). *Phys. Rev. Lett.*, 102(14):143601, 2009. 2
- [35] M. O. Scully. [Single photon subradiance: quantum control of spontaneous emission and ultrafast readout](#). *Phys. Rev. Lett.*, 115(24):243602, 2015. 2

- [36] W. Guerin, M. O. Araújo, and R. Kaiser. [Subradiance in a large cloud of cold atoms](#). *Phys. Rev. Lett.*, 116(8):083601, 2016. [2](#), [22](#), [75](#)
- [37] M. O. Araújo, I. Krešić, R. Kaiser, and W. Guerin. [Superradiance in a large and dilute cloud of cold atoms in the linear-optics regime](#). *Phys. Rev. Lett.*, 117(7):073002, 2016.
- [38] S. Roof, K. Kemp, M. Havey, and I. Sokolov. [Observation of single-photon superradiance and the cooperative Lamb shift in an extended sample of cold atoms](#). *Phys. Rev. Lett.*, 117(7):073003, 2016.
- [39] D. Das, B. Lemberger, and D. Yavuz. [Subradiance and superradiance-to-subradiance transition in dilute atomic clouds](#). *Phys. Rev. A*, 102(4):043708, 2020. [2](#), [75](#)
- [40] N. Stiesdal, H. Busche, J. Kumlin, K. Kleinbeck, H. P. Büchler, and S. Hofferberth. [Observation of collective decay dynamics of a single Rydberg superatom](#). *Phys. Rev. Res.*, 2(4):043339, 2020. [2](#), [22](#)
- [41] A. S. Sheremet, M. I. Petrov, I. V. Iorsh, A. V. Poshakinskiy, and A. N. Poddubny. [Waveguide quantum electrodynamics: collective radiance and photon-photon correlations](#). *Rev. Mod. Phys.*, 95(1):015002, 2023. [2](#), [3](#), [22](#)
- [42] A. Goban, C.-L. Hung, J. D. Hood, S.-P. Yu, J. A. Muniz, O. Painter, and H. J. Kimble. [Superradiance for atoms trapped along a photonic crystal waveguide](#). *Phys. Rev. Lett.*, 115(6):063601, 2015. [22](#)
- [43] P. Solano, P. Barberis-Blostein, F. K. Fatemi, L. A. Orozco, and S. L. Rolston. [Super-radiance reveals infinite-range dipole interactions through a nanofiber](#). *Nat. Commun.*, 8(1857):1, 2017. [23](#)
- [44] N. V. Corzo, J. Raskop, A. Chandra, A. S. Sheremet, B. Gouraud, and J. Laurat. [Waveguide-coupled single collective excitation of atomic arrays](#). *Nature*, 566(7744):359, 2019.
- [45] S. Okaba, D. Yu, L. Vincetti, F. Benabid, and H. Katori. [Superradiance from lattice-confined atoms inside hollow core fibre](#). *Commun. Phys.*, 2(136):1, 2019. [49](#), [75](#), [76](#)
- [46] R. Pennetta, M. Blaha, A. Johnson, D. Lechner, P. Schneeweiss, J. Volz, and A. Rauschenbeutel. [Collective radiative dynamics of an ensemble of cold atoms coupled to an optical waveguide](#). *Phys. Rev. Lett.*, 128(7):073601, 2022. [21](#), [49](#)

- [47] R. Pennetta, D. Lechner, M. Blaha, A. Rauschenbeutel, P. Schneeweiss, and J. Volz. [Observation of coherent coupling between super- and subradiant states of an ensemble of cold atoms collectively coupled to a single propagating optical mode.](#) *Phys. Rev. Lett.*, 128(20):203601, 2022. 2, 22, 75, 76, 77
- [48] W. Zakowicz and K. Rzazewski. [Collective radiation by harmonic oscillators.](#) *J. Phys. A Math. Theor.*, 7(7):869, 1974. 2
- [49] A. A. Svidzinsky, J.-T. Chang, and M. O. Scully. [Cooperative spontaneous emission of N atoms: Many-body eigenstates, the effect of virtual Lamb shift processes, and analogy with radiation of N classical oscillators.](#) *Phys. Rev. A*, 81(5):053821, 2010. 2
- [50] W. Guerin, M. Rouabah, and R. Kaiser. [Light interacting with atomic ensembles: collective, cooperative and mesoscopic effects.](#) *J. Mod. Opt.*, 64(9):895, 2017. 2, 56
- [51] A. Cipris, N. A. Moreira, T. S. do Espirito Santo, P. Weiss, C. J. Villas-Boas, R. Kaiser, W. Guerin, and R. Bachelard. [Subradiance with saturated atoms: Population enhancement of the long-lived states.](#) *Phys. Rev. Lett.*, 126(10):103604, 2021. 2, 75
- [52] D. Meiser, J. Ye, D. R. Carlson, and M. J. Holland. [Prospects for a millihertz-linewidth laser.](#) *Phys. Rev. Lett.*, 102(16):163601, 2009. 2
- [53] J. G. Bohnet, Z. Chen, J. M. Weiner, D. Meiser, M. J. Holland, and J. K. Thompson. [A steady-state superradiant laser with less than one intracavity photon.](#) *Nature*, 484(7392):78, 2012.
- [54] M. A. Norcia and J. K. Thompson. [Cold-strontium laser in the superradiant crossover regime.](#) *Phys. Rev. X*, 6(1):011025, 2016. 2
- [55] A. M. Kaufman and K.-K. Ni. [Quantum science with optical tweezer arrays of ultracold atoms and molecules.](#) *Nat. Phys.*, 17(12):1324, 2021. 2
- [56] D. Porras and J. I. Cirac. [Collective generation of quantum states of light by entangled atoms.](#) *Phys. Rev. A*, 78(5):053816, 2008. 2, 98
- [57] A. González-Tudela, V. Paulisch, D. E. Chang, H. J. Kimble, and J. I. Cirac. [Deterministic generation of arbitrary photonic states assisted by dissipation.](#) *Phys. Rev. Lett.*, 115(16):163603, 2015. 98
- [58] C. Groiseau, A. E. Elliott, S. J. Masson, and S. Parkins. [Proposal for a deterministic single-atom source of quasisuperradiant N-photon pulses.](#) *Phys. Rev. Lett.*, 127(3):033602, 2021. 2

- [59] V. Paulisch, M. Perarnau-Llobet, A. González-Tudela, and J. I. Cirac. [Quantum metrology with one-dimensional superradiant photonic states](#). *Phys. Rev. A*, 99(4):043807, 2019. **3**, **97**, **98**
- [60] M. Perarnau-Llobet, A. González-Tudela, and J. I. Cirac. [Multimode fock states with large photon number: effective descriptions and applications in quantum metrology](#). *Quantum Sci. Technol.*, 5(2):025003, 2020. **3**, **98**
- [61] G. Facchinetti, S. D. Jenkins, and J. Ruostekoski. [Storing light with subradiant correlations in arrays of atoms](#). *Phys. Rev. Lett.*, 117(24):243601, 2016. **3**
- [62] A. Asenjo-Garcia, M. Moreno-Cardoner, A. Albrecht, H. J. Kimble, and D. E. Chang. [Exponential improvement in photon storage fidelities using subradiance and “selective radiance” in atomic arrays](#). *Phys. Rev. X*, 7(3):031024, 2017. **3**
- [63] J. Rui, D. Wei, A. Rubio-Abadal, S. Hollerith, J. Zeiher, D. M. Stamper-Kurn, C. Gross, and I. Bloch. [A subradiant optical mirror formed by a single structured atomic layer](#). *Nature*, 583(7816):369, 2020. **3**, **22**, **75**
- [64] K. Srakaew, P. Weckesser, S. Hollerith, D. Wei, D. Adler, I. Bloch, and J. Zeiher. [A subwavelength atomic array switched by a single rydberg atom](#). *Nat. Phys.*, 2023. **3**
- [65] A. S. Solntsev, G. S. Agarwal, and Y. S. Kivshar. [Metasurfaces for quantum photonics](#). *Nat. Phot.*, 15(5):327, 2021. **3**
- [66] D. E. Chang, J. S. Douglas, A. González-Tudela, C.-L. Hung, and H. J. Kimble. [Colloquium: Quantum matter built from nanoscopic lattices of atoms and photons](#). *Rev. Mod. Phys.*, 90(3):031002, 2018. **3**
- [67] D. E. Chang, V. Vuletić, and M. D. Lukin. [Quantum nonlinear optics - photon by photon](#). *Nat. Phot.*, 8(9):685, 2014. **3**
- [68] K. Hammerer, A. S. Sørensen, and E. S. Polzik. [Quantum interface between light and atomic ensembles](#). *Rev. Mod. Phys.*, 82(2):1041, 2010. **3**
- [69] P. Lodahl, S. Mahmoodian, S. Stobbe, A. Rauschenbeutel, P. Schneeweiss, J. Volz, H. Pichler, and P. Zoller. [Chiral quantum optics](#). *Nature*, 541(7638):473, 2017. **3**, **4**, **8**, **16**, **18**, **113**
- [70] P. Lodahl, S. Mahmoodian, and S. Stobbe. [Interfacing single photons and single quantum dots with photonic nanostructures](#). *Rev. Mod. Phys.*, 87(2):347, 2015. **3**

- [71] D. Roy, C. M. Wilson, and O. Firstenberg. [Colloquium: Strongly interacting photons in one-dimensional continuum](#). *Rev. Mod. Phys.*, 89(2):021001, 2017.
- [72] K. P. Nayak, M. Sadgrove, R. Yalla, F. Le Kien, and K. Hakuta. [Nanofiber quantum photonics](#). *J. Opt.*, 20(7):073001, 2018.
- [73] A. W. Elshaari, W. Pernice, K. Srinivasan, O. Benson, and V. Zwiller. [Hybrid integrated quantum photonic circuits](#). *Nat. Phot.*, 14(5):285, 2020. 3
- [74] H. Carmichael. [Quantum trajectory theory for cascaded open systems](#). *Phys. Rev. Lett.*, 70(15):2273, 1993. 4, 30
- [75] C. Gardiner. [Driving a quantum system with the output field from another driven quantum system](#). *Phys. Rev. Lett.*, 70(15):2269, 1993. 4, 30
- [76] E. Vetsch, D. Reitz, G. Sagué, R. Schmidt, S. Dawkins, and A. Rauschenbeutel. [Optical interface created by laser-cooled atoms trapped in the evanescent field surrounding an optical nanofiber](#). *Phys. Rev. Lett.*, 104(20):203603, May 2010. 7, 9, 10, 13, 15
- [77] G. Sagué Cassany. [Cold atom physics using ultra-thin optical fibres](#). *PhD thesis: University of Bonn*, 2008. 7, 8
- [78] E. Vetsch. [Optical interface based on a nanofiber atom-trap](#). *PhD thesis: Johannes Gutenberg University Mainz*, 2011. 114, 115
- [79] R. Mitsch. [Interaction and manipulation of nanofiber-trapped atoms with spin-orbit coupled light](#). *PhD thesis: Technical University Wien*, 2014.
- [80] B. Albrecht. [Storage of fiber-guided light in a nanofiber-trapped ensemble of cold cesium atoms](#). *PhD thesis: Technical University Wien*, 2017.
- [81] Y. Meng. . *PhD thesis: Technical University Wien*, 2020. 29
- [82] S. Pucher. [Non-reciprocal optical amplification and phase shifts in a nanofiber-based atom-light interface and a precise lifetime measurement of the cesium \$5d5/2\$ state](#). *PhD thesis: Humboldt University of Berlin*, 2022. 7, 17, 89
- [83] F. Warken. [Ultradünne glasfasern als werkzeuge zur kopplung von licht und materie](#). *University of Bonn*, 2007. 7
- [84] A. Stiebeiner, R. Garcia-Fernandez, and A. Rauschenbeutel. [Design and optimization of broadband tapered optical fibers with a nanofiber waist](#). *Opt. Exp.*, 18(22):22677, 2010. 7

- [85] F. L. Kien, J. Liang, K. Hakuta, and V. Balykin. [Field intensity distributions and polarization orientations in a vacuum-clad subwavelength-diameter optical fiber.](#) *Opt. Commun.*, 242(4-6):445, 2004. 8
- [86] F. Le Kien, P. Schneeweiss, and A. Rauschenbeutel. [Dynamical polarizability of atoms in arbitrary light fields: general theory and application to cesium.](#) *Eur. Phys. J. D*, 67(5):1, 2013. 10
- [87] S. Buhmann. [Microscopic quantum electrodynamics and ground-state Casimir, Casimir-Polder and van der Waals forces.](#) 2012. 10
- [88] N. Schlosser, G. Reymond, and P. Grangier. [Collisional blockade in microscopic optical dipole traps.](#) *Phys. Rev. Lett.*, 89(2):023005, 2002. 10
- [89] D. A. Steck. [Cesium D line data.](#) Available online at: <https://steck.us/alkalidata> (Version 2.2.1), 2019. 11, 18, 114
- [90] Y. Meng, A. Dureau, P. Schneeweiss, and A. Rauschenbeutel. [Near-ground-state cooling of atoms optically trapped 300 nm away from a hot surface.](#) *Phys. Rev. X*, 8(3):031054, 2018. 11, 14
- [91] Y. Meng, C. Liedl, S. Pucher, A. Rauschenbeutel, and P. Schneeweiss. [Imaging and localizing individual atoms interfaced with a nanophotonic waveguide.](#) *Phys. Rev. Lett.*, 125(5):053603, 2020. 12, 15, 29, 98
- [92] R. Mitsch, C. Sayrin, B. Albrecht, P. Schneeweiss, and A. Rauschenbeutel. [Quantum state-controlled directional spontaneous emission of photons into a nanophotonic waveguide.](#) *Nat. Commun.*, 5(5713):1, 2014. 18, 30
- [93] S. Pucher, C. Liedl, S. Jin, A. Rauschenbeutel, and P. Schneeweiss. [Atomic spin-controlled non-reciprocal Raman amplification of fibre-guided light.](#) *Nat. Phot.*, 16(5):380, 2022. 18, 84
- [94] T. do Espirito Santo, P. Weiss, A. Cipris, R. Kaiser, W. Guerin, R. Bachelard, and J. Schachenmayer. [Collective excitation dynamics of a cold atom cloud.](#) *Phys. Rev. A*, 101(1):013617, 2020. 22
- [95] Y. He, L. Ji, Y. Wang, L. Qiu, J. Zhao, Y. Ma, X. Huang, S. Wu, and D. E. Chang. [Geometric control of collective spontaneous emission.](#) *Phys. Rev. Lett.*, 125(21):213602, 2020. 22
- [96] F. L. Kien and K. Hakuta. [Cooperative enhancement of channeling of emission from atoms into a nanofiber.](#) *Phys. Rev. A*, 77(1):013801, 2008. 22

- [97] A. Asenjo-Garcia, J. Hood, D. Chang, and H. Kimble. [Atom-light interactions in quasi-one-dimensional nanostructures: A Green's-function perspective](#). *Phys. Rev. A*, 95(3):033818, 2017. 22
- [98] F. Le Kien, S. D. Gupta, K. Nayak, and K. Hakuta. [Nanofiber-mediated radiative transfer between two distant atoms](#). *Phys. Rev. A*, 72(6):063815, 2005. 23
- [99] S. Cardenas-Lopez, S. J. Masson, Z. Zager, and A. Asenjo-Garcia. [Many-body superradiance and dynamical symmetry breaking in waveguide QED](#). *arXiv:2209.12970*, 2022. 23, 24, 28, 29, 81, 98
- [100] N. V. Corzo, B. Gouraud, A. Chandra, A. Goban, A. S. Sheremet, D. V. Kupriyanov, and J. Laurat. [Large bragg reflection from one-dimensional chains of trapped atoms near a nanoscale waveguide](#). *Phys. Rev. Lett.*, 117(13):133603, 2016. 28
- [101] H. Sørensen, J.-B. Béguin, K. Kluge, I. Iakoupov, A. Sørensen, J. Müller, E. Polzik, and J. Appel. [Coherent backscattering of light off one-dimensional atomic strings](#). *Phys. Rev. Lett.*, 117(13):133604, 2016. 28
- [102] C. W. Gardiner and M. J. Collett. [Input and output in damped quantum systems: Quantum stochastic differential equations and the master equation](#). *Phys. Rev. A*, 31(6):3761, 1985. 31, 116
- [103] G. Lindblad. [On the generators of quantum dynamical semigroups](#). *Commun. Math. Phys.*, 48(2):119, 1976. 31, 85, 124
- [104] H. J. Carmichael. [Statistical methods in quantum optics 1: master equations and fokker-planck equations](#). *Springer Science & Business Media*, 1, 1999. 31, 32, 121
- [105] R. Kubo. [Generalized cumulant expansion method](#). *JPSJ*, 17(7):1100, 1962. 36
- [106] D. Plankensteiner, C. Hotter, and H. Ritsch. [Quantumcumulants.jl: A Julia framework for generalized mean-field equations in open quantum systems](#). *Quantum*, 6:617, 2022. 36
- [107] O. Rubies-Bigorda, S. Ostermann, and S. F. Yelin. [Characterizing superradiant dynamics in atomic arrays via a cumulant expansion approach](#). *Phys. Rev. Res.*, 5(1):013091, 2023. 36
- [108] C. Liedl, S. Pucher, F. Tebbenjohanns, P. Schneeweiss, and A. Rauschenbeutel. [Collective radiation of a cascaded quantum system: From timed Dicke states to inverted ensembles](#). *Phys. Rev. Lett.*, 130(16):163602, 2023. 43

- [109] A. F. J. Levi. [The lorentz oscillator model](#). *Morgan and Claypool Publishers*, 2016. 44
- [110] S. L. McCall and E. L. Hahn. [Self-induced transparency by pulsed coherent light](#). *Phys. Rev. Lett.*, 18(21):908, 1967. 44
- [111] G. T. Genov, D. Schraft, T. Halfmann, and N. V. Vitanov. [Correction of arbitrary field errors in population inversion of quantum systems by universal composite pulses](#). *Phys. Rev. Lett.*, 113(4):043001, 2014. 51
- [112] Y. Ma, X. Huang, X. Wang, L. Ji, Y. He, L. Qiu, J. Zhao, Y. Wang, and S. Wu. [Precise pulse shaping for quantum control of strong optical transitions](#). *Opt. Exp.*, 28(12):17171, 2020.
- [113] Y. Ma, R. Liu, L. Ji, L. Qiu, S. Wu, D. Su, Y. Zhao, N. Yao, and W. Fang. [Composite picosecond control of atomic state through a nanofiber interface](#). *arXiv:2203.06716*, 2022. 51
- [114] E. Treacy. [Adiabatic inversion with light pulses](#). *Phys. Lett. A*, 27(7):421, 1968. 51
- [115] T. Rickes, L. Yatsenko, S. Steuerwald, T. Halfmann, B. Shore, N. Vitanov, and K. Bergmann. [Efficient adiabatic population transfer by two-photon excitation assisted by a laser-induced stark shift](#). *J. Chem. Phys.*, 113(2):534, 2000. 51
- [116] R. J. Mailloux. [Phased array antenna handbook](#). *Artech house*, 2017. 53, 64
- [117] P. Berman. [Energy conservation in collective coherent emission by dipole oscillators](#). *Am. J. Phys.*, 78(12):1323, 2010. 54
- [118] S. Scheel, S. Y. Buhmann, C. Clausen, and P. Schneeweiss. [Directional spontaneous emission and lateral Casimir-Polder force on an atom close to a nanofiber](#). *Phys. Rev. A*, 92(4):043819, 2015. 57
- [119] F. Robicheaux and S. Huang. [Atom recoil during coherent light scattering from many atoms](#). *Phys. Rev. A*, 99(1):013410, 2019. 57
- [120] D. E. Chang, J. I. Cirac, and H. J. Kimble. [Self-organization of atoms along a nanophotonic waveguide](#). *Phys. Rev. Lett.*, 110(11):113606, 2013. 57
- [121] D. Holzmann, M. Sonnleitner, and H. Ritsch. [Self-ordering and collective dynamics of transversely illuminated point-scatterers in a 1d trap](#). *Eur. Phys. J. D*, 68(11):1, 2014.

- [122] Z. Eldredge, P. Solano, D. Chang, and A. V. Gorshkov. [Self-organization of atoms coupled to a chiral reservoir](#). *Phys. Rev. A*, 94(5):053855, 2016. 57
- [123] G. Ferioli, A. Glicenstein, I. Ferrier-Barbut, and A. Browaeys. [Observation of a non-equilibrium superradiant phase transition in free space](#). *arXiv:2207.10361*, 2022. 57, 98
- [124] C. Liedl, F. Tebbenjohanns, C. Bach, S. Pucher, A. Rauschenbeutel, and P. Schneeweiss. [Observation of superradiant bursts in waveguide QED](#). *arXiv:2211.08940*, 2022. 59
- [125] A. R. Willms, P. M. Kitanov, and W. F. Langford. [Huygens' clocks revisited](#). *R. Soc. Open Sci.*, 4(9):170777, 2017. 59
- [126] S. Strogatz. [Sync: The emerging science of spontaneous order](#). *Penguin UK*, 2004. 59
- [127] R. Bonifacio and L. Lugiato. [Cooperative radiation processes in two-level systems: Superfluorescence](#). *Phys. Rev. A*, 11(5):1507, 1975. 61, 66
- [128] F. Haake, H. King, G. Schröder, J. Haus, and R. Glauber. [Fluctuations in superfluorescence](#). *Phys. Rev. A*, 20(5):2047, 1979.
- [129] M. Schuurmans, Q. Vrehen, D. Polder, and H. Gibbs. [Superfluorescence](#). *Adv. At. Mol. Phys.*, 17:167, 1982. 66
- [130] Q. Vrehen and M. Schuurmans. [Direct measurement of the effective initial tipping angle in superfluorescence](#). *Phys. Rev. Lett.*, 42(4):224, 1979. 66
- [131] C. Lee. [Effects of pumping process on the tipping angle and quantum fluctuations in superfluorescence](#). *Phys. Rev. Lett.*, 43(15):1110, 1979. 66
- [132] R. J. Glauber. [The quantum theory of optical coherence](#). *Phys. Rev.*, 130(6):2529, 1963. 68
- [133] H. A. Haus. [Electromagnetic noise and quantum optical measurements](#). *Springer Science & Business Media*, 2000. 70
- [134] G. Ferioli, A. Glicenstein, L. Henriot, I. Ferrier-Barbut, and A. Browaeys. [Storage and release of subradiant excitations in a dense atomic cloud](#). *Phys. Rev. X*, 11(2):021031, 2021. 75

- [135] J. Kumlin, K. Kleinbeck, N. Stiesdal, H. Busche, S. Hofferberth, and H. P. Büchler. [Nonexponential decay of a collective excitation in an atomic ensemble coupled to a one-dimensional waveguide](#). *Phys. Rev. A*, 102(6):063703, 2020. 75, 76
- [136] U. Van Bürck. [Coherent pulse propagation through resonant media](#). *Hyperfine Interactions*, 123(1):483, 1999. 75
- [137] S. J. Masson and A. Asenjo-Garcia. [Universality of Dicke superradiance in arrays of quantum emitters](#). *Nat. Comm.*, 13(2285):1, 2022. 82
- [138] C. Liedl, S. Pucher, P. Schneeweiss, L. Yatsenko, and A. Rauschenbeutel. [Observation of oscillatory Raman gain associated with two-photon Rabi oscillations of nanofiber-coupled atoms](#). *J. Phys. B: At. Mol. Opt. Phys.*, 55(23):234005, 2022. 83, 84, 124
- [139] M. Fleischhauer, A. Imamoglu, and J. P. Marangos. [Electromagnetically induced transparency: Optics in coherent media](#). *Rev. Mod. Phys.*, 77(2):633, 2005. 83
- [140] L. V. Hau, S. E. Harris, Z. Dutton, and C. H. Behroozi. [Light speed reduction to 17 metres per second in an ultracold atomic gas](#). *Nature*, 397(6720):594, 1999. 83
- [141] A. E. Kozhekin, K. Mølmer, and E. Polzik. [Quantum memory for light](#). *Phys. Rev. A*, 62(3):033809, Aug 2000. 83
- [142] L.-M. Duan, M. D. Lukin, J. I. Cirac, and P. Zoller. [Long-distance quantum communication with atomic ensembles and linear optics](#). *Nature*, 414(6862):413, 2001. 83
- [143] N. V. Vitanov, T. Halfmann, B. W. Shore, and K. Bergmann. [Laser-induced population transfer by adiabatic passage techniques](#). *Annu. Rev. Phys. Chem.*, 52(1):763, 2001. 83
- [144] H. Hatanaka and T. Hashi. [Transient nutations and spin echoes associated with two-quantum transition in multi-level NMR system](#). *J. Phys. Soc. Japan*, 39(4):1139, 1975. 83
- [145] A. Linskens, I. Holleman, N. Dam, and J. Reuss. [Two-photon Rabi oscillations](#). *Phys. Rev. A*, 54(6):4854, 1996. 83
- [146] T. R. Gentile, B. J. Hughey, D. Kleppner, and T. W. Ducas. [Experimental study of one- and two-photon Rabi oscillations](#). *Phys. Rev. A*, 40(9):5103, 1989. 83

- [147] D. Grison, B. Lounis, C. Salomon, J. Courtois, and G. Grynberg. [Raman spectroscopy of cesium atoms in a laser trap](#). *Europhys. Lett.*, 15(2):149, 1991. 84
- [148] J. Tabosa, G. Chen, Z. Hu, R. Lee, and H. Kimble. [Nonlinear spectroscopy of cold atoms in a spontaneous-force optical trap](#). *Phys. Rev. Lett.*, 66(25):3245, 1991.
- [149] L. Hilico, C. Fabre, and E. Giacobino. [Operation of a “cold-atom laser” in a magneto-optical trap](#). *Europhys. Lett.*, 18(8):685, 1992.
- [150] W. Guerin, F. Michaud, and R. Kaiser. [Mechanisms for lasing with cold atoms as the gain medium](#). *Phys. Rev. Lett.*, 101(9):093002, 2008. 84
- [151] K. Bergmann, H. Theuer, and B. Shore. [Coherent population transfer among quantum states of atoms and molecules](#). *Rev. Mod. Phys.*, 70(3):1003, 1998. 85, 124
- [152] E. Brion, L. H. Pedersen, and K. Mølmer. [Adiabatic elimination in a Lambda system](#). *J. Phys. A Math. Theor.*, 40(5):1033, 2007. 86, 87
- [153] C. F. Bohren and D. R. Huffman. [Absorption and scattering of light by small particles](#). *John Wiley & Sons*, 2008. 89
- [154] S. H. Autler and C. H. Townes. [Stark effect in rapidly varying fields](#). *Phys. Rev.*, 100(2):703, 1955. 90
- [155] C. N. Cohen-Tannoudji. [The Autler-Townes effect revisited](#). *Amazing Light, Springer*, 1996.
- [156] R. Kumar, V. Gokhroo, K. Deasy, and S. N. Chormaic. [Autler-Townes splitting via frequency up-conversion at ultralow-power levels in cold \$^{87}\text{Rb}\$ atoms using an optical nanofiber](#). *Phys. Rev. A*, 91(5):053842, 2015. 90
- [157] D. A. Steck. [Quantum and atom optics](#). Available online at <http://steck.us/teaching> (revision 0.13.10), 2021. 94, 116
- [158] Y. Yoshikawa, Y. Torii, and T. Kuga. [Superradiant light scattering from thermal atomic vapors](#). *Phys. Rev. Lett.*, 94(8):083602, 2005. 96
- [159] K. Kusmierik, K. Hammerer, S. Cardenas-Lopez, and A. Asenjo-Garcia. *Private communication*, 2022. 97
- [160] T. Peters and L. Yatsenko. *Private communication*, 2022. 98

- [161] A. S. Prasad, J. Hinney, S. Mahmoodian, K. Hammerer, S. Rind, P. Schneeweiss, A. S. Sørensen, J. Volz, and A. Rauschenbeutel. [Correlating photons using the collective nonlinear response of atoms weakly coupled to an optical mode](#). *Nat. Phot.*, 14(12):719, 2020. 98
- [162] J. Hinney, A. S. Prasad, S. Mahmoodian, K. Hammerer, A. Rauschenbeutel, P. Schneeweiss, J. Volz, and M. Schemmer. [Unraveling two-photon entanglement via the squeezing spectrum of light traveling through nanofiber-coupled atoms](#). *Phys. Rev. Lett.*, 127(12):123602, 2021.
- [163] M. Cordier, M. Schemmer, P. Schneeweiss, J. Volz, and A. Rauschenbeutel. [Tailoring photon statistics with an atom-based two-photon interferometer](#). *arXiv:2212.09592*, 2022. 98
- [164] N. Stiesdal. [Collective atom-light interactions with rydberg superatoms](#). *PhD thesis: University of Southern Denmark*, 2022. 98
- [165] S. Mahmoodian, G. Calajó, D. E. Chang, K. Hammerer, and A. S. Sørensen. [Dynamics of many-body photon bound states in chiral waveguide qed](#). *Phys. Rev. X*, 10(3):031011, 2020. 98
- [166] K. Stannigel, P. Rabl, and P. Zoller. [Driven-dissipative preparation of entangled states in cascaded quantum-optical networks](#). *New J. Phys.*, 14(6):063014, 2012. 98
- [167] T. Ramos, H. Pichler, A. J. Daley, and P. Zoller. [Quantum spin dimers from chiral dissipation in cold-atom chains](#). *Phys. Rev. Lett.*, 113(23):237203, 2014.
- [168] H. Pichler, T. Ramos, A. J. Daley, and P. Zoller. [Quantum optics of chiral spin networks](#). *Phys. Rev. A*, 91(4):042116, 2015. 98
- [169] P. Van der Straten and H. Metcalf. [Atoms and molecules interacting with light: Atomic physics for the laser era](#). *Cambridge University Press*, 2016. 115
- [170] H. C. Torrey. [Transient nutations in nuclear magnetic resonance](#). *Phys. Rev.*, 76(8):1059, 1949. 116

A Appendix

A.1 Transmission coefficient on resonance

The transmission coefficient of a single atom that is coupled to an optical waveguide is well known [69]. Here, we present a somewhat hand-waving but intuitive derivation based on a beam splitter model. We will assume weak, resonant driving and a coupling strength of β_f . We model the system as an interferometer, which is depicted in Fig. A.1. A light field E_{in} impinges on a beam splitter with field reflection and transmission coefficients r_{BS} and t_{BS} , respectively. The reflected field is then assumed to perfectly couple to a single two-level atom. Since we have defined the coupling strength, β_f , as the partial decay rate into the forward-propagating mode, $|r_{\text{BS}}|^2 = \beta_f$ in the beam splitter model, since a fraction of β_f of the emitted power couples to the forward-propagating mode. We choose $r_{\text{BS}} \in \mathbb{R}$, such that $r_{\text{BS}} = \sqrt{\beta_f}$. Using $|r|^2 + |t|^2 = 1$, we then obtain $t_{\text{BS}} = \sqrt{1 - \beta_f}$. We also assume that the propagating phases are the same in both arms of the interferometer. The transmitted field, E_f , can be computed by interfering the field that is reflected twice with the field that is transmitted twice,

$$E_f = t_{\text{BS}}^2 E_{\text{in}} - r_{\text{BS}}^2 E_{\text{in}}. \quad (\text{A.1})$$

The minus sign originates from the relative phase between the incoming field and the field scattered by the atomic dipole. For weak resonant excitation, the field emitted by the dipole is π -out of phase, yielding a minus-sign for the field in the upper arm of the

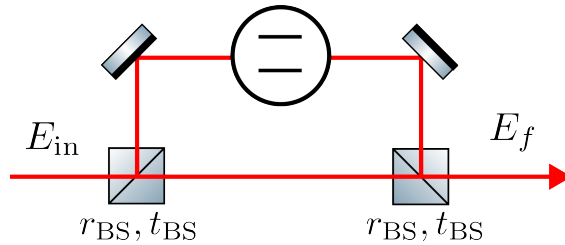


Figure A.1: Beam splitter model of transmission through a waveguide for a single atom that is coupled to the forward-propagating mode with a coupling strength, β_f .

interferometer in Fig. A.1. Thus, the scattered field interferes destructively with the incoming light field, i.e., the atom absorbs light. The field transmission coefficient through the nanofiber is given by

$$t = \frac{E_f}{E_{\text{in}}} = 1 - 2\beta_f. \quad (\text{A.2})$$

For small $\beta_f \ll 1$, the power transmission coefficient is

$$T = |t|^2 = 1 - 4\beta_f. \quad (\text{A.3})$$

where we have neglected the term of order β_f^2 , which is appropriate for $\beta_f \approx 0.01$ in our experiment. The optical depth of a single atom, OD_0 , is defined via the power transmission coefficient, $T = \exp(-OD_0) \approx 1 - OD_0$. By comparing this expression with Eq.(A.3), we obtain

$$OD_0 = 4\beta_f. \quad (\text{A.4})$$

A.2 Rabi frequency of a nanofiber-guided light field

The Rabi frequency of a light field is usually defined as

$$\Omega = \frac{\vec{d} \cdot \vec{E}}{\hbar}, \quad (\text{A.5})$$

where \vec{d} is the transition dipole moment and \vec{E} the electromagnetic field. Computing the electric field of the nanofiber-guided mode at the position of the atoms is quite cumbersome. Thus, it is useful to express the Rabi frequency in terms of the coupling strength, β_f , and the optical power, P , which can both be measured.

The saturation parameter, S , is defined as [89]

$$S = \frac{I}{I_{\text{sat}}} = 2 \frac{\Omega^2}{\Gamma^2}, \quad (\text{A.6})$$

where I is the intensity at the position of the atom and I_{sat} denotes the saturation intensity [89],

$$I_{\text{sat}} = \frac{\hbar\omega\Gamma}{2\sigma_0}. \quad (\text{A.7})$$

Here, $\sigma_0 = 3\lambda^2/2\pi$ is the resonant scattering cross section of a single atom [78]. We thus obtain

$$\Omega = \sqrt{\frac{\sigma_0\Gamma I}{\hbar\omega}}. \quad (\text{A.8})$$

In order to find how Ω depends on P and β_f , we thus have to find how I depends on β_f and P . For a given input power, P , the atoms are exposed to the intensity

$$I = \frac{P}{A_{\text{eff}}}, \quad (\text{A.9})$$

where we have introduced the effective mode area, A_{eff} . With these definitions, a single atom absorbs a fraction of σ_0/A_{eff} from a weak, resonant probe field [78]. For $\sigma_0/A_{\text{eff}} \ll 1$, we can write

$$T = \exp\left(-\frac{\sigma_0}{A_{\text{eff}}}\right). \quad (\text{A.10})$$

Comparing the exponent of the above equation to the optical depth of a single atom, see Eq. (A.4), we get

$$A_{\text{eff}} = \frac{\sigma_0}{4\beta_f}, \quad (\text{A.11})$$

such that the intensity is given by

$$I = \frac{4\beta_f P}{\sigma_0}. \quad (\text{A.12})$$

Finally, we insert the above expression for I into Eq. (A.8) and obtain

$$\Omega = \sqrt{\frac{4\beta_f \Gamma P}{\hbar\omega}}. \quad (\text{A.13})$$

A.3 Optical Bloch equations for a two-level atom

In the rotating wave approximation, the interaction of a single two-level atom with a coherent light field is described by the following Hamiltonian [169]

$$\hat{\mathcal{H}} = \hbar\Delta\hat{\sigma}^\dagger\hat{\sigma} + \frac{\hbar\Omega}{2}(\hat{\sigma}^\dagger + \hat{\sigma}), \quad (\text{A.14})$$

where Δ and Ω describe the detuning and Rabi frequency of the light field, respectively. The dynamics of the atomic density matrix, $\hat{\rho}$ is then determined by the Lindblad master equation,

$$\dot{\hat{\rho}} = -\frac{i}{\hbar}[\hat{\mathcal{H}}, \hat{\rho}] + \Gamma\left[\hat{\sigma}\hat{\rho}\hat{\sigma}^\dagger - \frac{1}{2}(\hat{\sigma}^\dagger\hat{\sigma}\hat{\rho} + \hat{\rho}\hat{\sigma}^\dagger\hat{\sigma})\right]. \quad (\text{A.15})$$

The first term describes coherent evolution, while the second term describes dissipation. Since $\rho_{ee} + \rho_{gg} = 1$, and $\rho_{ge} = \rho_{eg}^*$, it is sufficient to solve the following two equations:

$$\dot{\rho}_{eg} = -i\Delta\rho_{eg} - \frac{\Gamma}{2}\rho_{eg} - \frac{i}{2}\Omega(1 - 2\rho_{ee}), \quad (\text{A.16})$$

$$\dot{\rho}_{ee} = -\Gamma\rho_{ee} + \frac{i}{2}\Omega(\rho_{eg} - \rho_{ge}). \quad (\text{A.17})$$

A.3.1 Transmission coefficient for arbitrary detuning

In the weak excitation regime, the excited state probability ρ_{ee} vanishes, i.e., $\rho_{ee} \ll 1$. Then, one can solve Eq. (A.16) in the steady state,

$$\rho_{eg}^{ss} = \lim_{t \rightarrow \infty} \rho_{eg} = \frac{-i\Omega}{2i\Delta + \Gamma}. \quad (\text{A.18})$$

For a given input field E_{in} , the forward scattered field E_f can be obtained via the input output equation [102],

$$E_f = E_{\text{in}} - i\sqrt{\beta_f\Gamma}\rho_{eg}. \quad (\text{A.19})$$

Inserting ρ_{eg}^{ss} for ρ_{eg} and using the relation $\Omega = \sqrt{4\beta_f\Gamma}E_{\text{in}}$, we can calculate the amplitude transmission coefficient, t ,

$$t(\Delta) = \frac{E_f}{E_{\text{in}}} = 1 - \frac{\beta_f\Gamma}{i\Delta + \Gamma/2}. \quad (\text{A.20})$$

The power transmission coefficient through an ensemble of N atoms is then given by

$$\begin{aligned} T_N(\Delta) &= |t(\Delta)^N|^2 \approx \left| \left(1 - \frac{\beta_f\Gamma}{i\Delta + \Gamma/2} \right)^N \right|^2 = \exp \left[2N \ln \left(1 - \frac{\beta_f\Gamma}{i\Delta + \Gamma/2} \right) \right] \\ &\approx \exp \left[-\frac{2\beta_f N \Gamma}{i\Delta + \Gamma/2} \right] =: \exp[-OD(\Delta)], \end{aligned} \quad (\text{A.21})$$

where we have again neglected terms of order β_f^2 . The on-resonance optical depth is thus given by $OD(0) = 4\beta_f N$, consistent with our derivation in section A.1.

A.3.2 Analytical solution

While an analytical solutions to the optical Bloch equations exists, here we will only treat the case of resonant driving, i.e., $\Delta = 0$ [170]. This can be done either by using a computer program like Mathematica or by following the approach known as Torrey's solution, which is well explained, e.g., in Ref. [157]. We assume that the atom is initially prepared in the ground state, such that the initial conditions $\rho_{ee}(t=0) = 0$, $\rho_{eg}(t=0) = \rho_{ge}(t=0) = 0$.

The solutions are then given by:

$$\rho_{ee}(t) = \frac{\Omega^2}{2\Omega^2 + \Gamma^2} \left[1 - e^{-\frac{3\Gamma}{4}t} \left(\cos \Omega_\Gamma t + \frac{3\Gamma}{4\Omega_\Gamma} \sin \Omega_\Gamma t \right) \right], \quad (\text{A.22})$$

$$\rho_{ge}(t) = \frac{i\Omega\Gamma}{\Omega^2 + \Gamma^2/2} \left[1 - e^{-\frac{3\Gamma}{4}t} \left(\cos \Omega_\Gamma t - \frac{\Omega^2 - \Gamma^2/4}{\Gamma\Omega_\Gamma} \sin \Omega_\Gamma t \right) \right], \quad (\text{A.23})$$

$$\rho_{eg}(t) = \rho_{ge}^*(t). \quad (\text{A.24})$$

Here, Ω_Γ is the oscillation frequency in the presence of radiative damping with the rate Γ ,

$$\Omega_\Gamma = \sqrt{\Omega^2 - \frac{1}{4}\Gamma^2}. \quad (\text{A.25})$$

The pulse duration of $T_{\text{pulse}} = 4$ ns used in chapter 5 requires a Rabi frequency of $\Omega = 2\pi \times 125$ MHz. For this setting, the value of $\Omega_\Gamma = 2\pi \times 124.97$ MHz is almost the same as Ω , which is why we do not take into account this modification of the oscillation frequency in the main part of this thesis.

If we assume $\Omega_\Gamma = \pi/T_\pi$, we can calculate the excited state probability after a π -pulse with duration T_π , i.e. $\rho_{ee}(t = T_\pi)$,

$$p_{\text{exc}}(T_\pi) = \frac{4(\pi/T_\pi)^2 + \Gamma^2}{8(\pi/T_\pi)^2 + 5\Gamma^2} \left(1 - e^{-\frac{3\Gamma}{4}T_\pi} \right), \quad (\text{A.26})$$

which is plotted in Fig. 4.2(a) as a function of T_π .

A.4 Ideal Dicke superradiance in wQED

In this section, we analyze the many-body master equation (ME) of wQED for the case of unity coupling, i.e., $\beta_f + \beta_b = 1$, in two cases: symmetric and unidirectional atom-waveguide coupling. We furthermore compare the resulting ME to that of the ideal Dicke case, where all atoms are located at the same position. In the first case of symmetric coupling, we additionally assume that the atoms are arranged in the Bragg configuration, i.e., the spacing between different atoms is an integer multiple of the optical wavelength. In this case, the coefficients J_{ij} and Γ_{ij} are particularly simple,

$$J_{ij} = 0, \quad (\text{A.27})$$

$$\Gamma_{ij} = \Gamma, \quad (\text{A.28})$$

and the ME reads

$$\dot{\hat{\rho}} = \sum_{i,j=1}^N \frac{\Gamma}{2} \left(2\hat{\sigma}_i \hat{\rho} \hat{\sigma}_j^\dagger - \hat{\rho} \hat{\sigma}_j^\dagger \hat{\sigma}_i - \hat{\sigma}_j^\dagger \hat{\sigma}_i \hat{\rho} \right) = \frac{\Gamma}{2} \left(2\hat{S} \hat{\rho} \hat{S}^\dagger - \hat{\rho} \hat{S}^\dagger \hat{S} - \hat{S}^\dagger \hat{S} \hat{\rho} \right), \quad (\text{A.29})$$

where $\hat{S} = \sum_{i=1}^N \hat{\sigma}_i$ is the collective lowering operator. Equation (A.29) is identical to the master equation of ideal Dicke superradiance. In the Dicke regime, all atoms radiate into a single optical mode with unity coupling strength. They feature particle exchange symmetry, and any lowering operator that can act on the ensemble has to be symmetric with respect to particle exchange. In particular, the dynamics in Eq. (A.29) is purely dissipative, i.e., there are no dipole-dipole interactions between the atoms.

The situation becomes more complex when we introduce unidirectional coupling, where $\beta_f = 1$ and $\beta_b = 0$. In addition, one can absorb the propagation phases by introducing $\hat{\hat{\sigma}}_i = e^{ik_f z_i} \hat{\sigma}_i$, such that the ME becomes independent of the atomic positions, z_i . For the coefficients J_{ij} and Γ_{ij} , we get

$$J_{ij} = -\frac{i}{2} \Gamma \text{sign}(i - j), \quad (\text{A.30})$$

$$\Gamma_{ij} = \Gamma, \quad (\text{A.31})$$

and the ME reads

$$\dot{\hat{\rho}} = -\frac{i}{\hbar} [\hat{\mathcal{H}}, \hat{\rho}] + \frac{\Gamma}{2} \left(2\hat{S} \hat{\rho} \hat{S}^\dagger - \hat{\rho} \hat{S}^\dagger \hat{S} - \hat{S}^\dagger \hat{S} \hat{\rho} \right), \quad (\text{A.32})$$

$$\hat{\mathcal{H}} = -\frac{i\hbar\Gamma}{2} \sum_{i>j} \hat{\hat{\sigma}}_i^\dagger \hat{\hat{\sigma}}_j + \text{c.c.} \quad (\text{A.33})$$

The dissipative part is still the same as for symmetric coupling and the ideal Dicke case. However, now the effective Hamiltonian does not vanish. The nanofiber-guided mode mediates unidirectional dipole-dipole interactions between the atoms. This interaction seems to be responsible for the occurrence of subradiant dynamics after the emission of a superradiant burst by a fully inverted ensemble, see section 5.6.

A.5 Extracting the first-order correlation function from the heterodyne signal

In section 5.5.2, we extracted the first-order correlation function of the signal field from the second-order correlation function of a heterodyne signal. In this section, we present a more detailed explanation of this procedure. Let us assume a light field $\hat{a}(t)$ with power $P(t)$

that describes the light exiting the nanofiber and superpose a classical, continuous-wave local oscillator field a_{lo} with power P_{LO} , with a randomly fluctuating relative phase, θ_{LO} , and relative frequency, ω_{LO} :

$$a_{lo}(t) = \sqrt{P_{LO}} e^{-i(\omega_{LO}t + \theta_{LO})}. \quad (\text{A.34})$$

The field and power incident on the detector are then given by

$$\hat{a}_D(t) = \sqrt{P_{LO}} e^{-i(\omega_{LO}t + \theta_{LO})} + \hat{a}(t), \quad (\text{A.35})$$

$$P_D(t) = P_{LO} + P(t), \quad (\text{A.36})$$

In our experiment, we measure the normalized second-order correlation function of this heterodyne signal. We average over the relative phase between the local oscillator and the signal field, θ_{LO} , since the latter is not stabilized and drifts randomly on the time scale of the repetition period of our measurements. Due to these random drifts, there is no interference term in Eq. (A.36) since it averages to zero. Using the definitions in Eqs. (5.2), we first calculate the unnormalized second-order autocorrelation function of the heterodyne signal,

$$\begin{aligned} G_D^{(2)}(t, \tau) &= \langle \hat{a}_D^\dagger(t) \hat{a}_D^\dagger(t + \tau) \hat{a}_D(t + \tau) \hat{a}_D(t) \rangle \\ &= P_D(t) P_D(t + \tau) + 2P_{LO} \sqrt{P(t) P(t + \tau)} \text{Re} \left[e^{-i\omega_{LO}\tau} g^{(1)}(t, \tau) \right] \\ &\quad + P(t) P(t + \tau) \left[g^{(2)}(t, \tau) - 1 \right], \end{aligned} \quad (\text{A.37})$$

where we have averaged over the randomly fluctuating relative phase, θ_{LO} , such that terms of order $\mathcal{O}(P_{LO}^{1/2})$ and $\mathcal{O}(P_{LO}^{3/2})$ average to zero. We have also introduced the normalized correlation functions for the light exiting the nanofiber, $g^{(1)}(t, \tau)$ and $g^{(2)}(t, \tau)$. We can then normalize this result to obtain the normalized second-order autocorrelation function of the heterodyne signal,

$$\begin{aligned} g_D^{(2)}(t, \tau) &= 1 + \frac{2P_{LO} \sqrt{P(t) P(t + \tau)}}{P_D(t) P_D(t + \tau)} \left[\cos(\omega_{LO}\tau) \text{Re} \left(g^{(1)}(t, \tau) \right) + \sin(\omega_{LO}\tau) \text{Im} \left(g^{(1)}(t, \tau) \right) \right] \\ &\quad + \frac{P(t) P(t + \tau)}{P_D(t) P_D(t + \tau)} \left[g^{(2)}(t, \tau) - 1 \right]. \end{aligned} \quad (\text{A.38})$$

Note that since we drive the atomic ensemble on resonance, we assume that $g^{(1)}(t, \tau)$ is real, which is confirmed by the MCSA model. Since, for the experimental parameters in our experiment, $P_{LO} \gg \sqrt{P(t) P(t + \tau)}$, we neglect the last term that includes the

contribution of $g^{(2)}(t, \tau)$ such that we are left with

$$g_D^{(2)}(t, \tau) = 1 + V_{\max}(t, \tau) \cos(\omega_{\text{LO}}\tau)g^{(1)}(t, \tau). \quad (\text{A.39})$$

Here, we have introduced the maximum visibility of $V_{\max}(t, \tau)$.

$$V_{\max}(t, \tau) = \frac{2P_{\text{LO}}\sqrt{P(t)P(t+\tau)}}{P_D(t)P_D(t+\tau)}. \quad (\text{A.40})$$

The second-order correlation function of our heterodyne signal is thus given by the first-order correlation function of the signal field $\hat{a}(t)$, oscillating at ω_{LO} . We extract both $g_D^{(2)}(t, \tau)$ and $V_{\max}(t, \tau)$ from our measurements and infer the following quantity from our data:

$$\cos(\omega_{\text{LO}}\tau)g^{(1)}(t, \tau) = \frac{g_D^{(2)}(t, \tau) - 1}{V_{\max}(t, \tau)}, \quad (\text{A.41})$$

which we show in Fig. 5.7 of section 5.5.2.

To test our method of extracting the first-order correlation function as described above, we launch a time-modulated signal that is substantially weaker than the local oscillator field into the nanofiber-guided mode without trapping any atoms. The amplitude modulation is created using our pulse generation setup. This field stems from the same laser field as the local oscillator field and should be completely coherent on the time scale of tens of nanoseconds that we are interested in, such that we expect $g^{(1)}(t_1, \tau) = 1$. We use a polarizing beam splitter and waveplates to exactly match the polarization of the local oscillator field to the polarization of the signal field that exits the nanofiber-guided mode. The time trace of the power detected with the HPD is plotted in Fig. A.2(a). Next, we compute the normalized second-order correlation function, $g^{(2)}(t_1, \tau)$, which is shown for $t_1 = 5$ ns in Fig. A.2(b) in blue. Note that we subtract 1 from $g^{(2)}(t_1, \tau)$. At the same time, we measure the time traces using the SPCM, on which only the signal field is incident. This allows us to extract the maximal visibility, $V_{\max}(t_1, \tau)$, which we show in orange in panel (b). While the visibility of the oscillations of $g^{(2)}(t_1, \tau)$ decays with τ , this decay exactly matches the decay of V_{\max} . Indeed, when we normalize $g^{(2)}(t_1, \tau) - 1$ with $V_{\max}(t_1, \tau)$, the visibility stays constant, see panel (c). According to our analysis above, this is the first-order correlation function of the signal field, $g^{(1)}(t_1, \tau)$, oscillating at the local oscillator frequency, ω_{LO} . The visibility of the oscillations is thus given by $g^{(1)}(t_1, \tau)$. Fitting the amplitude of a cosine function to this data gives $g^{(1)}(t_1, \tau) = 1.04(1) \approx 1$, in accordance with our expectation. Note that the visibility can be further reduced if the polarization of the

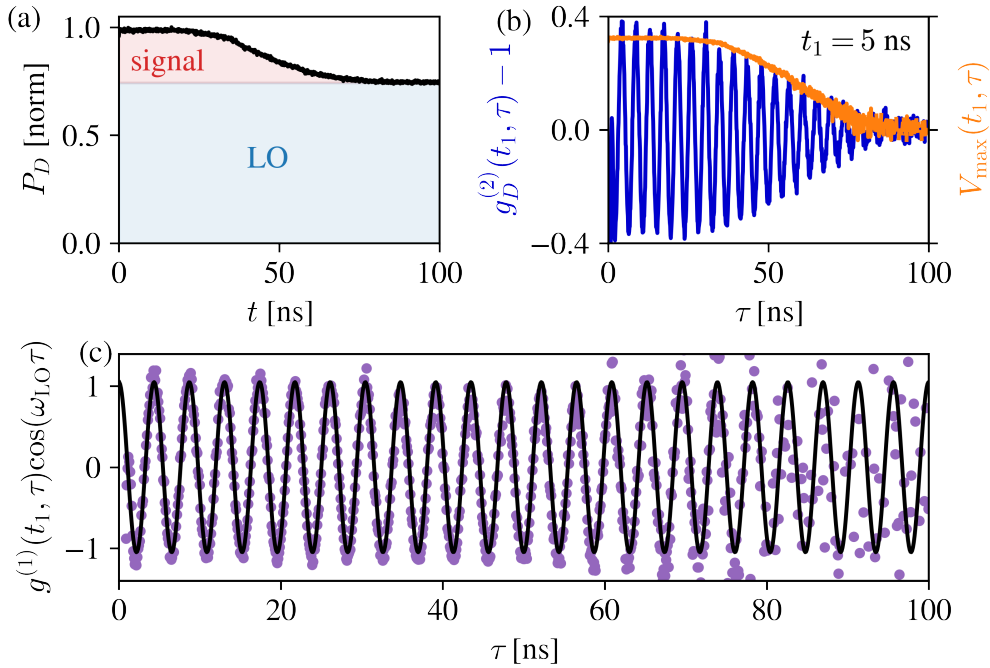


Figure A.2: Extracting the first-order coherence function of a coherent, nanofiber-guided signal from the second-order correlation function of a heterodyne signal. Here, no atoms are present. (a) Time trace of the detector signal. (b) Normalized second-order correlation of the heterodyne signal. The decay of the fringe visibility coincides with the decay of the maximal visibility, V_{\max} . (c) By normalizing the second-order correlation function by the maximal visibility, we obtain the first-order correlation function of the signal exiting the nanofiber-guided mode, oscillating at the local oscillator frequency, ω_{LO} .

field exiting the nanofiber-guided mode and the local oscillator field do not match. We checked that this effect is limiting the maximal visibility of our measurement in Fig. 5.7.

A.6 First-order correlation function of independent and inverted two-level atoms

Here, we analyze the first-order coherence function of an ensemble of independently emitting atoms that are initially excited and then decay due to spontaneous emission. We start with the first-order coherence function of a single atom, which is, e.g., derived in Ref [104]. For the initial conditions, $\langle \hat{\sigma}(t=0) \rangle = 0$, $\langle \hat{\sigma}^\dagger \hat{\sigma}(t=0) \rangle = 1$ (i.e. full inversion),

the solution of the Lindblad Master equation is

$$\langle \hat{\sigma}^\dagger \hat{\sigma}(t) \rangle = e^{-\Gamma t}, \quad (\text{A.42})$$

$$\langle \hat{\sigma}^\dagger(t) \rangle = \langle \hat{\sigma}(t) \rangle = 0. \quad (\text{A.43})$$

Using the quantum regression theorem, one can calculate the corresponding two-time correlation function,

$$\langle \hat{\sigma}^\dagger(t) \hat{\sigma}(t + \tau) \rangle = e^{-(\Gamma/2)\tau} e^{-\Gamma t}, \quad (\text{A.44})$$

where we have chosen a frame rotating at the atomic transition frequency. The field $\langle \hat{a} \rangle(t)$ emitted by the atom is proportional to $\langle \hat{\sigma} \rangle$, while the power is proportional to $\langle \hat{\sigma}^\dagger \hat{\sigma} \rangle$. Consequently, the two-time first-order coherence of the light emitted by the atom can be calculated as follows:

$$g^{(1)}(t, \tau) = \frac{\langle \hat{a}^\dagger(t) \hat{a}(t + \tau) \rangle}{\sqrt{\langle \hat{a}^\dagger \hat{a}(t) \rangle \langle \hat{a}^\dagger \hat{a}(t + \tau) \rangle}} = \frac{\langle \hat{\sigma}^\dagger(t) \hat{\sigma}(t + \tau) \rangle}{\sqrt{\langle \hat{\sigma}^\dagger \hat{\sigma}(t) \rangle \langle \hat{\sigma}^\dagger \hat{\sigma}(t + \tau) \rangle}}. \quad (\text{A.45})$$

Inserting the solutions given in Eq. (A.42) and (A.44), respectively, we get

$$g^{(1)}(t, \tau) = \frac{e^{-(\Gamma/2)\tau} e^{-\Gamma t}}{\sqrt{e^{-\Gamma t} \cdot e^{-\Gamma(t+\tau)}}} = \frac{e^{-(\Gamma/2)\tau} e^{-\Gamma t}}{e^{-(\Gamma/2)\tau} e^{-\Gamma t}} = 1, \quad (\text{A.46})$$

i.e., the two-time first-order coherence of the light spontaneously emitted by a single atom is time-independent.

Now we want to extend this result to two independently emitting atoms that are initially inverted. The field emitted by the atoms is proportional to $\langle \hat{\sigma}_1 \rangle + e^{i\phi} \langle \hat{\sigma}_2 \rangle$, where $e^{i\phi}$ is the relative propagation phase, and the index denotes the first and second atom, respectively. The total emitted power is given by $\langle \hat{\sigma}_1^\dagger \hat{\sigma}_1 \rangle + \langle \hat{\sigma}_2^\dagger \hat{\sigma}_2 \rangle$. The first-order coherence function of two independently emitting atoms is then proportional to

$$g^{(1)}(t, \tau) \sim \frac{\left\langle \left(\hat{\sigma}_1^\dagger(t) + e^{-i\phi} \hat{\sigma}_2^\dagger(t) \right) \left(\hat{\sigma}_1(t + \tau) + e^{i\phi} \hat{\sigma}_2(t + \tau) \right) \right\rangle}{\sqrt{(P_1(t) + P_2(t)) \cdot (P_1(t + \tau) + P_2(t + \tau))}}. \quad (\text{A.47})$$

Since we assume that the two atoms emit independently, all correlators involving both atoms vanish. We then get

$$g^{(1)}(t, t + \tau) \sim \frac{\langle \hat{\sigma}_1^\dagger(t) \hat{\sigma}_1(t + \tau) \rangle + \langle \hat{\sigma}_2^\dagger(t) \hat{\sigma}_2(t + \tau) \rangle}{2\sqrt{P(t)P(t + \tau)}}, \quad (\text{A.48})$$

where we have used that $P_1(t) = P_2(t) = P(t)$. This means that the two-time first-order correlation of the combined field is simply the mean of the two-time first-order correlations

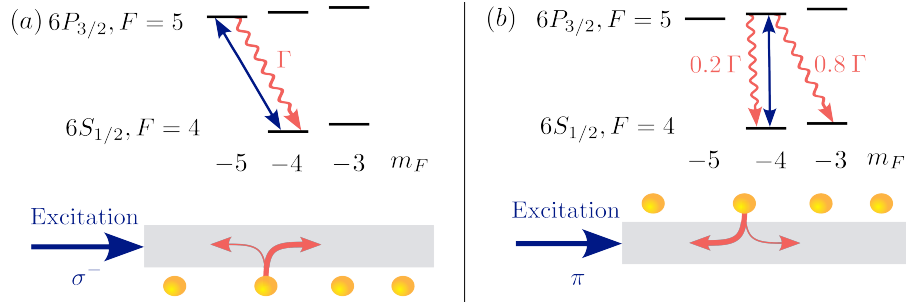


Figure A.3: (a) Excitation scheme as described in chapter 4. There, spontaneously emitted photons predominantly couple to the forward-propagating mode, i.e., the direction in which the excitation laser field propagates. (b) Alternative excitation scheme: Here, the atoms predominantly decay into the backward-propagating mode, i.e., opposite to the excitation laser field.

of the two individual atoms,

$$g^{(1)}(t, \tau) = \frac{1}{2} [g_1^{(1)}(t, \tau) + g_2^{(1)}(t, \tau)] = 1, \quad (\text{A.49})$$

i.e., also time-independent. This result can be generalized to the case of N independently emitting atoms that are inverted at time $t = 0$.

We can also calculate the time-averaged first-order correlation function for a single atom,

$$g^{(1)}(\tau) = \lim_{T \rightarrow \infty} \frac{1}{T} \int_0^T dt \frac{\langle \hat{\sigma}^\dagger(t) \hat{\sigma}(t + \tau) \rangle}{P(t)}. \quad (\text{A.50})$$

Using Eqs. (A.42) and (A.44), we get $g^{(1)}(\tau) = e^{-(\Gamma/2)\tau}$. As for the two-time first-order correlation function, we can generalize this result for N independently emitting atoms.

A.7 Alternative excitation scheme

In Fig. A.3(a), we show the optical excitation scheme used in chapter 4. We use a fiber-guided excitation laser field that is locally σ^- polarized to resonantly excite the atoms to the state $|e\rangle = |6P_{3/2}, F=5, m_F=-5\rangle$. Note that the quantization axis points out of the plane. The subsequent decay is σ^- -polarized, and the light predominantly couples to the forward-propagating mode, with a directionality of $D = 0.84$.

In panel (b), we show an alternative excitation scheme for which the ensemble predominantly decays into the opposite direction of the propagation direction of the excitation laser field. We trap atoms on the other side of the fiber in the same initial ground state as in (a), $|6S_{1/2}, F=4, m_F=-4\rangle$. This can be achieved by performing DRC using a

fiber-guided laser that propagates from right to left. Then, we excite the atoms using a fiber-guided laser field that is locally π -polarized, which excites the atoms to the state $|6P_{3/2}, F = 5, m_F = -4\rangle$. This state features a π - and a σ^- -polarized decay channel, with branching ratios of 0.2 and 0.8, respectively. The overall directionality of the emitted light is thus given by

$$D = 0.8D_{\sigma^-} + 0.2D_{\pi} = 0.68, \quad (\text{A.51})$$

where $D_{\pi} = 0$ and $D_{\sigma^-} = 0.84$, are the directionalities of the π - and σ^- -polarized decay channels, respectively.

A.8 Optical Bloch equations for a three-level atom

This section is based on the supplementary material of Ref. [138]:

C. Liedl, S. Pucher, P. Schneeweiss, L. P. Yatsenko, and A. Rauschenbeutel. [Observation of oscillatory Raman gain associated with two-photon Rabi oscillations of nanofiber-coupled atoms](#). *J. Phys. B: At. Mol. Opt. Phys.*, 55(23):234005, 2022.

Here, we describe the interaction between two classical laser fields with an atomic Λ -system, comprising two ground states, $|a\rangle = |6S_{1/2}, F = 4, m_F = -4\rangle$ and $|b\rangle = |6S_{1/2}, F = 3, m_F = -3\rangle$, as well as an excited state, $|e\rangle = |6P_{3/2}, F = 4, m_F = -4\rangle$, as depicted in Fig. 6.1. The Λ -system is driven by a probe laser field and a coupling laser field. The π -polarized coupling field with the Rabi frequency Ω_c is detuned by Δ_c from the $|a\rangle \rightarrow |e\rangle$ transition. The σ^- -polarized probe field with the Rabi frequency Ω_p is detuned by Δ_p from the $|b\rangle \rightarrow |e\rangle$ transition. In the rotating wave approximation, the Hamiltonian is given by [151]

$$\hat{\mathcal{H}} = -\hbar \frac{\Omega_p}{2} (\hat{\sigma}_{be} + \hat{\sigma}_{be}^\dagger) - \hbar \frac{\Omega_c}{2} (\hat{\sigma}_{ae} + \hat{\sigma}_{ae}^\dagger) - \hbar \Delta_p \hat{\sigma}_{ee}^\dagger \hat{\sigma}_{ee} - \hbar (\Delta_p - \Delta_c) \hat{\sigma}_{bb}^\dagger \hat{\sigma}_{bb}. \quad (\text{A.52})$$

where we have chosen the Rabi frequencies to be real. The operators $\sigma_{ij} = |i\rangle\langle j|$, where $i, j \in \{a, b, e\}$, describe the atomic annihilation and creation operators for the different transitions. As for a two-level atom, the dynamics of the density matrix $\hat{\rho}$ is then determined by the Lindblad master equation [103]

$$\frac{d\hat{\rho}}{dt} = -\frac{i}{\hbar} [\hat{\mathcal{H}}, \hat{\rho}] + \sum_{i \in \{a, b\}} \frac{1}{2} (2\hat{c}_n \hat{\rho} \hat{c}_n^\dagger - \hat{\rho} \hat{c}_n^\dagger \hat{c}_n - \hat{c}_n^\dagger \hat{c}_n \hat{\rho}). \quad (\text{A.53})$$

Here, \hat{c}_i are the collapse operators that describe spontaneous emission from the excited state, $|e\rangle$ to the two ground states,

$$\hat{c}_a = \sqrt{\Gamma_{ea}} \cdot \hat{\sigma}_{ae}, \quad (\text{A.54})$$

$$\hat{c}_b = \sqrt{\Gamma_{eb}} \cdot \hat{\sigma}_{be}, \quad (\text{A.55})$$

where $\Gamma_{ea} = (7/15)\Gamma$ and $\Gamma_{ba} = (5/12)\Gamma$ are the population decay rates from the excited state to $|a\rangle$ and $|b\rangle$, respectively, and $\Gamma = 2\pi \times 5.2$ MHz is the total decay rate. There are losses from the three-level system with the rate $\Gamma_{\text{loss}} = (7/60)\Gamma \approx 0.1\Gamma$, which we neglect in the following since they do not significantly alter the dynamics on the short timescale we are interested in. The differential equations for the density matrix elements read

$$\dot{\rho}_{aa} = -\frac{i}{2}\Omega_c(\rho_{ea} - \rho_{ae}) + \Gamma_{ea}\rho_{ee}, \quad (\text{A.56})$$

$$\dot{\rho}_{bb} = -\frac{i}{2}\Omega_p(\rho_{eb} - \rho_{be}) + \Gamma_{eb}\rho_{ee}, \quad (\text{A.57})$$

$$\dot{\rho}_{ab} = -\frac{i}{2}(\Omega_c\rho_{eb} - \Omega_p\rho_{ae}) - i(\Delta_c - \Delta_p)\rho_{ab}, \quad (\text{A.58})$$

$$\dot{\rho}_{ae} = -\frac{i}{2}\Omega_c(\rho_{ee} - \rho_{aa}) + \frac{i}{2}\rho_{ab}\Omega_p - \left(\frac{\Gamma}{2} + i\Delta_c\right)\rho_{ae}, \quad (\text{A.59})$$

$$\dot{\rho}_{be} = -\frac{i}{2}\Omega_p(\rho_{ee} - \rho_{bb}) + \frac{i}{2}\rho_{ba}\Omega_c - \left(\frac{\Gamma}{2} + i\Delta_p\right)\rho_{be}, \quad (\text{A.60})$$

$$\dot{\rho}_{ee} = \frac{i}{2}\Omega_c(\rho_{ea} - \rho_{ae}) + \frac{i}{2}\Omega_p(\rho_{eb} - \rho_{be}) - \Gamma\rho_{ee}. \quad (\text{A.61})$$

A.8.1 Adiabatic elimination

Adiabatic elimination of the excited state means that we can neglect the time derivative of the optical coherences and the population of the excited state, i.e. $\dot{\rho}_{ae} = \dot{\rho}_{be} = \dot{\rho}_{ee} = 0$. We can then express the matrix elements that involve the excited state in terms of the coherences and populations of the two ground states:

$$\rho_{ae} = \frac{-\frac{i}{2}\Omega_c(\rho_{ee} - \rho_{aa}) + \frac{i}{2}\rho_{ab}\Omega_p}{\frac{\Gamma}{2} + i\Delta_c}, \quad (\text{A.62})$$

$$\rho_{be} = \frac{-\frac{i}{2}\Omega_p(\rho_{ee} - \rho_{bb}) + \frac{i}{2}\rho_{ba}\Omega_c}{\frac{\Gamma}{2} + i\Delta_p}, \quad (\text{A.63})$$

$$\rho_{ee} = \frac{i}{2}\frac{\Omega_c}{\Gamma}(\rho_{ea} - \rho_{ae}) + \frac{i}{2}\frac{\Omega_p}{\Gamma}(\rho_{eb} - \rho_{be}). \quad (\text{A.64})$$

Since we are interested in the dynamics for large detuning and on two-photon resonance, we assume $\Delta_c = \Delta_p = \Delta$. The condition for the validity of adiabatic elimination is that

the excited state population ρ_{ee} is very small, i.e., that

$$\Omega_p^2, \Omega_c^2 \ll 4\Delta^2 + \Gamma^2. \quad (\text{A.65})$$

If this condition is met, we can eliminate ρ_{ee} in Eqs. (A.62)–(A.64) and insert the resulting expressions into the differential equations for the ground-state density matrix elements, Eqs. (A.56)–(A.58), which then read

$$\dot{\rho}_{aa} = -\Gamma_a \rho_{aa} + \Gamma_{ba} \rho_{bb} - \frac{i}{2} \tilde{\Omega} (\rho_{ba} - \rho_{ab}), \quad (\text{A.66})$$

$$\dot{\rho}_{bb} = -\Gamma_b \rho_{bb} + \Gamma_{ab} \rho_{aa} + \frac{i}{2} \tilde{\Omega} (\rho_{ba} - \rho_{ab}), \quad (\text{A.67})$$

$$\dot{\rho}_{ab} = -\frac{i}{2} \tilde{\Omega} (\rho_{bb} - \rho_{aa}) + i \tilde{\Delta} \rho_{ab} - \left(\frac{\Gamma_c}{2} + \frac{\Gamma_p}{2} \right) \rho_{ab}. \quad (\text{A.68})$$

Here, we have introduced the two-photon Rabi frequency

$$\tilde{\Omega} = \frac{\Omega_c \Omega_p}{2\Delta}. \quad (\text{A.69})$$

The transition rates to the excited state from state $|a\rangle$ and $|b\rangle$ due to excitation by the coupling and probe fields are given by

$$\Gamma_{c,p} = \Gamma \frac{\Omega_{c,p}^2}{4\Delta^2}, \quad (\text{A.70})$$

respectively. These rates also lead to a relaxation of the coherence ρ_{ab} with rate $\Gamma_c/2 + \Gamma_p/2$. The rates $\Gamma_a, \Gamma_b, \Gamma_{ab}$, and Γ_{ba} describe the redistribution of population between the two ground states due to spontaneous emission. They are given by the following expressions:

$$\Gamma_a = \frac{1}{4} \frac{\Omega_c^2}{\Delta^2} (\Gamma - \Gamma_{ea}) = \Gamma_c \left(1 - \frac{\Gamma_{ea}}{\Gamma} \right) = \frac{8}{15} \Gamma_c, \quad (\text{A.71})$$

$$\Gamma_{ba} = \frac{1}{4} \frac{\Omega_p^2}{\Delta^2} \Gamma_{ea} = \Gamma_p \frac{\Gamma_{ea}}{\Gamma} = \frac{7}{15} \Gamma_p, \quad (\text{A.72})$$

$$\Gamma_b = \frac{1}{4} \frac{\Omega_p^2}{\Delta^2} (\Gamma - \Gamma_{eb}) = \Gamma_p \left(1 - \frac{\Gamma_{eb}}{\Gamma} \right) = \frac{7}{12} \Gamma_p, \quad (\text{A.73})$$

$$\Gamma_{ab} = \frac{1}{4} \frac{\Omega_c^2}{\Delta^2} \Gamma_{eb} = \Gamma_c \frac{\Gamma_{eb}}{\Gamma} = \frac{5}{12} \Gamma_c. \quad (\text{A.74})$$

Finally, $\tilde{\Delta}$ denotes the detuning from the light-shifted two-photon resonance,

$$\tilde{\Delta} = \Delta_p - \Delta_c + \frac{\Omega_c^2}{2\Delta_c}. \quad (\text{A.75})$$

A.8.2 Simplified effective two-level system

To describe the experimental data in the main manuscript, we make the following approximations:

1. We assume that the system is closed, such that $\Gamma_{ea} + \Gamma_{eb} = \Gamma$.
2. For simplicity, we assume that the approximate equality $\Gamma_{ea} \approx \Gamma_{eb}$ is exact: $\Gamma_{ea} = \Gamma_{eb} = \Gamma/2$.
3. Since the probe field is much weaker than the control field, we assume that $\Gamma_p = 0$.
4. We assume that we have tuned the laser frequency to the light-shifted two-photon resonance: $\tilde{\Delta} = 0$.

Under these assumptions, the different rates simplify such that $\Gamma_a = \Gamma_{ab} = \Gamma_c/2$ and $\Gamma_b = \Gamma_{ba} = 0$. The dynamics of the ground-state populations and coherences is then governed by the following set of equations.

$$\dot{\rho}_{aa} = -\tilde{\Gamma}\rho_{aa} - \frac{i}{2}\tilde{\Omega}(\rho_{ba} - \rho_{ab}), \quad (\text{A.76})$$

$$\dot{\rho}_{bb} = +\tilde{\Gamma}\rho_{aa} + \frac{i}{2}\tilde{\Omega}(\rho_{ba} - \rho_{ab}), \quad (\text{A.77})$$

$$\dot{\rho}_{ab} = -\frac{i}{2}\tilde{\Omega}(\rho_{bb} - \rho_{aa}) - \tilde{\Gamma}\rho_{ab}. \quad (\text{A.78})$$

These equations describe a resonantly driven two-level system with ground state $|b\rangle$ and excited state $|a\rangle$, with an effective decay rate from $|a\rangle \rightarrow |b\rangle$, $\tilde{\Gamma}$:

$$\tilde{\Gamma} = \frac{\Gamma_c}{2} = \frac{\Omega_c^2}{8\Delta^2}\Gamma. \quad (\text{A.79})$$

Here, the coherence ρ_{ab} decays at the same rate as the population, $\tilde{\Gamma}$. This marks an important difference compared to the usual two-level closed system, in which the coherence would decay with a rate of $\tilde{\Gamma}/2$. This additional decoherence channel is associated with a transition to the excited state $|e\rangle$ and a subsequent decay to the initial state. This process does not affect the ground-state populations but leads to additional decoherence. The solution of these equations is analogous to the solution we gave in section A.3.2. However, here we are interested in the initial conditions $\rho_{aa}(0) = 1, \rho_{ab}(0) = 0$.

Selbstständigkeitserklärung

Ich erkläre, dass ich die Dissertation selbständig und nur unter Verwendung der von mir gemäß § 7 Abs. 3 der Promotionsordnung der Mathematisch-Naturwissenschaftlichen Fakultät, veröffentlicht im Amtlichen Mitteilungsblatt der Humboldt-Universität zu Berlin Nr. 42/2018 am 11.07.2018 angegebenen Hilfsmittel angefertigt habe.

Berlin, 27.01.2023

Christian Liedl